APPLICATIONS OF PLASMON ENHANCED EMISSION AND ABSORPTION

A THESIS

SUBMITTED TO THE GRADUATE PROGRAM OF MATERIALS SCIENCE AND NANOTECHNOLOGY

AND THE INSTITUTE OF ENGINEERING AND SCIENCES

OF BILKENT UNIVERSITY

IN PARTIAL FULLFILMENT OF THE REQUIREMENTS

FOR THE DEGREE OF

MASTER OF SCIENCE

By

Sencer Ayas

December, 2009

I certify that I have read this thesis and that in my opinion it is fully adequate, in scope and in quality, as a thesis for the degree of Master of Science.

_____

Prof. Dr. Salim Çıracı (Supervisor)

I certify that I have read this thesis and that in my opinion it is fully adequate, in scope and in quality, as a thesis for the degree of Master of Science.

_____

Assist. Prof. Dr. Aykutlu Dâna (Co-supervisor)

I certify that I have read this thesis and that in my opinion it is fully adequate, in scope and in quality, as a thesis for the degree of Master of Science.

_____

Assist. Prof. Dr. Ceyhun Bulutay

I certify that I have read this thesis and that in my opinion it is fully adequate, in scope and in quality, as a thesis for the degree of Master of Science.

_____

Assist. Prof. Dr. Ali Kemal Okyay

Approved for the Institute of Engineering and Sciences:

_____

Prof. Dr. Mehmet B. Baray

Director of Institute of Engineering and Sciences

ABSTRACT

APPLICATION OF PLASMON ENHANCED EMISSION AND ABSORPTION

Sencer Ayas

M. Sc., Department of Materials Science and Nanotechnology

Supervisor: Prof. Dr. Salim Çıracı

December, 2009

The term plasmon-polariton is used to describe coupled modes of electromagnetic waves with electronic plasma oscillations in conductors. Surface plasmon resonances have found profound interest over the last few decades in multiple fields ranging from nanophotonics to biological sensing. In this thesis, we study enhancement of absorption and emission of radiation due to the presence of a modified local electromagnetic mode density within the vicinity of metallic surfaces supporting plasmon modes. Various coupling schemes of free-space electromagnetic modes to plasmon modes are investigated theoretically and experimentally. Local mode densities and field enhancements due to plasmon modes in planar structures, gratings and optical antennas have been studied in their relation to the absorption and emission enhancement of dipoles positioned in various orientations and locations with respect to structures displaying plasmonic effects. Particularly, grating coupled plasmon resonances were analysed using Rigorously Coupled Wave Analysis and Finite Difference Time domain methods. Experimental demonstrations of absorption and emission enhancement of dielectric layers containing Rhodamine 6G on various plasmonic structures are given. Confocal Raman microscopy was used in characterization of fabricated structures. It is seen that the experimental measurements are in good agreement with theoretical predictions. Direction dependent luminescence enhancement is observed with dye molecules on grating structures. Potential applications of plasmon enhanced absorption and emission include high sensitivity absorption spectroscopy, performance enhancement in thin film solar cells and luminescent concentrators.

Keywords: Plasmonics, Emission, Absorption,Grating Coupled Surface Plasmon Resonance, Local mode density

ÖZET

PLASMON ARTTIRIMLI IŞINIM VE EMİLİM UYGULAMALARI

Sencer Ayas

Tez Yöneticisi: Prof. Dr. Salim Çıracı

Yüksek Lisans, Malzeme Bilimi ve Nanoteknoloji Bölümü

Aralık, 2009

Plazmon polariton terimi iletkenlerdeki plazma elektronik salınımlarıyla çiftlenmiş elektromanyetik dalga modlarını tanımlamak için kullanılmaktadır. Yüzey plazmon rezonansları son yirmi 30 yilda nanofotonikten ve biyolojik algılamaya kadar birçok alanda geniş merak uyandırmıstır. Bu tezde, plazmon modlarını destekleyen metal yüzeylerin sebep oldugu ışınım ve emilim arttıtrımı lokal elektromanyetik mod yoğunluğuna göre incleledik. Serbest uzay elektromanyetik modlarını, plazmon modlarına çiftleyen değişik uyarılma mekanizmalarını teorik ve deneysel olarak inceledik. Dipollerdeki ışınım ve emilim plazmonik yapıların lokal mod yoğunluğu ve alan arttrımına bağlı olarak çeşitli oryantasyondaki ve plazmonik yapıların değişik yerlerindeki dipollerle inceledik. Kırınım ağına çiftlenmiş plazmon rezonansları RCWA ve FDTD metodlarıyla incelenmiştir. Rhodamine 6G boyasının emilim ve ışınım arttırımı plazmonik yapılarda deneysel olarak gösterilmiştir.Ayrıca konfokal raman mikroskobu florasans karakterizasyounda kullanılmıştır. Teorik sonuçşar ve deneysel sonuçlar birbirini destekler niteliktedir. Ayrıca boya moleküllerinin ışınımının plazmonik kırınım ağı yapılarında yöne bağımlılığı gösterilmiştir. Plazmon arttırımlı ışınım ve emilim uygulama alanları olaraksa, çok hassas emilim spektroskopisi, ince film güneş pillerinde performans arttırımı ve ışıyan yoğunlaştırıcılar olarak gösterilebilir.

Anahtar kelimeler: Plazmonik, Işınım, Emilim, Kırınım ağına çiftlenmiş Plazmon rezonansı, lokal mod yoğunluğu

Acknowledgement

First of all, I would like to express my gratitude to my advisors Prof. Salim Çıracı and Prof. Aykutlu Dana for their support in every aspect of this thesis.

I would like to thank to my thesis committee, Prof. Ceyhun Bulutay and Prof. Ali Kemal Okyay. I would also like to thank to Prof. Mehmet Bayındır for his instrumental support.

I thank to my groupmates: Hasan Güner, Kurtuluş Abak, Mustafa Ürel, Okan Öner Ekiz.

I would also thank to Koray Mızrak for his support on FIB and E-Beam processes.

I thank to my office mates, Kurtuluş Abak, Mustafa Ürel, Ali Güneş Kaya, Seydi Yavaş and Mutlu Erdoğan. I would also thank to my precious friends Yavuz Nuri Ertaş.

I gratefully aknowledged TUBITAK for the financial support.

Table of Contents

Chapter 1

Introduction and Motivation

Surface plasmons are charge density oscillations propagating along the metal dielectric interfaces. They are tightly confined to interface and induce an evanescent wave perpendicular to the interface. Due to confinement of plasmonic modes, field intensity enhances enormously at the interface. This unique property of surface plasmons promise several applications in the area of photonics. Metallic surfaces are tailored for exploiting the properties of surface plasmons. Extra Ordinary Transmission (EOT), sub wavelength confinement, low threshold lasers, surface plasmon resonance (SPR) sensors, plasmon enhanced solar cells and plasmon enhanced light emitting devices are realized based on the principles of surface plasmons [1-9].

Fluorescence techniques are widely studied due to their usage in biological imaging, fluorescence sensors and optical microscopy. Pushing the sensitivity up to single photon detection of these devices is now one of the hot topics for scientist and researchers. The absorption and emission properties of emitters strongly depend on not only to the quantum mechanical dynamics, but also the surrounding environment. Modifying the absorption and emission medium changes the fluorescence dynamics. Plasmonic structures are suitable for this aim. In recent studies, fluorescence of molecules are studied on or near plasmonic resonators and antennas both theoretically and experimentally [9-13]. Interaction of optical emitters with surface plasmons in a semiconductor heterostructures and organic polymers are studied with various aspects [14-16].

The motivation behind this thesis was to understand the dynamics of absorption and the emission processes, then integrate this problem with plasmonics. Therefore, in this study, we numerically and experimentally studied both absorption and emission enhancement of fluorophores on or near plasmonic structures. Using the theoretical

background, radiative rate enhancement, quantum yield and field distribution calculations were done numerically. Sinusoidal and biharmonic grating structures are fabricated using soft lithography and focused ion beam(FIB) techniques. Nanoantenna strip are fabricated using E-beam lithography technique. We spin coated the fabricated plasmonic structures with Rhodamine 6G doped dye layers and measured the fluorescence signals under different excitation conditions to demonstrate emission and absorption enhancements.

Our contributions can be summarized as follows

1. Simulation of emission properties of optical emitters on different plasmonic structures. Position and polarization dependent emission enhancement of classical dipoles is studied on biharmonic gratings.
2. Process development for the fabrication of sinusoidal gratings using nanoimprint lithography, PDMS moulding, dry etching. Absorption enhancement of Rhodamine 6G is demonstrated due to excitation of surface plasmons.
3. Fabrication of biharmonic gratings using focused ion beam(FIB) techniques and measurement of emission enhancement due to enhancement of plasmonic mode density at the band edges of plasmonic dispersion curves.

The outline of this thesis as follows. In the second chapter, theoretical background of fluorescence, absorption and emission processes is provided by deriving Fermi's Golden Rule and classical dipole emission. In the third chapter, fundamental properties of surface plasmons and coupling schemes are explained. Transfer matrix method(TMM) and rigorous coupled wave analysis (RCWA) methods are derived. Field distributions, dispersion curves are studied numerically to verify theoretical background. In the fourth chapter, emission and absorption enhancement is simulated for different plasmonic structures. Emission enhancement and quantum yield of emitters are calculated on plasmonic structures. In the fifth chapter, optimization and fabrication of lamellar and sinusoidal gratings are presented. Fluorescence measurements on grating and nanoantenna strips are also provided. In the sixth chapter, we summarize what we have done so far on this subject.

Chapter 2

THEORETICAL BACKGROUND

In this chapter, theoretical background information about fluorescence and photoluminescence is discussed by introducing radiative and non-radiative lifetimes. Absorption enhancement is explained using Fermi's Golden Rule, which is derived from time-dependent perturbation theory. Then emission of a dipole is described in free space and in the presence of inhomogeneous environment.

2.1 Fluorescence

Fluorophores, molecules and quantum-dot nanoparticles interact with incident photon and absorb it, then re-emit it at a longer wavelength. This process is called fluoroscence. Fluorescence occurs in a certain time period called decay time. Radiative and non-radiative decay are two types of relaxation mechanism in emission process. Non-radiative decay is an internal mechanism of emitter due to the quantum interaction of wave functions of exited states. This mechanism is the lossy mechanism and is the reason for red shift in the emission wavelength and independent of the environment that the emitter is situated. Radiative decay mechanism is directly related to the local electromagnetic density of states. In vacuum, this relaxation process is called spontaneous emission. Due to the dependence on local electromagnetic field of the environment, it can be altered or quenched by changing the photonic mode density of the system. In the emission process, the photonic mode density cannot be changed externally by an excitation mechanism, since once the emitter is excited, decay mechanisms are driven by internally for non-radiative and by its own emission mode density for its radiative decay processes. Therefore, radiative decay rates can only be changed by modifying the mode density at the emission wavelength. Lasers are such devices, working principle based on controlling decay rates and spontaneous emission.

In lasers, there occurs coherent population of emitted photon. This process is called stimulated emission.

There are two types of fluorescence processes, Phosphorescence and Photoluminescence. In Phosphorescence, absorbed photons are emitted in much longer time with respect to photoluminescence. The photoluminescence process can be understood from Jablonski diagram [Fig 2.1]. Incident photons excites the molecule to an upper energy level. By internal mechanisms it decays to a lower energy level. Then, the molecule relaxes to its ground state by emitting a photon.

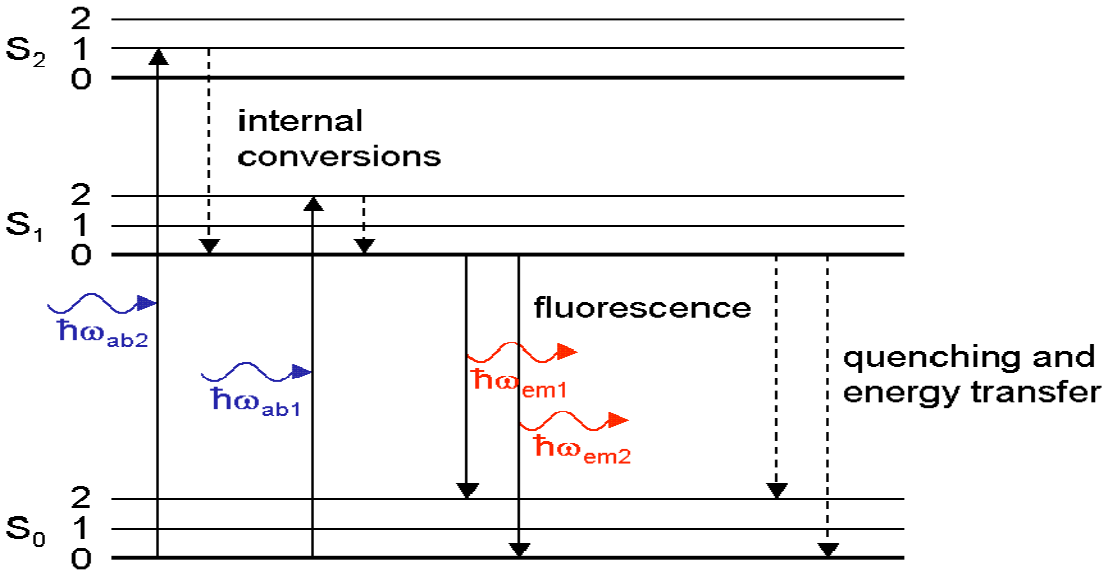

Figure 2.1 *Jablonski diagram for photoluminescence. Incident photon excites the molecule to an upper energy level. By internal mechanisms it decays to low energy level. Then the emitter relaxes to its ground state by emitting a photon*

In the emission process, quantum yield or efficiency of an emitter described the ratio of the emitted photons to absorbed photons and given by,

$$n_o = \frac{\gamma_{ro}}{\gamma_o} \tag{2.1}$$

where $\gamma_o = \gamma_{ro} + \gamma_{nro}$. γ_o is the total decay rate from an excited state to ground state. γ_{ro} and γ_{nro} are radiative and nonradiative decay rates. Quantum yield is a measure of the spontaneous emission rate. γ_o and γ_r can be changed by modifying the local photonic mode density. Moreover, Eq.2.1 is defined for vacuum environment and n_o is

called intrinsic quantum yield. If the emitter is near a particle, surface or inside a cavity, local photonic mode density changes so that decay rates and quantum yield of the emitter changes. The modified quantum yield is given by,

$$n = \frac{\gamma_r}{\gamma} \tag{2.2}$$

where $\gamma = \gamma_r + \gamma_{nr} + \gamma_{nro}$. In Eq. 2.2, quantum yield changes due to the change of radiative and total decay rates. The term γ_{nr} is inserted due to the external losses caused by new environment.

2.2 Absorption Enhancement

Absorption of a photon by a molecule can be understood by means of Time-Dependent Perturbation Theory. It is a well known theory, that explains how the quantum mechanical systems reply to the changes in their environment. One of the main results of Time-Dependent Perturbation Theory is the understanding of light-matter interaction.

To understand the interaction of excitation field with a quantum mechanical system, such as fluorophores, one has to solve Time Dependent Schrodinger's equation. For the sake of simplicity consider a two level quantum mechanical system with an initial and final states $|\psi_i\rangle$, $|\psi_f\rangle$. The wave function of system can be written as,

$$|\Psi\rangle = a_i(t)|\psi_i\rangle e^{\frac{-iE_i t}{\hbar}} + a_f(t)|\psi_f\rangle e^{\frac{-iE_f t}{\hbar}} \tag{2.3}$$

Using Eq.2.3 in Schrodinger's equation we get the coupled equation between a_i, a_f given by [18],

$$\frac{da_f}{dt} = \frac{1}{i\hbar} a_i e^{iw_{if}t} \langle \psi_f | H_p(t) | \psi_i \rangle \tag{2.4}$$

$$\frac{da_i}{dt} = \frac{1}{i\hbar} a_i e^{iw_{if}t} \langle \psi_i | H_p(t) | \psi_f \rangle \tag{2.5}$$

with $w_{if} = \frac{(E_f - E_i)}{\hbar}$

For starters, to elucidate the interaction of light with an emitter, oscillatory electromagnetic wave nature of light is used. Consider a monochromatic electromagnetic wave that is polarized in the z direction,

$$E = \hat{z}\, E_o (e^{iwt} + e^{-iwt}) = \hat{z}\, 2E_o \cos(wt) \tag{2.6}$$

This would lead to perturbing Hamiltonian given by,

$$\begin{aligned} H_p(t) &= eE_o (e^{iwt} + e^{-iwt})\, \hat{z} \\ H_{po} &= eE_o\, \hat{z} \end{aligned} \tag{2.7}$$

We assumed this perturbation is on for a certain time interval than it turns off as,

$$\begin{aligned} &H_{po}(t) = 0 \quad ,\text{t<0} \\ &H_p(t) = H_{po}(e^{iwt} + e^{-iwt})\, \hat{z} \;,\text{0<t<to} \\ &H_{po}(t) = 0 \;\; ,\text{t>to} \end{aligned} \tag{2.8}$$

If the system is in the lower energy state $|\psi_i\rangle$ initially, then the probability P of finding system in the final state $|\psi_f\rangle$ is $P = |a_f|^2$.

To calculate the probability P, the value of a_f has to be evaluated after time period t_o. After some mathematical manipulations, the probability of the system to be found in the final state then becomes [18],

$$\begin{aligned} P = |a_f|^2 = \frac{t_o^2}{\hbar^2} \left| \langle \psi_i | H_{po} | \psi_f \rangle^2 \right| \Bigg\{ &\left| \frac{\sin((w_{if} + w)t_o/2)}{(w_{if} + w)t_o/2} \right|^2 + \left| \frac{\sin((w_{if} - w)t_o/2)}{(w_{if} - w)t_o/2} \right|^2 \\ &+ 2\cos(wt_{to}) \frac{\sin((w_{if} - w)t_o/2)}{(w_{if} - w)t_o/2} \frac{\sin((w_{if} + w)t_o/2)}{(w_{if} + w)t_o/2} \Bigg\} \end{aligned} \tag{2.9}$$

The term with a cosine product in Eq.2.9 is zero. Since, sinc functions decay rapidly after $w = \pm w_{if}$

$$\frac{\sin((w_{if} - w)t_o/2)}{(w_{if} - w)t_o/2} \frac{\sin((w_{if} + w)t_o/2)}{(w_{if} + w)t_o/2} = 0 \tag{2.10}$$

We have the transition probability for a two level system, which is initially in the $|\psi_i\rangle$ state as,

$$P = |a_f|^2 = \frac{t_o^2}{\hbar^2}\left|\langle\psi_i|H_{po}|\psi_f\rangle^2\right|\left\{\left|\frac{\sin((w_{if}+w)t_o/2)}{(w_{if}+w)t_o/2}\right|^2 + \left|\frac{\sin((w_{if}-w)t_o/2)}{(w_{if}-w)t_o/2}\right|^2\right\} \quad (2.11)$$

There are two terms in Eq.2.11. To interpret this formula to the absorption probability, the system has to be in the lower energy state. Then, the first term of Eq.2.11 is zero.

Finally, we have the absorption probability for a two level quantum mechanical system as,

$$P = |a_f|^2 = \frac{t_o^2}{\hbar^2}\left|\langle\psi_i|H_{po}|\psi_f\rangle^2\right|\left|\frac{\sin((w_{if}-w)t_o/2)}{(w_{if}-w)t_o/2}\right|^2 \quad (2.12)$$

If the electromagnetic wave is resonant with this system, absorption process occurs where $w = w_{if}$ and we get,

$$P = |a_f|^2 = \frac{t_o}{\hbar^2}\left|\langle\psi_i|H_{po}|\psi_f\rangle^2\right| \quad (2.13)$$

More general form of Eq.2.13 is obtained by inserting the mode density into Eq. 2.12,

$$\begin{aligned} P = |a_f|^2 &= \frac{t_o^2}{\hbar^2}\left|\langle\psi_i|H_{po}|\psi_f\rangle^2\right|\int\left|\frac{\sin((w_{if}-w)t_o/2)}{(w_{if}-w)t_o/2}\right|^2 g(\hbar w_{if})d\hbar w_{if} \\ P = |a_f|^2 &= \frac{2t_o\pi}{\hbar}\left|\langle\psi_i|H_{po}|\psi_f\rangle^2\right| g(\hbar w_{if}) \end{aligned} \quad (2.14)$$

Using Eq. 2.7 in Eq.2.14, we obtain the famous *Fermi's Golden Rule,*

$$W = \frac{2\pi}{\hbar}\left|\langle\psi_i|ez|\psi_f\rangle^2\right| g(\hbar w_{if})|E_o|^2 \quad (2.15)$$

The main result of this equation turns out that, the absorption rate is directly related the photonic mode density or $|E_0|^2$, the intensity of incident electric field.

Finally, the emission enhancement of a emitter due to the intensity enhancement of incident light can be calculated using the formula,

$$\frac{I}{I_o} = \left| \frac{p.E(\omega_{exc})}{p.E_o(\omega_{exc})} \right|^2$$

(2.16)

where $|E_0|^2$ is the field intensity in free space, $|E|^2$ is the modified field intensity at the emitter position, ω_{exc} is the excitation frequency and p is the polarization of the emitter.

2.3 Emission Enhancement

In the previous chapter, fluorescence enhancement due to the absorption enhancement is derived using time dependent perturbation theory. In this chapter the emission enhancement is going to be explained due to the change in the photonic mode density during the emission process. Rigorous classical oscillator model is used for the derivation of emission. Although classical oscillator model for emission is a quite simple model, it is in good agreement with experimental results. This model gives us two main intuition: Decay rates and frequency shifts. Decay rates are well explained with this model, but in order to calculate frequency shifts due to the changes of mode density, a quantum mechanical approach has to be introduced.

An emitting source can be assumed as a dipole. The emission property of dipoles can be modeled as classical equation of motion which has a dipole moment p, as given below[19,20],

$$\frac{d^2p}{dt^2} + \gamma_o \frac{dp}{dt} + w_o^2 p = \frac{e^2}{m}(p_o^* E_{loc}(r_o)) \qquad (2.17)$$

γ_o is the free space decay rate , w_o is the oscillation frequency in the absence of damping , m is the effective mass of the dipole and $E_{loc}(r_o)$ is the electric field induced by dipole at its location.

In free space, right hand side of Eq. 2.17 is zero and written in the form :

$$\frac{d^2p}{dt^2}+\gamma_o\frac{dp}{dt}+w_o^2p=0 \tag{2.18}$$

while the solution of Eq. 2.18 is $p=p_oe^{-iw_ot}e^{\frac{\gamma_o t}{2}}$

If the emitter is in inhomogeneous environment, the solution to Eq. 2.18 is $p=p_oe^{-iwt}$, where w is given by [21],

$$w=-i\frac{\gamma_o}{2}+w_o\sqrt{1-\frac{\gamma_o^2}{4w_o^2}-\frac{e^2}{mw_o^2p_o^2}p_o^*E_{loc}(r_o)} \tag{2.19}$$

Local electric field is in the same frequency with the oscillatory dipole moment $E_{loc}(r_o)=E_{loc}(r_o)e^{-iwt}$. Assuming that $\frac{\gamma_o^2}{4}+\frac{e^2}{mp_o^2}p_o^*E_{loc}(r_o)$ term is very small compared to w_o^2 and using the expansion $\sqrt{1-x}\cong 1-\frac{x}{2}$, we get

$$w=-i\frac{\gamma_o}{2}+w_o(1-\frac{\gamma_o^2}{8w_o^2}-\frac{e^2}{2mw_o^2p_o^2}p_o^*E_{loc}(r_o)) \tag{2.20}$$

Eq. 2.20 involves two terms, both decay rate and new oscillation frequency of the dipole. The real part and imaginary part correspond to new oscillation frequency and the new decay rate.

$$\begin{aligned} w_{new}&=w_o-\frac{\gamma_o^2}{8w}-\frac{e^2}{2mw_op_o^2}\mathrm{Re}(p_o^*E_{loc}(r_o)) \\ \gamma&=\gamma_o+\frac{e^2}{mw_op_o^2}\mathrm{Im}(p_o^*E_{loc}(r_o)) \end{aligned} \tag{2.21}$$

Eq.2.21 describes the classical decay rate and oscillation frequency of an classical emitter in inhomogeneous environment. The oscillation frequency of the dipole is red shifted [Eq.2.20]. This result may be misleading but it gives an intuition about shift of emission wavelength of the dipole. On the other hand decay rates go well together

with experimental results, full quantum mechanical and semi-classical approaches[13]. If the local electric field is zero in Eq. 2.21, we get free space parameters.

In free space, the radiative decay rate of an optical emitter is given by[22]

$$\gamma_{ro} = \frac{2Ne^2 w_0^{\,2}}{3mc^3} \tag{2.22}$$

If we combine Eqs. 2.1-21-22, we get normalized decay rate as follows

$$\frac{\gamma}{\gamma_o} = 1 + \frac{3n_o c^3}{2w_o^3 N p_o^2} \mathrm{Im}(p_o^* E_{loc}(r_o)) \tag{2.23}$$

where N is the refractive index. By calculating the induced electric field at the dipole position we can calculate normalized decay rate of any system. However, analytically for most of the systems, it is hard to calculate the electric field distribution. Different solving techniques have been introduced to for mathematically complex system. For instance, dipoles near spherically symmetric particles are solved by using Mie's Theory[9]. Green Function formalism is used for cylindrically symmetric systems and stratified media[21,23]. Transmittance matrix and plane wave expansion methods are used together to analyze emission on stratified medium[24].

Solving Maxwell's equations numerically is one of most used techniques for analytically complex systems. Finite Element Method(FEM), Finite Integration Techniques(FIT), Finite Difference Frequency Domain(FDFD) and Finite Different Time Domain Methods are widely used numerical methods[25-28].

Quantum mechanical approach for normalized decay rates is more complex rather than the classical one and is given by [19]

$$\frac{\gamma}{\gamma_o} = \frac{n_p \cdot \mathrm{Im}\{G(r_o, r_o, w_o)\} \cdot n_p}{n_p \cdot \mathrm{Im}\{G_o(r_o, r_o, w_o)\} \cdot n_p} \tag{2.24}$$

where $G(r_o, r_o, w_o)$ and $G_o(r_o, r_o, w_o)$ are the Green's Dyadic Functions in inhomogeneous and free space at r_o due to emitter positioned r_o. n_p is the unit vector in the direction of emitter. Green functions in Eq.2.24 are 3 by 3 tensor given by ,

$$G = \begin{bmatrix} G_{xx} & G_{xy} & G_{xz} \\ G_{yx} & G_{yy} & G_{yz} \\ G_{zx} & G_{zy} & G_{zz} \end{bmatrix} \tag{2.25}$$

One has to calculate $G(r_o, r_o, w_o)$ in inhomogeneous environment to calculate normalized decay rate, which is impossible for most of the system. On the other hand field distributions are given by using Green's Integral equations taken from Ref. [19],

$$\begin{aligned} E(r) &= E_o + iw\mu_o\mu\int_V G(r,r')\,j(r') \\ H(r) &= H_o + iw\mu_o\mu\int_V G(r,r')\,j(r') \end{aligned} \tag{2.26}$$

where E_o and H_o are the fields in the absence of source. For a point source or dipole Eq. 2.26 reduced to by using the relation between current source and dipole moment $j(r) = -iwp_o\delta[r - r_o]$

$$\begin{aligned} E(r) &= w^2\mu_o\mu G(r,r_o)\,p_o \\ H(r) &= -iw\mu_o\mu[\nabla \times G(r,r_o)]p_o \end{aligned} \tag{2.27}$$

Using full quantum mechanical approach derived using Dyadic Green Functions along with numerically solving the local electric field distribution, it is possible to obtain normalized decay rates for an emitter. Still we have no information about the radiative and non-radiative decay rates. Radiative decay rate is related to the power radiated to the far field. Dyadic Green Function can be partitioned to near field, intermediate field and far-field terms. Moreover, the relation between the radiative and total decay rates can be written in the form [1,29],

$$\frac{P_{rad}}{P_{tot}} = \frac{\gamma_r}{\gamma} \tag{2.28}$$

Where, P_{rad} is the radiated power to far field and P_{tot} is the total radiated power by the dipole. P_{rad} and P_{tot} can be evaluated by integrating the Poynting vector in the far field and around the dipole[Fig. 2.3].

Quantum yield or efficiency is the measure of fluorescence in the emission process. It is defined as the ratio of emitted photons to the far field to the absorbed photons. Enhancement of quantum yields leads enhancement of emission process.

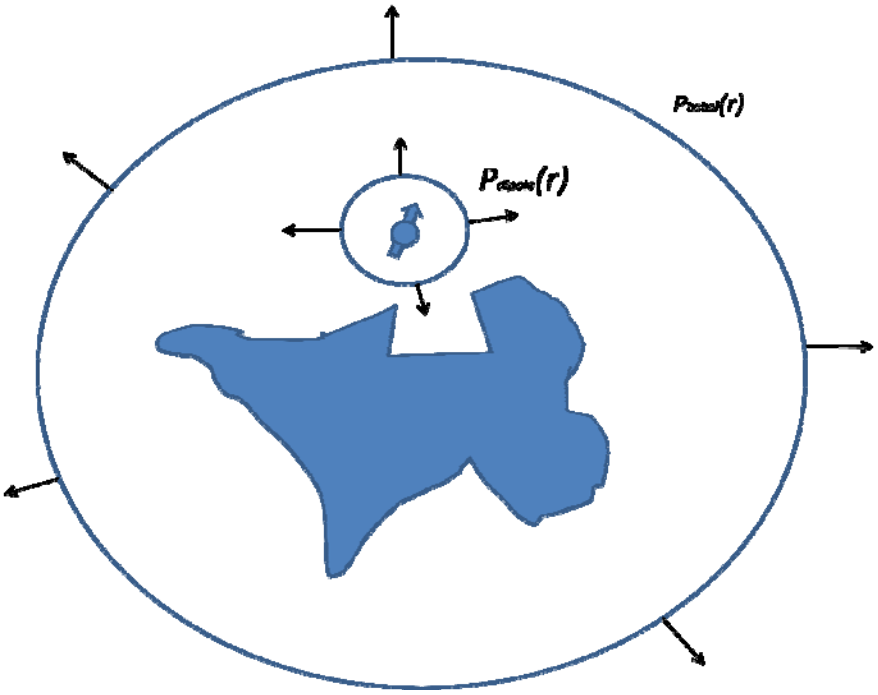

Figure 2.2 Illustration of Poynting vector around the system and the dipole to calculate radiation emitted to farfield and total radiated power by the emitter. The integration surface of Poynting vector around the emitter is infinitely small.

2.4 Total Emission Enhancement

Effect of absorption and emission enhancement derived separately. Thus, we have to combine these two terms in order to get a unified relation. As a result total emission enhancement can be written as,

$$\frac{I}{I_o} = \frac{n(w_{em})}{n_o(w_{em})} \frac{\left|p \cdot E\right|^2}{\left|p \cdot E_o\right|^2} \tag{2.29}$$

where w_{em} is the emission frequency of the emitter. Absorption term can be easily calculated at the emitter location by normalizing the squared value of electric field to the that of free space. Emission enhancement term is the ratio of the new quantum

efficiency to the intrinsic quantum efficiency. However, for most of the measurement systems we can only collect a small portion of the emitted light to the far field.

Therefore, system collection efficiency has to be accounted. It can be inserted to Eq.2.29 by convolving the far field patterns of the emitters by system's collection function, which is related to numerical aperture.

Chapter 3

SURFACE PLASMON POLARITONS

In this chapter basic information about Surface Plasmon Polaritons (SPPs) is provided. Coupling conditions of light to surface plasmons in different geometries are explained. Field distributions, dispersion diagrams of these geometries are also given. Transfer Matrix formulation for one dimensional multilayer medium is introduced for TE and TM modes. Rigorously Coupled Wave Analysis(RCWA) for one dimensional grating structures is derived..

3.1 Surface Plasmons

Surface plasmons waves are coupled oscillations of photons and electrons at the interface of metals and dielectrics. These waves are tightly confined to the interface, they decay evanescently in the perpendicular direction of the interface. The physics of the SPPs can be understood by deriving dispersion relation of SPPs. The dispersion diagram can be took out by solving Maxwell equations on dielectric-metal interface[30].

Dispersion relation of SPPs at metal dielectric interface can be obtained by solving Maxwell equations for TM polarization. The dispersion relation of surface plasmons is given by,

$$k_x = \frac{w}{c}\sqrt{\frac{\varepsilon_m + \varepsilon_d}{\varepsilon_m \varepsilon_d}} \tag{3.1}$$

Dispersion relation for at silver air interface can be realized as in Fig 3.1 using the measured refractive index data in Ref. 31[31]. The dispersion relation of photons in a dielectric medium is given by,

$$k_x = \frac{w}{c}\sqrt{\varepsilon_d} \tag{3.2}$$

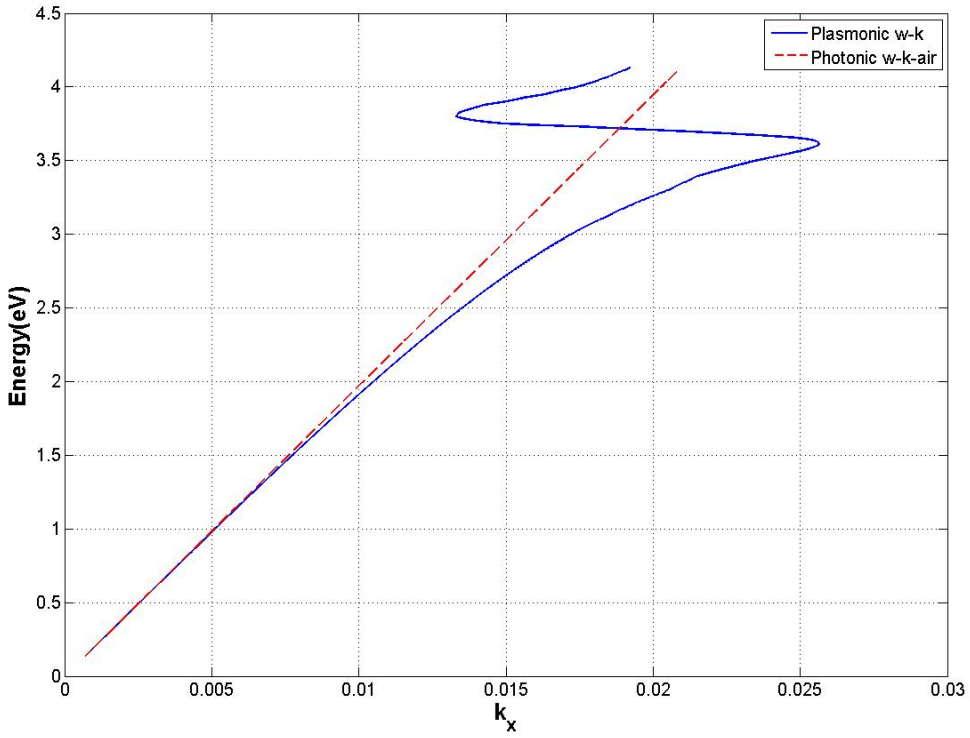

Figure 3.1 Photonic dispersion curve of photons in air and plasmonic dispersion curve of surface plasmons at metal-dielectric interface. Below 3.61 eV dispersion curves do not intersect except the origin and surface plasmons cannot be excited at metal dielectric interface.(For this simulation silver-air interface)

In Fig 3.1, Surface plasmons cannot be directly exited on metal dielectric interface since the dispersion curve of SPPs lies below the dispersion curve of photons. In order to excite surface plasmons at the metal dielectric interface, the slope of photonic dispersion curve has to be changed. This can be done by using techniques such as, prism and grating coupling techniques. Kretschmann and Otto coupling schemes are two prism coupling method to excite surface plasmons.

.3.2 Excitation of SPPs

The mismatch between the momentums can be altered by using a high refractive index medium. The slope of the photonic dispersion curve decreases, so that plasmonic and photonic can overlap as seen in Fig. 3.2. There are two configuration to excite surface plasmons with prism coupling method. These are Kretschmann and Otto

configurations (Fig. 3.3). Otto configuration is a special case of attenuated total internal reflection(ATR). Due to the difficulty of controlling the gap size it is less preferred. In Kretschmann geometry, total internal reflection(TIR) takes place. Tail of the incident light extends to metallic region. If the momentums are matched surface plasmons are excited.

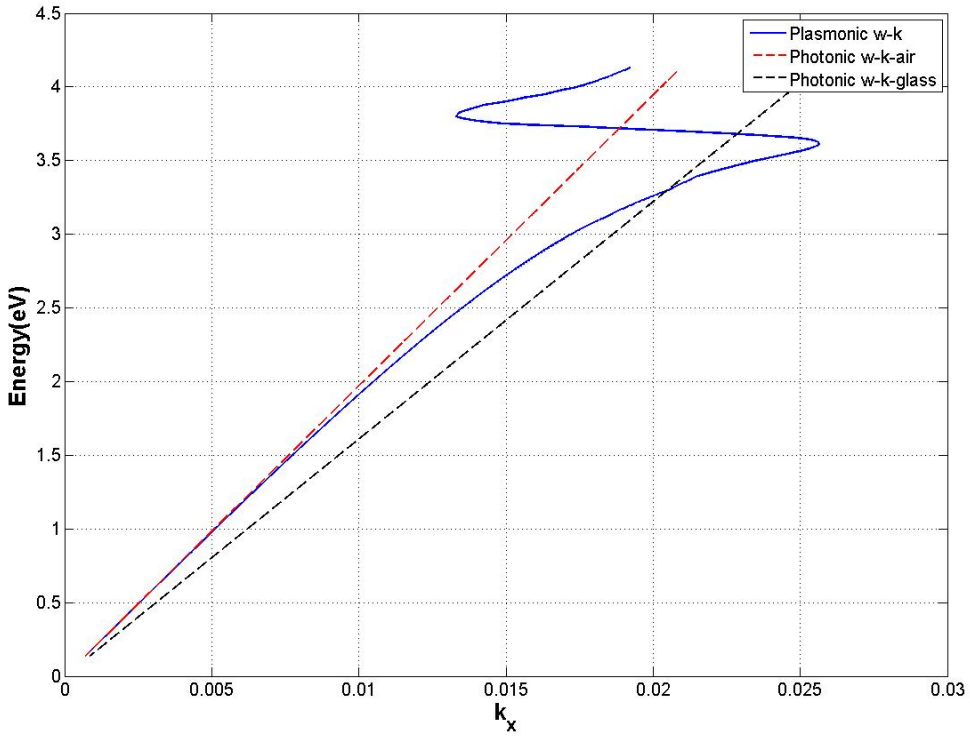

Figure 3.2 Photonic dispersion curve of photons in air, in glass and plasmonic dispersion curve of surface plasmons at metal-dielectric interface. The photonic dispersion curve of photons and dispersion curve of surface plasmons intersect. Excitation of surface plasmons is possible. (For this simulation silver-air and silver-glass interfaces)

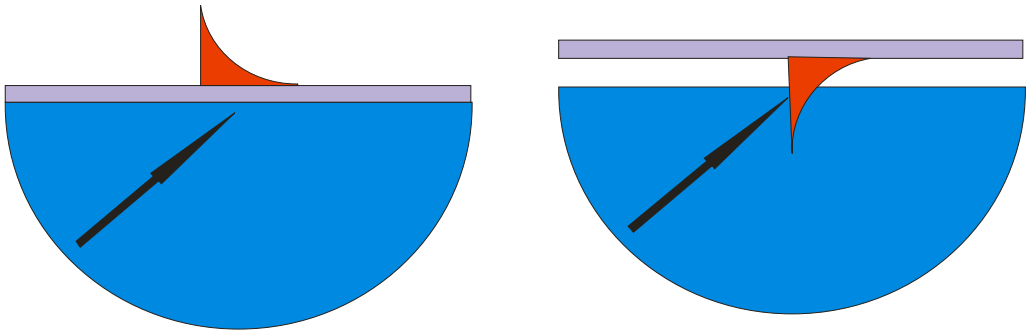

Fig. 3.3 Two prism coupling scheme of surface plasmons. Kretshcmann(a) and Otto(b) configuration. In Kretshcmann configuration, total internal reflection(TIR) takes place. The tail of incident light from prism extended to the metallic region. In Otto configuration attenuated total reflection (ATR) takes place. The tail of incident wave tunnels to the metal surface. Surface plasmons are excited if the horizontal component of momentum of incident light matches the surface plasmons momentum.

Another surface plasmon excitation scheme is grating coupling configuration. In gratings the refractive index changes spatially due to the corrugation on the structure. When a light incident on this structure, it diffracts into the many orders that have different momentums. Surface plasmons are excited when the x component of momentum of a diffracted order is equal to surface plasmon momentum vector.

$$k_{spp} = k\sin(\alpha) \pm mG \tag{3.3}$$

where G is the grating vector and given by $G = \frac{2\pi}{\Lambda}$. Λ is the period of the grating. The dispersion relation of grating is expressed by inserting Eq.1 into Eq.3 as,

$$k_{spp} = \frac{w}{c}\sqrt{\frac{\varepsilon_m + \varepsilon_d}{\varepsilon_m \varepsilon_d}} \pm mG \tag{3.4}$$

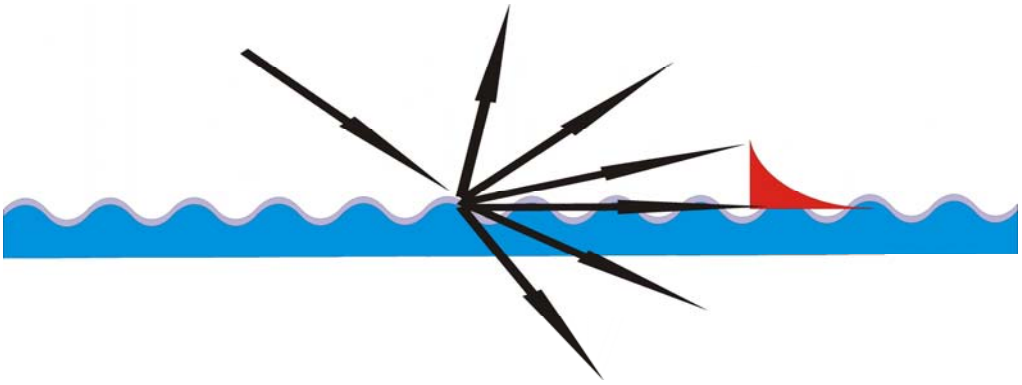

Figure 3.4 Grating coupling scheme; Incident light is diffracted into many orders. If the horizontal components of momentums of diffracted orders are matched with the surface plasmons momentum on metal dielectric interface, then surface plasmons are excited. At many wavelengths, excitation of surface plasmons are possible.

Surface plasmons are excited at both interfaces of metal. The dispersion relation given by Eq. 3.4 can be plotted at metal air and metal-dielectric interfaces as in Fig. 3.5.. The dispersion curves are calculated for the first three orders. SPPs can be excited by sending light to metal dielectric interface or the metal air interface.

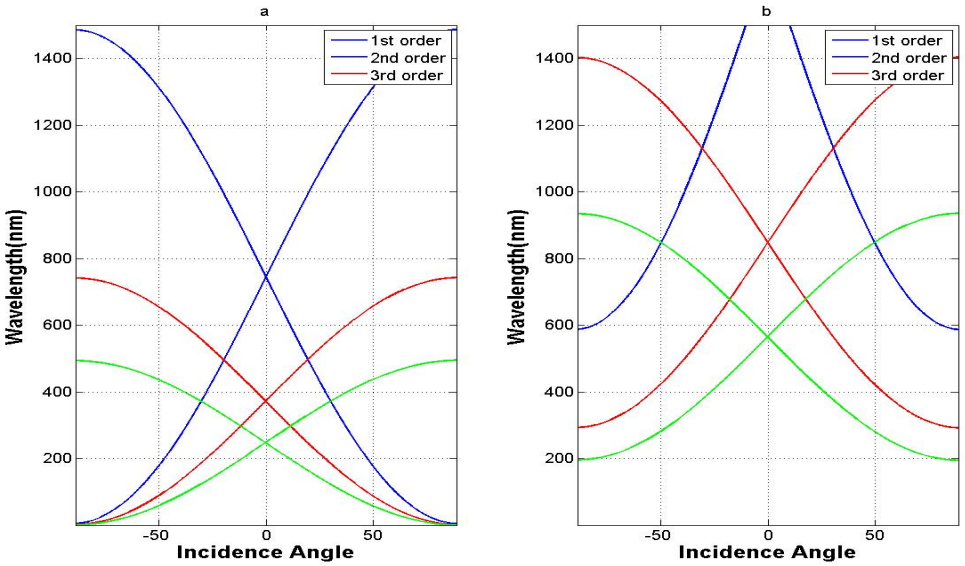

Figure 3.5 Dispersion relation of SPPs. Strong dependence of dispersion relation to the dielectric function is illustrated. Surface plasmons can be excited both on metal-air interface(a) and metal-dielectric interface(b). Dispersion relation due to first three orders are highlighted.

3.3 Transfer Matrix Method

The dispersion relations can be evaluated by using Fresnel formulas derived from the Maxwell Equations. For the structures shown in Fig. 3.3 it can be solved analytically by matching the boundary conditions at the interfaces. On the other hand, Transfer Matrix Method(TMM) which is generally used to calculate transmission and reflection characteristics of a multilayer structure, can be utilized to determine dispersion relation for Kretschmann and Otto SPP coupling schemes. Furthermore, for an arbitrary metallic multilayer structure, dispersion relation can be easily evaluated.

Consider multilayer structure, which has L uniform layers with refractive indices $n_1, n_2, n_3 ..... n_L$ and thicknesses $d_1, d_2, d_3 ..... d_L$ as seen Fig. 3.6. For a TE polarized wave, Electric fields in each layer can be written in the form,

$$E_o = \left[e^{-ik_{1z}z} + Re^{-ik_{1z}z} \right] e^{-ik_x x} \qquad \text{for z<0}$$

$$E_l = \left[A_l e^{-k_o \gamma_l (z - Z_{l-1})} + B_l e^{k_o \gamma_l (z - Z_l)} \right] e^{-ik_x x} \text{ for } Z_{l-1} \le z \le Z_l \qquad (3.5)$$

$$E_t = \left[Te^{-ik_{1z}(z - Z_l)} \right] e^{-ik_x x} \qquad \text{for } z > Z_l$$

where $k_{2z} = k_0 \sqrt{(n_2^2 - n_1^2 \sin^2(\theta))}$ and $\gamma_l = i\sqrt{(n_l^2 - n_1^2 \sin^2(\theta))}$. R and T are the reflection and transmission coefficients. A and B are the amplitudes of electric field in each slab Now we can solve Maxwell equations for each layer. From continuity equations at the boundary of 0^{th} and 1^{st} layers,

$$\begin{aligned} 1 + R &= A_1 + B_1 e^{-k_o \gamma_l d_1} \\ i\frac{k_{1z}}{k_0}(1 - R) &= \gamma_1 [A_1 - B_1 e^{-k_o \gamma_l d_1}] \end{aligned} \quad \text{at z=0} \qquad (3.6)$$

At the boundary of l^{th} and $(l\text{-}1)^{th}$ layer,

$$\begin{aligned} A_{l-1} e^{-k_o \gamma_{l-1} d_{l-1}} + B_{l-1} &= A_l + B_l e^{-k_o \gamma_l d_l} \\ \gamma_{l-1} [A_{l-1} e^{-k_o \gamma_{l-1} d_{l-1}} - B_{l-1}] &= \gamma_l [A_l - B_l e^{-k_o \gamma_l d_l}] \end{aligned} \qquad (3.7)$$

At the boundary of last layer and *(L-1)* th layer,

$$\begin{aligned} A_L e^{-k_o \gamma_L d_L} + B_L &= T \\ \gamma_L [A_L e^{-k_o \gamma_L d_L} - B_L] &= i \frac{k_{1z}}{k_0} T \end{aligned} \tag{3.8}$$

From Eqs. 3.6-8 , for an L homogeneous layers there are $2(L-1)$ equations. These system of equations can be solved simultaneously for R and T by using basic linear algebra techniques for any refractive indices and any number of layers L.

Using Eq. 3.8 at the Lth boundary we get the matrix equation for the A and B coefficients,

$$\begin{bmatrix} e^{-k_o \gamma_L d_L} \gamma_L & 1 \\ e^{-k_o \gamma_L d_L} \gamma_L & -\gamma_L \end{bmatrix} \begin{bmatrix} A_L \\ B_L \end{bmatrix} = \begin{bmatrix} 1 \\ i \frac{k_{1z}}{k_0} \end{bmatrix} T \tag{3.9}$$

which can be written in the form of ,

$$\begin{bmatrix} A_L \\ B_L \end{bmatrix} = \begin{bmatrix} e^{-k_o \gamma_L d_L} \gamma_L & 1 \\ e^{-k_o \gamma_L d_L} \gamma_L & -\gamma_L \end{bmatrix}^{-1} \begin{bmatrix} 1 \\ i \frac{k_{1z}}{k_0} \end{bmatrix} T \tag{3.10}$$

Coupled equation at the (L-1)th and 1st boundary can also be transformed into matrix form as,

$$\begin{bmatrix} e^{-k_o \gamma_{l-1} d_{l-1}} & 1 \\ \gamma_{l-1} e^{-k_o \gamma_{l-1} d_{l-1}} & -\gamma_{l-1} \end{bmatrix} \begin{bmatrix} A_{l-1} \\ B_{l-1} \end{bmatrix} = \begin{bmatrix} 1 & e^{-k_o \gamma_l d_l} \\ \gamma_l & -\gamma_l e^{-k_o \gamma_l d_l} \end{bmatrix} \begin{bmatrix} A_l \\ B_l \end{bmatrix} \tag{3.11}$$

$$\begin{bmatrix} 1 \\ i \frac{k_{1z}}{k_0} \end{bmatrix} + \begin{bmatrix} 1 \\ -i \frac{k_{1z}}{k_0} \end{bmatrix} R = \begin{bmatrix} 1 & e^{-k_o \gamma_l d_1} \\ \gamma_1 & -\gamma_1 e^{-k_o \gamma_l d_1} \end{bmatrix} \begin{bmatrix} A_1 \\ B_1 \end{bmatrix} \tag{3.12}$$

where Eq. 3.11 is simplified into the equation,

$$\begin{bmatrix} A_{l-1} \\ B_{l-1} \end{bmatrix} = \begin{bmatrix} e^{-k_o \gamma_{l-1} d_{l-1}} & 1 \\ \gamma_{l-1} e^{-k_o \gamma_{l-1} d_{l-1}} & -\gamma_{l-1} \end{bmatrix}^{-1} \begin{bmatrix} 1 & e^{-k_o \gamma_l d_l} \\ \gamma_l & -\gamma_l e^{-k_o \gamma_l d_l} \end{bmatrix} \begin{bmatrix} A_l \\ B_l \end{bmatrix} \tag{3.13}$$

Let'sdefine, $V_l = \begin{bmatrix} 1 & e^{-k_o\gamma_l d_l} \\ \gamma_l & -\gamma_l e^{-k_o\gamma_l d_l} \end{bmatrix}$, $U_l = \begin{bmatrix} e^{-k_o\gamma_l d_l} & 1 \\ \gamma_{l-1}e^{-k_o\gamma_l d_l} & -\gamma_l \end{bmatrix}$, $\underline{X_l} = \begin{bmatrix} A_l \\ B_l \end{bmatrix}$, then Eq. 3.13 can be written as,

$$\underline{X_{l-1}} = U_{l-1}^{-1} V_l \underline{X_l} \tag{3.14}$$

Repeating Eq. 3.14 for each layer, we get the recursive relation between 1st and Lth electric field components,

$$\underline{X_1} = U_1^{-1}\left(\prod_{l=2}^{L-1} V_l U_l\right) V_L \underline{X_L} \tag{3.15}$$

By replacing Eqs.3.10-15 into Eq.3.12, we get

$$\begin{bmatrix} 1 \\ i\frac{k_{1z}}{k_0} \end{bmatrix} + \begin{bmatrix} 1 \\ -i\frac{k_{1z}}{k_0} \end{bmatrix} R = V_1 U_1^{-1}\left(\prod_{l=2}^{L-1} V_l U_l^{-1}\right) V_L U_L \begin{bmatrix} 1 \\ i\frac{k_{1z}}{k_0} \end{bmatrix} T \tag{3.16}$$

which can be simplified as,

$$\begin{bmatrix} 1 \\ i\frac{k_{1z}}{k_0} \end{bmatrix} + \begin{bmatrix} 1 \\ -i\frac{k_{1z}}{k_0} \end{bmatrix} R = \left(\prod_{l=1}^{L} V_l U_l^{-1}\right) \begin{bmatrix} 1 \\ i\frac{k_{1z}}{k_0} \end{bmatrix} T \tag{3.17}$$

where, $V_l = \begin{bmatrix} 1 & e^{-k_o\gamma_l d_l} \\ \gamma_l & -\gamma_l e^{-k_o\gamma_l d_l} \end{bmatrix}$ and $U_l = \begin{bmatrix} e^{-k_o\gamma_l d_l} & 1 \\ \gamma_{l-1}e^{-k_o\gamma_l d_l} & -\gamma_l \end{bmatrix}$

In Eq. 3.17, reflection and transmission coefficients are coupled. To solve this equation, the vector on the right hand side and the vector of the reflection coefficients are combined.

Let $\underline{W} = \left(\prod_{l=1}^{L} V_l U_l^{-1} \right) \begin{bmatrix} 1 \\ i\frac{k_{1z}}{k_0} \end{bmatrix}$ and $\underline{K} = \begin{bmatrix} 1 \\ -i\frac{k_{1z}}{k_0} \end{bmatrix}$, then Eq. 3.17 can be written in matrix form as,

$$\begin{bmatrix} 1 \\ i\frac{k_{1z}}{k_0} \end{bmatrix} = \begin{bmatrix} -K & W \end{bmatrix} \begin{bmatrix} R \\ T \end{bmatrix} \tag{3.18}$$

Finally, reflection and transmission coefficients can be calculated using Eq. 3.18 as,

$$\begin{bmatrix} R \\ T \end{bmatrix} = \begin{bmatrix} -K & W \end{bmatrix}^{-1} \begin{bmatrix} 1 \\ i\frac{k_{1z}}{k_0} \end{bmatrix} \tag{3.19}$$

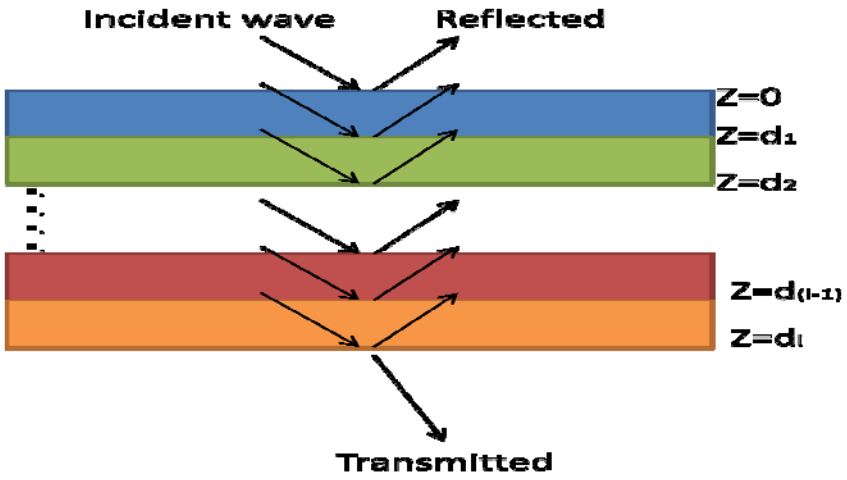

Figure 3.6 Reflection and Transmission from a multilayer system. For each interface, backward and forward reflected waves are shown. At each interface horizontal and magnetic fields are matched due to continuity equation Matching horizontal components of electric and magnetic field for each layer iteratively results the relation between incident, reflected and transmitted waves.

The formulation for TM-polarization case is quite similar to those of Eqs. 3.5-19, however γ_l is replaced by $\frac{\gamma_l}{n_l^2}$ except in the exponents , k_{1z} and k_{2z} are replaced by $\frac{k_{1z}}{n_1^2}$ and $\frac{k_{2z}}{n_2^2}$.

3.4 Dispersion of SPPs using TMM

The dispersion curves of SPPs in Otto and Kretschmann configurations can be evaluated by solving directly Maxwell equations at the interface (Fig. 3.1 and 3.2). On the other hand, TMM can be applied to simulate dispersion curves of SPPs for both Otto and Kretschmann configurations. Moreover TMM can also be used to analyze multilayer plasmonic structures, such as MIM(metal insulator metal), IMI(insulator metal insulator). TMM method can also be used to analyze DBR(Distributed Bragg Reflectors). Figure 3.6-7 shows the reflection data for excitation wavelength of 532nm and dispersion curve for Kretschmann configuration. Figure 3.8-9 shows the reflectivity simulation for excitation wavelength of 532nm and dispersion curve for Otto configuration. Refractive index of dielectric layer is 1.5 for both configurations. Silver is used as plasmonic layer with a thickness of 50nm for Kretschmann coupling scheme. For Otto configuration the thickness of silver layer is assumed infinity. All simulations are done for TM polarization, which supports surface plasmon modes.

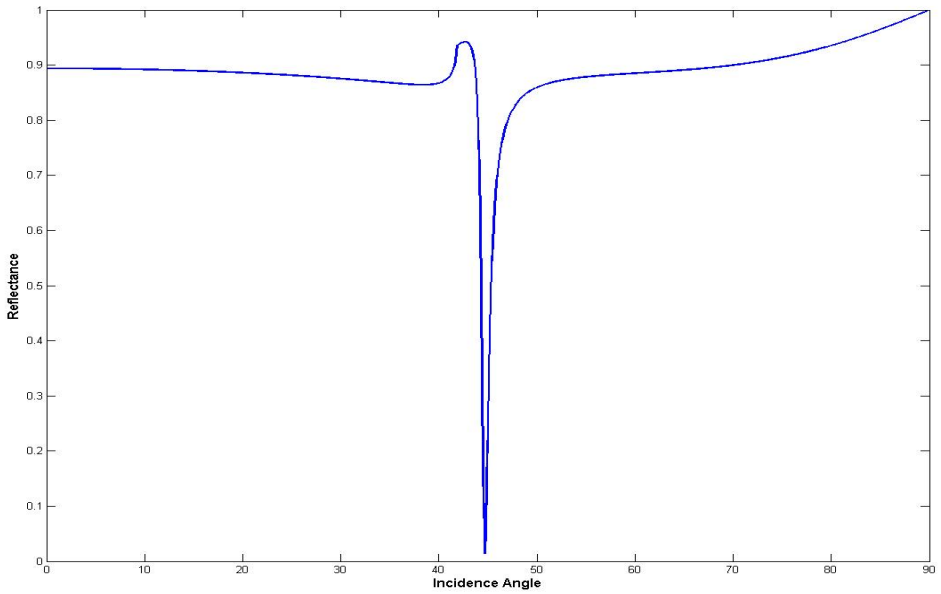

Figure 3.6 Simulated reflectivity vs. angle for Kretschmann coupling scheme using transfer matrix method. Silver is used as metallic layer. For incident wavelength of 532nm, surface plasmons are excited at 45 degrees.

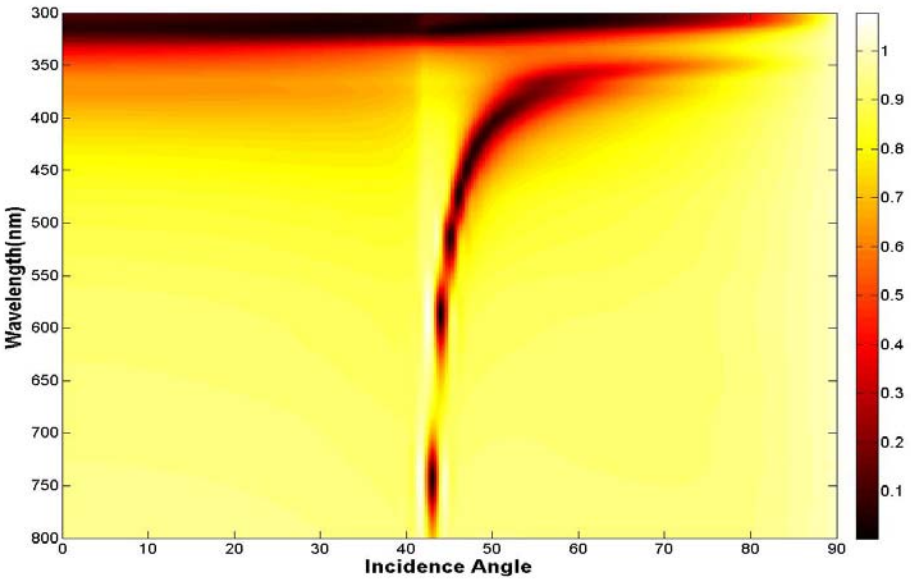

Figure 3.7 Dispersion relation for Kretschmann SPP Coupling Scheme obtained using transfer matrix method. For each wavelength angle resolved reflectivity is calculated. The discreteness of curve for higher wavelengths is due to the interpolation of simulation result.

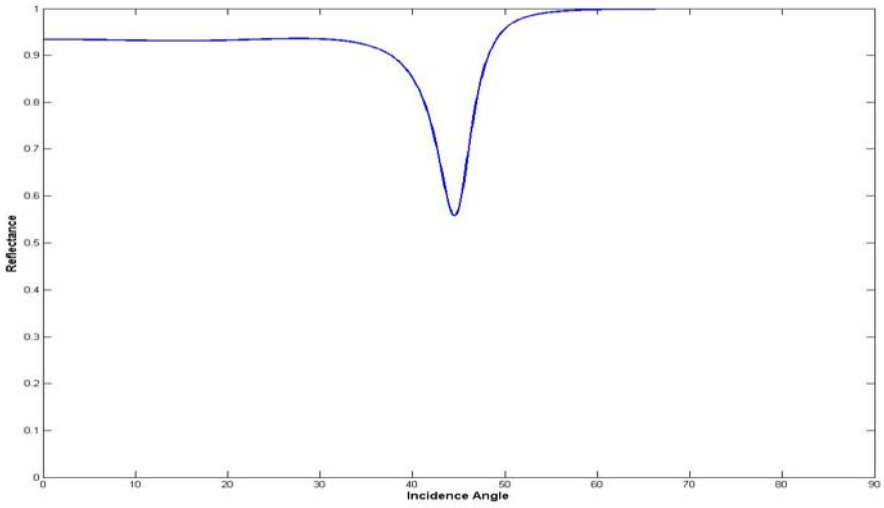

Figure 3.8 Simulated reflectivity vs. angle for Otto coupling scheme using transfer matrix method. Silver is used as metallic layer. For incident wavelength of 532nm, surface plasmons are excited at 45 degrees. Reflectivity strongly depends on the separation between air and metal. For this simulation it is 250nm.

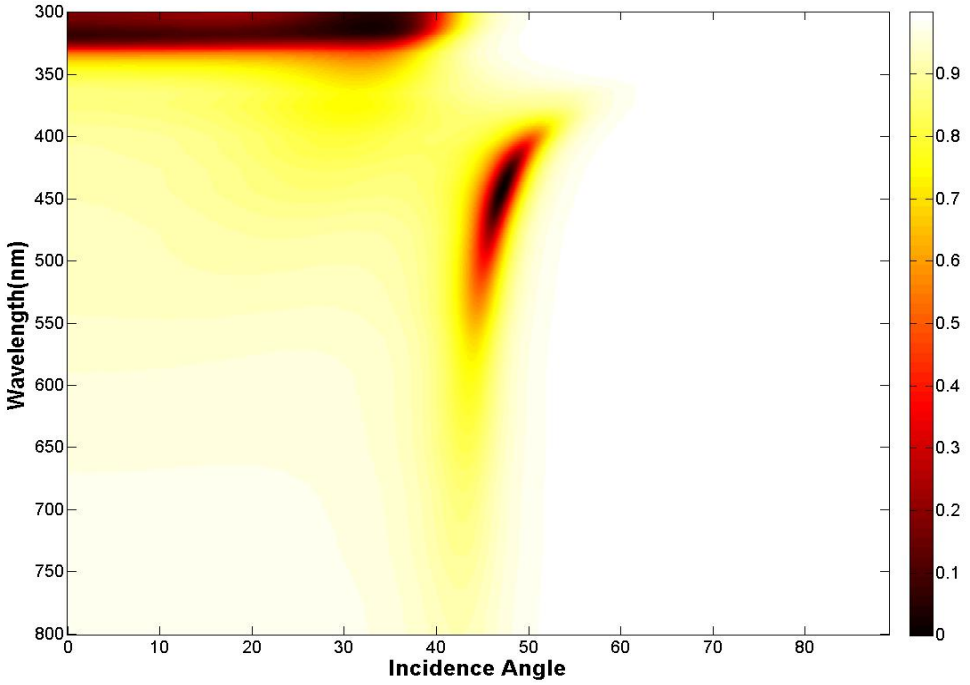

Figure 3.9 Dispersion relation for Otto SPP Coupling Scheme obtained using transfer matrix method. For each wavelength angle resolved reflectivity is calculated. The separation is 250nm. Silver is used as metallic layer.

Field distributions of Kretschmann and Otto configurations are shown in Figures 3.10-13. For Kretschmann geometry, an excitation wavelength of 532nm is used. The field distributions at the resonance conditions prove the accuracy of transfer matrix method (TMM). The field distributions are calculated using a commercial FDTD program[28]. From Figures 3.10-11, for Kretschmann configuration y component of electric field intensity increases 30 fold at the metal air interface for an incidence angle of 45 degrees due to reflection minima [Fig. 3.6]

For Otto configuration, Figures 3.12-13 shows us the imaginary and real parts of x component of electric field. The bars on the right hand sides of figures proves the strong coupling of light to surface plasmons to the surface at the reflection minima[Fig. 3.8]

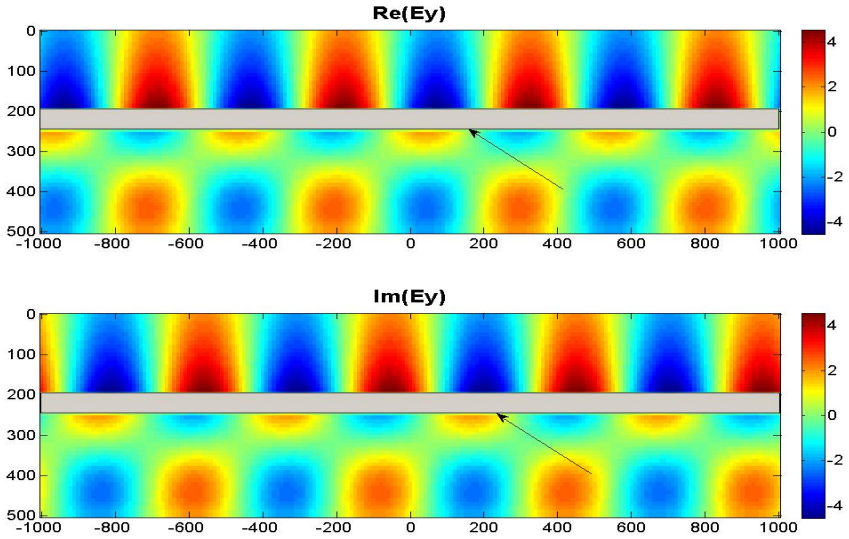

Figure 3.10 Real and Imaginary parts of y component of electric field distribution for an incidence angle of 45 for Kretschmann coupling scheme. Surface plasmons are excited at metal-air interface. White layer indicates the silver layer. Wavelength of incident light is 532nm

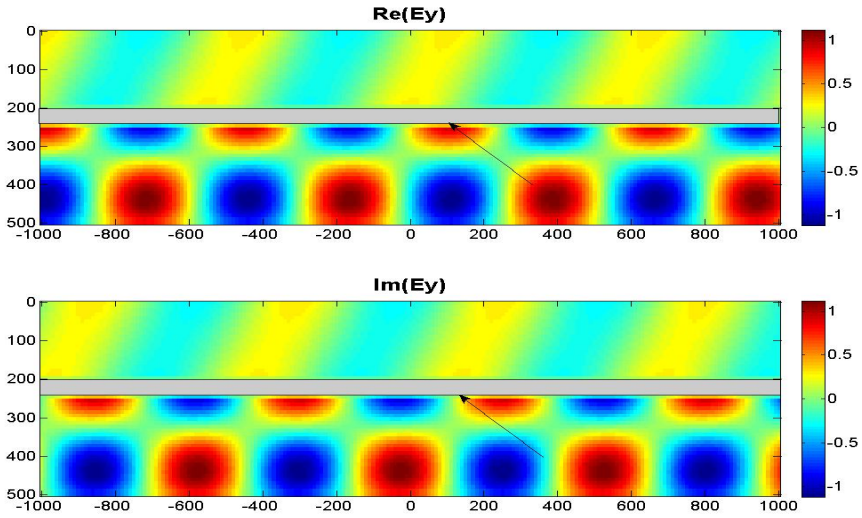

Figure 3.11 Real and Imaginary parts of y component of electric field distribution for an incidence angle of 40 for Kretschmann coupling scheme. Incident light is almost reflected from the silver layer. Wavelength of incident light is 532nm

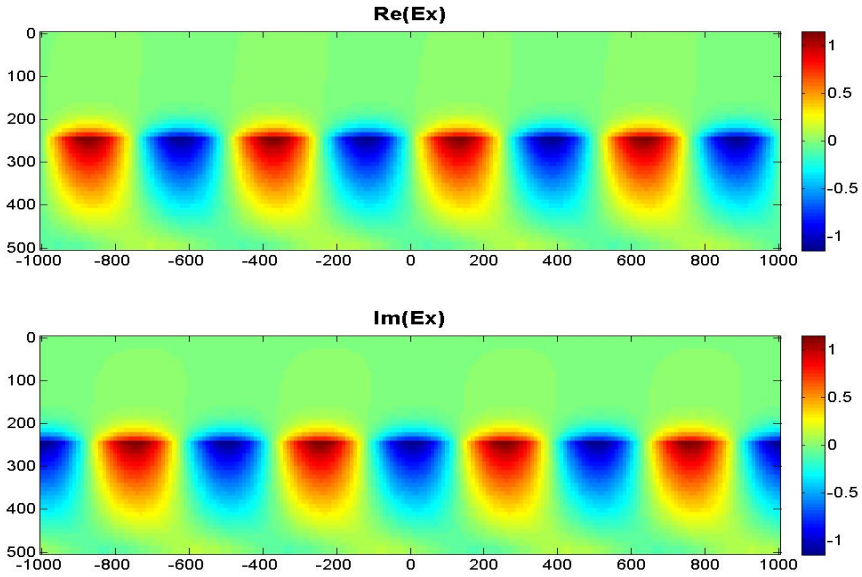

Figure 3.12 Real and Imaginary parts of x component of electric field distribution for an incidence angle of 45 for Otto coupling scheme. Surface plasmons are excited at metal-air interface. The thickness of silver layer assumed infinite. The separation is 250nm. Wavelength of incident light is 532nm

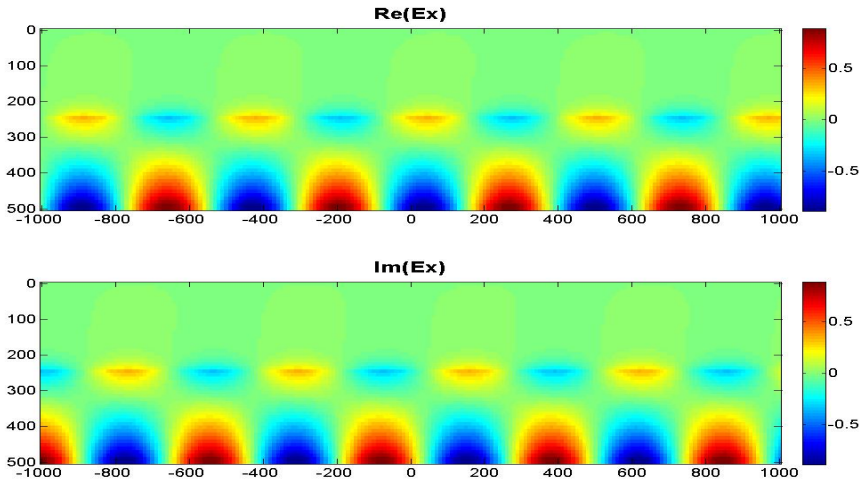

Figure 3.13 Real and Imaginary parts of y component of electric field distribution for an incidence angle of 40 for Otto coupling scheme. Incident light is almost reflected from the silver layer. Surface plasmons are still excited on metal surface. That can be explained from wider reflectivity curve[Fig.3.8]. Wavelength of incident light is 532nm

3.3 Rigorous Coupled Wave Analysis(RCWA)

Rigorous coupled wave analysis(RCWA) has been used to analysis and design of diffractive structures. It is an exact solution to the Maxwell's equations for grating structures. This technique was initially used to design holographic gratings, then it was extended to surface-relief and multilevel grating structures[32]. RCWA is also applied to analyze the transmission, reflection and absorption characteristics of metallic gratings. Furthermore, RCWA can be extended to analyze two and three dimensional plasmonic and photonic structures[34-35]. The accuracy of solution depends on the terms used in the space-harmonic representation of the fields. In this technique, grating is divided into a large number of thin planar slabs which are also grating structures. As the number of these slabs increases the accuracy of diffracted orders increases. Then electromagnetic boundary conditions, the continuity of tangential components of electrical and magnetic components are applied at the output region, grating slabs and input interfaces respectively.

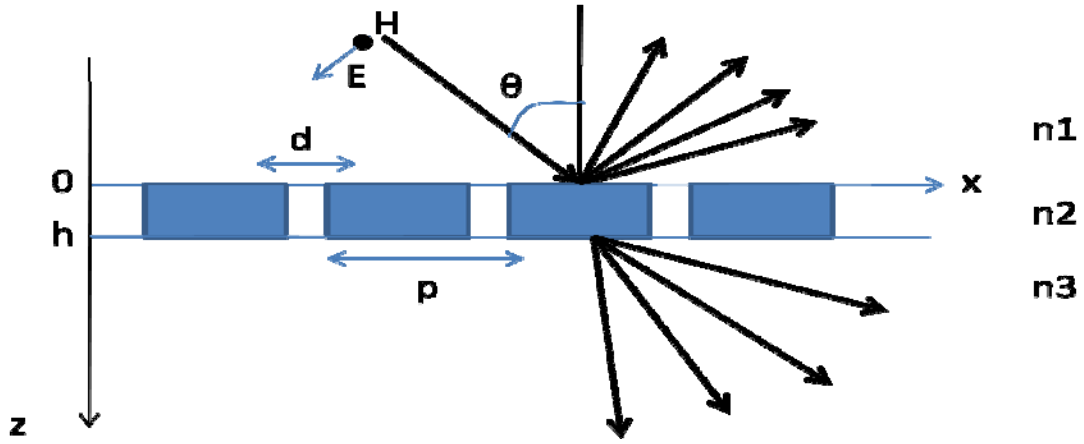

Figure 3.14 Periodically modulated metallic grating structure with a period of p, slit width of d and a film thickness h. In the second region dielectric function can be expanded into Fourier Series due to periodicity of dielectric function. In the second region electric and magnetic field components are written in terms of each diffracted order.

In Fig. 3.14, the dielectric function of system is constant for z<0 and for z>h. In the second region the dielectric function of system is modulated(0<z<h). The dielectric function can be expanded into Fouriers series as,

$$\varepsilon_2(x) = \sum_n \varepsilon_n e^{jngx} \tag{3.20}$$

where n is an integer and g i the reciprocal period of lattice and expressed as, $g = 2\pi / p$.

Then, the fourier components of dielectric function given by Eq. 3.20 is expressed as,

$$\begin{aligned} \varepsilon_0 &= f\varepsilon_s + (1-f)\varepsilon_m \\ \varepsilon_n &= (\varepsilon_s - \varepsilon_m)\frac{\sin(n\pi f)}{n\pi} \end{aligned} \tag{3.21}$$

where f=d/p and ε_s , ε_m are the dielectric functions of metal and dielectric in region 2.

For TM polarized wave, magnetic field component of incident wave can be written as,

$$H_{0y} = \exp(-i(k_{1x}x + k_{1z}z)) \tag{3.22}$$

where $k_{1x} = k_o\sqrt{\varepsilon_1}\sin(\theta)$ and $k_{1z} = k_o\sqrt{\varepsilon_1}\cos(\theta)$. Incident light is diffracted to multiple waves due to the modulated structure. The inplane wave vectors of diffracted orders are given by $k_{nx} = k_{1x} + ng$.

In regions 1 and 3 reflected and diffracted waves can be expressed as,

$$\begin{aligned} H_{1y} &= H_{0y} + \sum_n r_n \exp(-i(k_{nx}x - k_{nz1}z)) \\ H_{3y} &= \sum_n t_n \exp[-i(k_{nx}x + k_{nz3}(z-h))] \end{aligned} \tag{3.23}$$

with $k_{nzi}^{\ 2} = k_i^{\ 2} - k_{nx}^{\ 2}$. r_n and t_n are the amplitude of reflected and transmitted magnetic field of order n. The total electric and magnetic fields can be found in regions 1 and 3 from Maxwell's equation,

$$E = \left(\frac{-i}{w\varepsilon_f\varepsilon}\right)\nabla \times H \tag{3.24}$$

In the second region Eq.3.24 can be written as,

$$\frac{\partial H_{2y}}{\partial z} = -iw\varepsilon_f \varepsilon(x) E_{2x}$$
$$\frac{\partial E_{2x}}{\partial z} = -iw\mu_0 H_{2y} + \frac{\partial E_{2z}}{\partial x} \tag{3.25}$$

Since the dielectric function of second region is modulated the tangential electric and magnetic field components can be expresses as(Bloch's theorem),

$$H_{2y} = \sum_n H_{2n}(z)\exp(-i(k_{nx}x))$$
$$E_{2x} = i\left(\frac{\mu_0}{\varepsilon_f}\right)\sum_n E_{2n}(z)\exp(-i(k_{nx}x)) \tag{3.26}$$

Substituting Eq.3.26 into Eq.3.24 and after some algebraic operations we get some coupled equations of harmonics $H_{2n}(z)$, $E_{2n}(z)$ written in the matrix form as,

$$\frac{\partial [H_2]}{\partial z} = k_0 [\varepsilon][E_2] \tag{3.27}$$

$$\frac{\partial [E_2]}{\partial z} = k_0 (K_x [\varepsilon]^{-1} K_x - I)[H_2] \tag{3.28}$$

Then the derivative of Eq.3.27 is substituted into Eq.3.28 and we get ,

$$\frac{\partial^2 [E_2]}{\partial z^2} = k_0{}^2 (K_x [\varepsilon]^{-1} K_x - I)[\varepsilon][E_2] \tag{3.29}$$

$$\frac{\partial^2 [H_2]}{\partial z^2} = k_0{}^2 [\varepsilon](K_x [\varepsilon]^{-1} K_x - I)[H_2] \tag{3.30}$$

where $[\varepsilon]$ is the Toeplitz matrix generated by the fourier coefficients of $\varepsilon(x)$ such that its (m-n)th element is ε_{n-m}. I is the identity matrix. K_x is the diagonal matrix with elements $\frac{k_{nx}}{k_0}$. $[H_2]$ and $[E_2]$ are the field vectors of magnetic and electric fields given by Eq. 3.26. All the matrices in Eq.3.29 are N by N, where N is the number of harmonics used in fourier expansion of fields.

The solution to differential Eq. 3.29 can be evaluated from the eigenvalues and eigenvectors of matrix product $k_0^2(K_x[\varepsilon]^{-1}K_x - I)[\varepsilon]$. The spatial harmonics $E_{2n}(z)$ is expressed as,

$$E_{2n}(z) = \sum_m E_{n,m}[W_m^+ \exp(-k_0 q_m z) + W_m^- \exp(k_0 q_m (z-h))] \tag{3.31}$$

where q_m is the positive square root of eigenvalues of matrix $k_0^2(K_x[\varepsilon]^{-1}K_x - I)[\varepsilon]$, W_m^+ and W_m^- are the amplitudes of forward and backward travelling waves to be determined, $E_{n,m}$ is the elements of eigenvector matrix $[E]$. Substituting Eq.3.31 into Eq.3.25, we get similar results for the spatial harmonics of magnetic field component.

$$H_{2n}(z) = \sum_m H_{n,m}[-W_m^+ \exp(-k_0 q_m z) + W_m^- \exp(k_0 q_m (z-h))] \tag{3.32}$$

The amplitudes W_m^+, W_m^-,reflection coefficients(r_n) and transmission coefficients(t_n) can be determined by matching the tangential components of electric and magnetic field at the boundaries. At z=0,

$$\begin{aligned} \delta_{no} + r_n &= \sum_{m=1}^{N} H_{n,m}[-W_m^+ + W_m^- \exp(-k_0 q_m h)] \\ -\frac{k_{1zn}}{\varepsilon_1}\delta_{no} + \frac{k_{1zn}}{\varepsilon_1} r_n &= \sum_{m=1}^{N} -iE_{n,m}[W_m^+ + W_m^- \exp(-k_0 q_m h)] \end{aligned} \tag{3.33}$$

At the output boundary (z=h),

$$\begin{aligned} t_n &= \sum_{m=1}^{N} H_{n,m}[-W_m^+ \exp(-k_0 q_m h) + W_m^-] \\ \frac{k_{3zn}}{\varepsilon_3} t_n &= \sum_{m=1}^{N} iE_{n,m}[W_m^+ \exp(-k_0 q_m h) + W_m^-] \end{aligned} \tag{3.34}$$

Eqs. 3.33-34 are written for only for a harmonic. If one introduce these equations for every harmonics, a matrix form is obtained.

$$\begin{aligned} \underline{\delta}_{no} + \underline{r} &= -\underline{\underline{H}}\,\underline{W}^+ + \underline{\underline{H}}\,\underline{\underline{X}}\,\underline{W}^- \\ -\frac{k_{1zn}}{\varepsilon_1}\underline{\delta}_{no} + \frac{k_{1zn}}{\varepsilon_1}\underline{r} &= -i\underline{\underline{E}}\,\underline{W}^+ - i\underline{\underline{E}}\,\underline{\underline{X}}\,\underline{W}^- \end{aligned} \tag{3.35}$$

$$\begin{aligned} \underline{t} &= -\underline{\underline{H}}\,\underline{\underline{X}}\,\underline{W}^{+} + \underline{\underline{H}}\,\underline{W}^{-} \\ \frac{k_{3zn}}{\varepsilon_3}\underline{t} &= i\underline{\underline{E}}\,\underline{\underline{X}}\,\underline{W}^{+} + i\underline{\underline{E}}\,\underline{W}^{-} \end{aligned} \tag{3.36}$$

where $\underline{\underline{X}}$ is the diagonal matrix with elements $\exp(-k_0 q_m h)$. $\underline{W}^{+}$ and $\underline{W}^{-}$ are the coefficient vector of forward and backward scattered waves. $\underline{t}$ and $\underline{r}$ are the transmission and reflection vectors. Furthermore, Eqs. 3.35-36 can be written more compact matrix form as,

$$\begin{aligned} \begin{bmatrix} -\underline{\underline{H}} & \underline{\underline{H}}\,\underline{\underline{X}} \\ -i\underline{\underline{E}} & -i\underline{\underline{E}}\,\underline{\underline{X}} \end{bmatrix} \begin{bmatrix} \underline{W}^{+} \\ \underline{W}^{-} \end{bmatrix} &= \begin{bmatrix} \underline{\delta}_{no} \\ -\dfrac{k_{1zn}}{\varepsilon_1} \end{bmatrix} + \begin{bmatrix} I \\ Z_1 \end{bmatrix} r \\ \begin{bmatrix} -\underline{\underline{H}}\,\underline{\underline{X}} & \underline{\underline{H}} \\ i\underline{\underline{E}}\,\underline{\underline{X}} & i\underline{\underline{E}} \end{bmatrix} \begin{bmatrix} \underline{W}^{+} \\ \underline{W}^{-} \end{bmatrix} &= \begin{bmatrix} I \\ Z_3 \end{bmatrix} t \end{aligned} \tag{3.37}$$

where I is the identity matrix, Z_1 and Z_3 are the diagonal matrices with elements $-\dfrac{k_{1zn}}{\varepsilon_1}$ and $\dfrac{k_{3zn}}{\varepsilon_3}$.

After eliminating amplitude vectors, we get the following relation

$$\begin{bmatrix} -\underline{\underline{H}} & \underline{\underline{H}}\,\underline{\underline{X}} \\ -i\underline{\underline{E}} & -i\underline{\underline{E}}\,\underline{\underline{X}} \end{bmatrix} \begin{bmatrix} -\underline{\underline{H}}\,\underline{\underline{X}} & \underline{\underline{H}} \\ i\underline{\underline{E}}\,\underline{\underline{X}} & i\underline{\underline{E}} \end{bmatrix}^{-1} \begin{bmatrix} I \\ Z_3 \end{bmatrix} t = \begin{bmatrix} \underline{\delta}_{no} \\ -\dfrac{k_{1zn}}{\varepsilon_1} \end{bmatrix} + \begin{bmatrix} I \\ Z_1 \end{bmatrix} r \tag{3.38}$$

which can be simplified as,

$$A\,t = \begin{bmatrix} \underline{\delta}_{no} \\ -\dfrac{k_{1zn}}{\varepsilon_1} \end{bmatrix} + B\,r \tag{3.39}$$

with $A = \begin{bmatrix} -\underline{\underline{H}} & \underline{\underline{H}}\,\underline{\underline{X}} \\ -i\underline{\underline{E}} & -i\underline{\underline{E}}\,\underline{\underline{X}} \end{bmatrix} \begin{bmatrix} -\underline{\underline{H}}\,\underline{\underline{X}} & \underline{\underline{H}} \\ i\underline{\underline{E}}\,\underline{\underline{X}} & i\underline{\underline{E}} \end{bmatrix}^{-1} \begin{bmatrix} I \\ Z_3 \end{bmatrix}$ and $B = \begin{bmatrix} I \\ Z_1 \end{bmatrix}$. Finally Transmission and reflection coefficients can be found as,

$$\begin{bmatrix} t \\ r \end{bmatrix} = \begin{bmatrix} A & -B \end{bmatrix} \begin{bmatrix} \delta_{no} \\ -\dfrac{k_{1zn}}{\varepsilon_1} \end{bmatrix} \tag{3.40}$$

Diffraction efficiencies of each order is given by,

$$\begin{aligned} R_n &= r_n r_n^* \,\mathrm{Re}\left[\frac{k_{1zn}}{k_0 n_1 \cos(\theta)}\right] \\ T_n &= t_n t_n^* \,\mathrm{Re}\left[\frac{n_1 k_{3zn}}{k_0 n_3^2 \cos(\theta)}\right] \end{aligned} \tag{3.41}$$

For N=3, the dielectric function of the modulated structure is sinusoidal and given by,

$$\varepsilon(x) = \varepsilon_0 + \varepsilon_1 \exp(igx) + \varepsilon_{-1} \exp(-igx) \tag{3.41}$$

where $\varepsilon_1 = \varepsilon_{-1}$ [Fig. 3.15]. Figure 3.16-17 shows the reflectivity structure for different incident angle. For an incidence angle of 0, there is one plasmon mode. As the angle changes this plasmon mode splits into 2 modes. The refractive index of region 3 in Fig. 3.17 is considered as same as that of silver. Sharper peaks are obtained when silver is used for the third layer as expected [See Chapter 5.1].

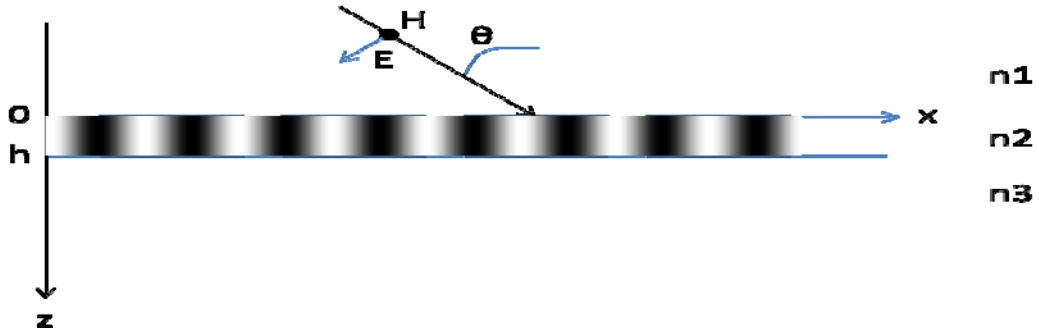

Figure 3.15 Illustration of dielectric function in the second region when first three components of fourier coefficient of dielectric function are used. Dielectric function is used in the second region. The structure is assumed infinite in the y plane.

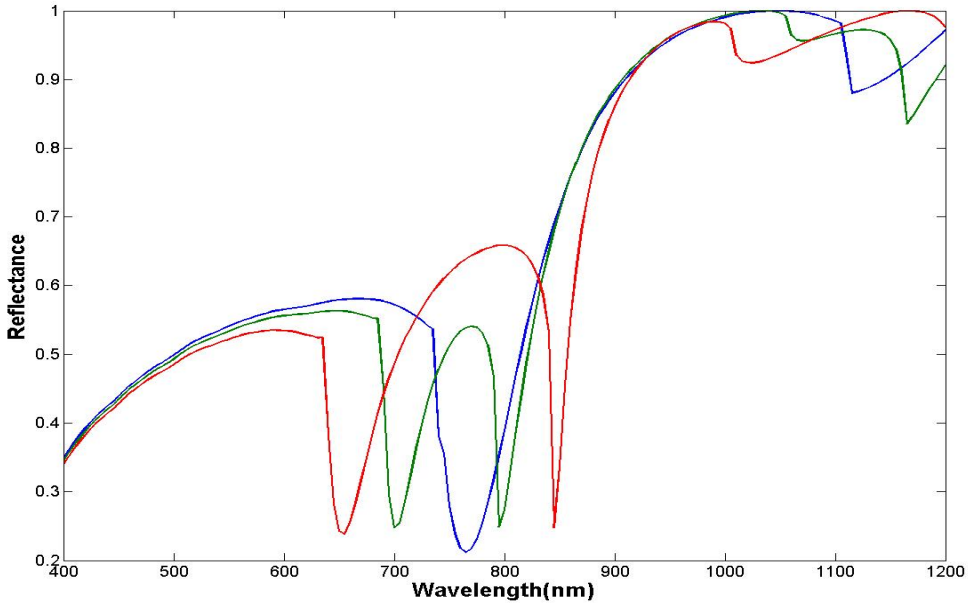

Figure 3.16 Reflectivity vs. wavelength when the first 3 components of fourier coefficients are used. . n_1=1, n_3=2.28, θ=0,4 and 8 degrees. period =740nm

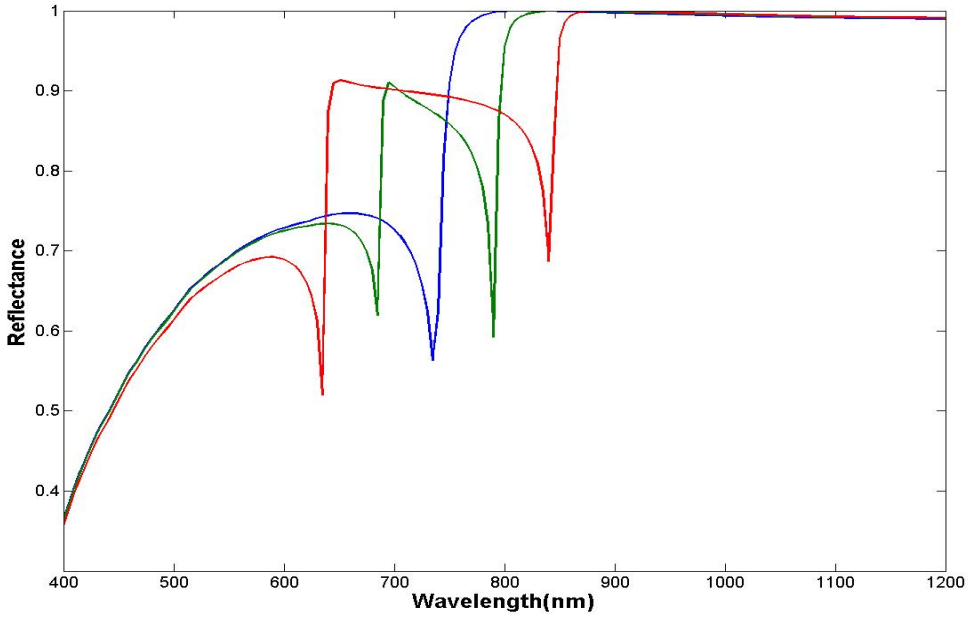

Figure 3.16 Reflectivity vs. wavelength when the first 3 components of fourier coefficients are used. . n_1=1, n_3=silver, θ=0,4 and 8 degrees. Period =740nm

Chapter 4

Simulation Emission and Absorption Enhancement on Plasmonic Structures

In this chapter, absorption and emission properties of emitters on plasmonic structures are studied. Radiative rate enhancement, quantum yield and far field patterns of classical emitters analyzed numerically. Biharmonic gratings are studied to understand the effect of band gap on emission. The absorption and emission properties of emitters coupled to proposed metallic nanoantenna strips are presented.

4.1 Simulation method

The emission of an optical emitter changes as the photonic mode density of surrounding medium modified. Near a reflector the far field emission depends on interference of direct and reflected wave. As the orientation, distance to mirror and wavelength changes the interference effect may destructive or constructive. The reflected field changes the local mode density around the emitter, so the radiative decay rate and quantum yield [Fig. 4.1].

In free space, quantum yield of an optical emitter is given by,

$$\eta = \frac{\gamma_r}{\gamma_{nr} + \gamma_r} \tag{4.1}$$

where γ_r and γ_{nr} are radiative and nonradiative transition rates. From Eq. 2.28, quantum yield can be written in terms of radiated powers as,

$$\eta = \frac{P_r}{P_{nr} + P_r} \tag{4.2}$$

In inhomogenous environment, Eq. 4.2 can be written as,

$$\eta = \frac{P_r}{P_{nr} + P_r + P_{nre}} \tag{4.3}$$

where P_{nre} is nonradiative power dissipated to environment. Furthermore, Eq.4.1 can be written as,

$$\eta = \frac{\gamma_r}{\gamma_{nr} + \gamma_r + \gamma_{nre}} \tag{4.4}$$

with γ_{nre} nonradiative transition rates due to the inhomogeneous environment. Let internal quantum yield of an emitter be η_0, then quantum yield in inhomogeneous environment is written in the form[36],

$$\eta = \frac{\eta_0}{\frac{(1-\eta_0)}{F} + \frac{\eta_0}{\eta_a}} \tag{4.5}$$

In Eq. 4.5, F is the Purcell factor defined as $F = \frac{\gamma_r}{\gamma_{r0}}$. η_a is defined as, $\eta_a = \frac{\gamma_r + \gamma_{nre}}{\gamma_r}$.

The power radiated by current source can be calculated using classical electrodynamics. Total radiated power is given by[3],

$$\oint_S (E \times H) \times dS + \int_V (\mu H \ \frac{dH}{dt} + \varepsilon E \ \frac{dE}{dt}) = -\int (j \cdot E_{loc}) dV \tag{4.6}$$

The time-averaged value from the harmonic representation of Eq.4.6 can be written as,

$$\frac{1}{2}\Re\left\{\oint_S E \times H^* dS\right\} + \frac{w}{2}\Im\left\{\int_V (H \times \mu^* H^* + E \times \varepsilon^* E^*) dV\right\} = -\frac{1}{2}\Re\left\{\int j \cdot E_{loc} dV\right\} \tag{4.7}$$

The first term of left hand side of Eq.4.7 is time averaged power transmitted to far field. The second term is the power dissipated by the surroinding environment. The right hand ride term is the total power emitted by the source. J is the current density of source. For classical dipole it is defined as with a dipole moment at position r_0,

$$J = iwp_0\delta(r - r_o) \tag{4.8}$$

The volume integral on the right hand side of Eq. 4.7 is zero everywhere except the emitter position. The integral term then becomes,

$$-\frac{1}{2}R\left\{\int j \cdot E_{loc} dV\right\} = -\frac{w}{2}\Im\left\{p_0^* \cdot E_{loc}\right\} \tag{4.9}$$

So, the total power radiated by a classical dipole depends on the electric field intensity and the orientation of dipole. Local electric intensity can be interpreted as the density of states at the source location. For simple system, such as metallic mirrors, spherically symmetric systems or stratified mediums the far field radiation and electric field intensity can be found analytically. But, for most of the problems, there are many and disordered scatterers and solving the problem becomes more and more complex. For such problems, numerical methods are more preferred. Finite integration, finite element and finite difference time domain methods can be used to solve problem numerically. Then, the obtained results are processed to calculate emission properties.

We applied finite difference time domain (FDTD) method to plasmonic grating and nanoantenna structures. Then, obtained field distributions are used to calculate radiative rate enhancement and quantum yield of an optical emitter coupled to these structures. Not all FDTD programs have, defined dipole sources. We used Lumerical's FDTD program which have magnetic and electric dipole sources [28]. The emission is modeled as classical dipole.

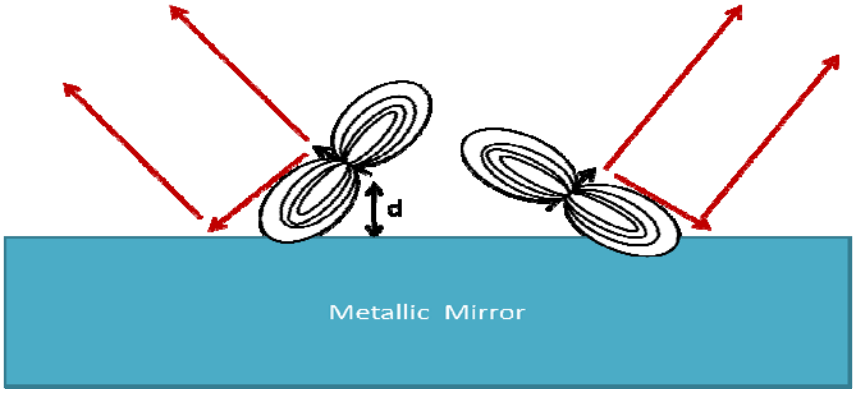

Figure 4.1 Emitter on a metallic mirror. The local field intensity or mode density around the emitter and far field radiation depend on the position, polarization and the surrounding medium. Emitter is modeled as classical dipole. Field intensity can be destructive or constructive at the dipole position and at the farfield as the distance to surface changes.

4.2 Emission on sinusoidal gratings

Surface plasmons can be excited on gratings with nanometer periodicity. Field intensity can be enhanced on the order of 100 close to the surface due to the small volume of surface plasmons. Therefore, both absorption and emission of an emitter close to interface can be altered. Emission changes due to the scattering of dipole emission by the surrounding environment. Local mode density at the dipole position determines emission process. Coupling of emitted light to surface plasmons can modify mode density around the emitter.

In our experiments, we used modified DVD-R discs used to fabricate grating structures to excite surface plasmons. The surface profile varies for different brands. We used Philips' DVD-R discs, which have almost sinusoidal surface profile. They have 740nm periodicity and 0.5 duty cycle.

We simulated radiative rate enhancement and quantum yield of dipoles on sinusoidal gratings for different lateral and vertical position for perpendicular and parallel polarizations. The simulation parameters are optimized to obtain most stable results. We used 30x4 μm^2 simulation domain with 5nm mesh size. The emitter is located at the center of the domain. We used first term of left hand side of Eq.4.7 to calculate far field radiation. As the lateral dimension of problem gets smaller, the oscillatory behavior of far field radiation is observed due to surface plasmons. So that, we chose 30 µm lateral size to minimize the field intensity of surface plasmons at far field. For

the simulations, emitters have 0.2 intrinsic quantum yield, surrounding medium is air and the depths of gratings are 60nm.

In Figs 4.2-3 radiative rate enhancement and quantum yield for parallel and perpendicular oriented dipole vary regarding the distance to the metal dielectric interface. As the distance increases, the oscillations increases due to the interference effect of emitted and reflected waves. The peaks of perpendicular dipoles come from the increased plasmonic mode density around 760nm. Fig 4.4 shows the dispersion relation of surface plasmons. At 760nm the dispersion curves of different orders intersect and the both curves contribute to mode density. In Figs. 4.5-6, the distance dependent radiative rate enhancement and quantum yield shows that as the wavelength increases for a specific distance, the oscillation period decreases. Since, in the emission process interference occurs due to the contribution of wavevector, which is related to the wavelength inversely. Also, as the distance to the interface decreases, the emission is almost quenched for parallel oriented dipoles. This can be understood by means of method of images[Fig.4.7]. As the dipole interface separation decreases, the image of the dipole cancels the effect of dipole for parallel polarized dipole. For perpendicular polarized dipole, the image tends to strengthen the dipole.

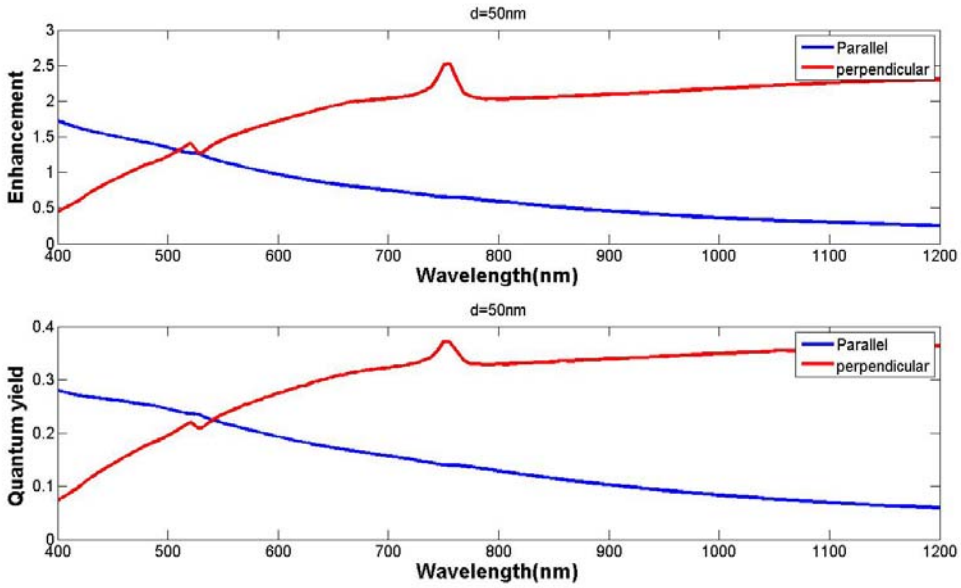

Figure 4.2 Calculated wavelength dependent radiative rate enhancement and quantum yield for both polarizations of dipole on sinusoidal gratings using the method described above. At 760nm, due to enhanced mode density, emission enhancement is more significant[See Fig. 4.4]The distance of dipole to the surface (d) is 50nm, n_0=0.2

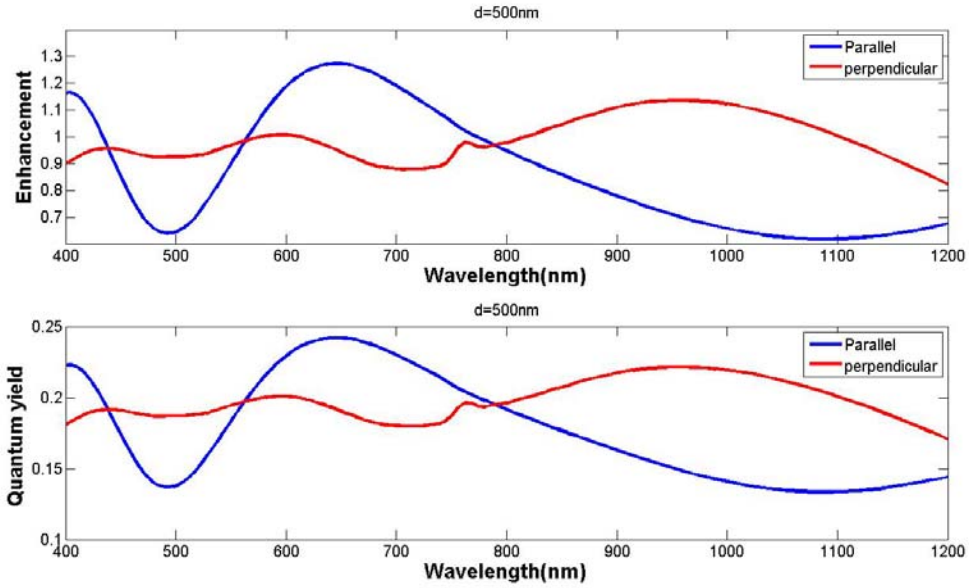

Figure 4.3 Calculated wavelength dependent radiative rate enhancement and quantum yield for both polarizations of dipole on sinusoidal gratings. The effect of plasmonic mode density is still significant at 760nm. d=500nm,n_0=0.2

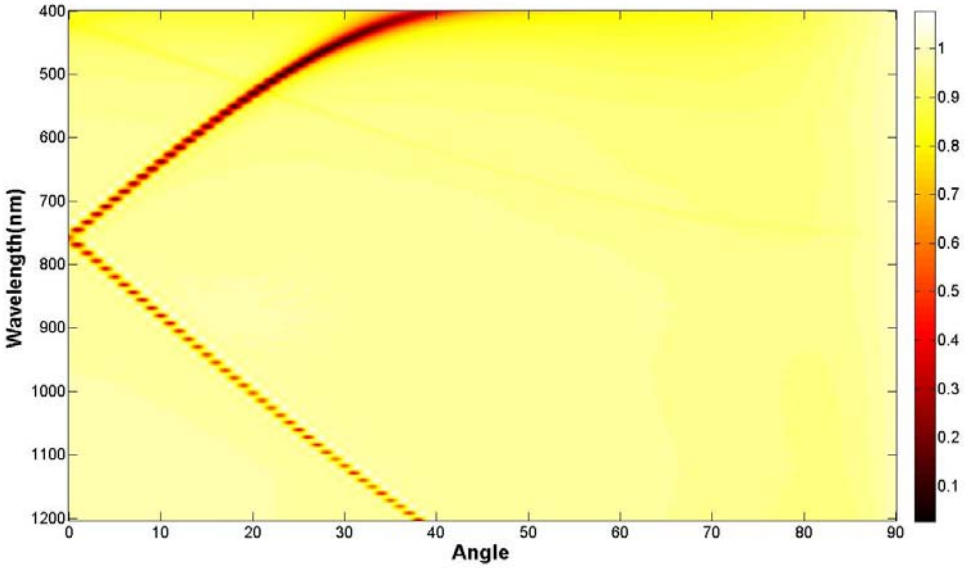

Figure 4.4 Numerical dispersion curve of surface plasmons on sinusoidal gratings. Two parts of dispersion curve intersect at 760nm. Plasmonic mode density can be defined as $(d\omega/dk_n)^{-1}$ for the curve n. At 760nm two curves intersect and total plasmonic mode density is the sum of each curve's plasmonic mode density. Dispersion curves are calculated using RCWA

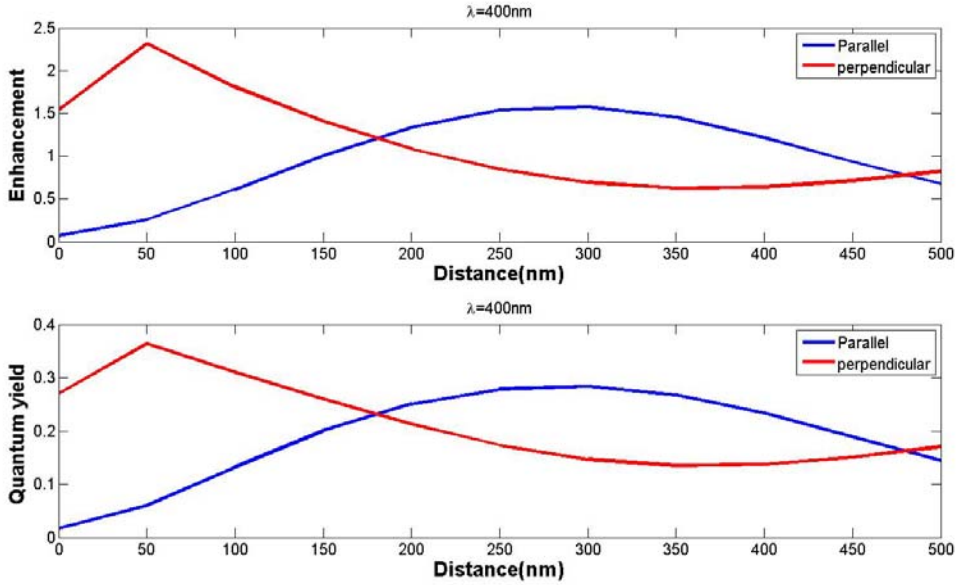

Figure 4.5 Calculated distance dependent radiative rate enhancement and quantum yield for both polarizations of dipole on sinusoidal gratings. Wavelength of the emitter is 400nm. The emission of parallel polarized dipole quenches as the distance decreases [See Fig. 4.7], $n_0=0.2$

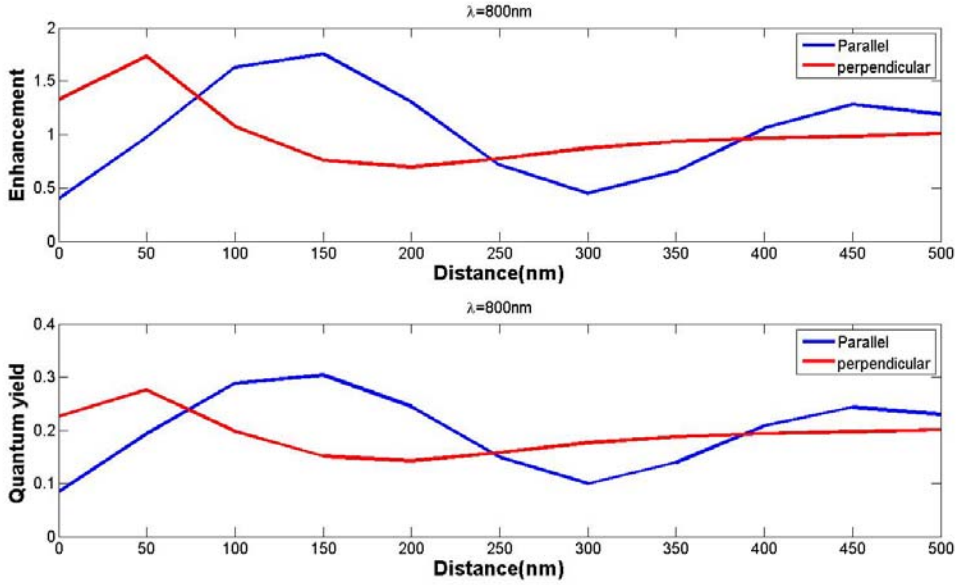

Figure 4.6 Calculated distance dependent radiative rate enhancement and quantum yield for both polarizations of dipole on sinusoidal gratings. Wavelength of the emitter is 800nm. Oscillations are due to decreased wavevector. The emission of parallel dipole quenches as the distance decreases [See Fig. 4.7], $n_0=0.2$

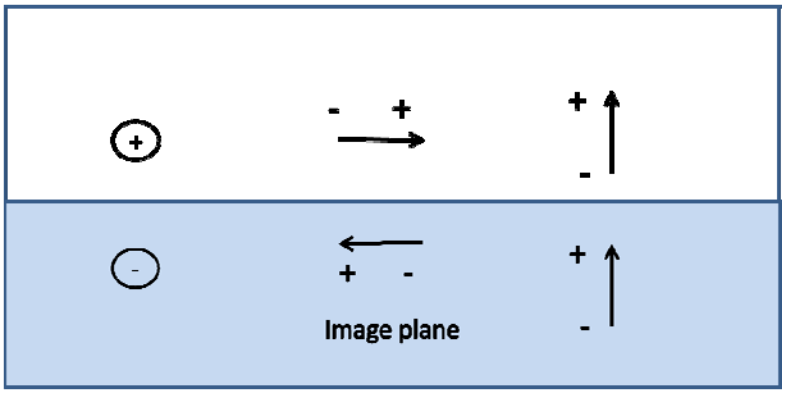

Figure 4.7 Image formation of positive charge, parallel and perpendicular polarized dipoles on a metallic mirror. Images are formed inside the mirror. As the dipole mirror separation decreases, the image of dipole cancels the effect of dipole for parallel polarization, the image of dipole strengthens the effect of dipole for perpendicular polarization

Lateral position of the emitter also effects the emission properties. Because, plasmonic mode density is not uniform on the surface. We examined where the peak on radiative rate enhancement and quantum yield comes at 760 nm for perpendicular dipole[Fig.4.2]. Firstly, we have to understand how the x and y components of Electric field intensity are localized on the interface for 760nm wavelength. In Fig.4.8, x and y component of electric field intensity is shown. The positions where radiative rate enhancement of dipole are calculated is shown in Fig.4.9. The field distributions of y component are the highest at the sides of the ridges of the gratings for 760nm wavelength. So, we expect that radiative rate enhancement and quantum yield are the highest at this point.

Fig. 4.10 shows the calculated radiative rate enhancement and quantum yield for all positions. As expected, we get higher rate enhancement and quantum yield the first dipole position at this wavelength. Although y component of electric field intensity diminishes at the ridges, we have emission enhancement. At the third position of dipole, emission is quenched.

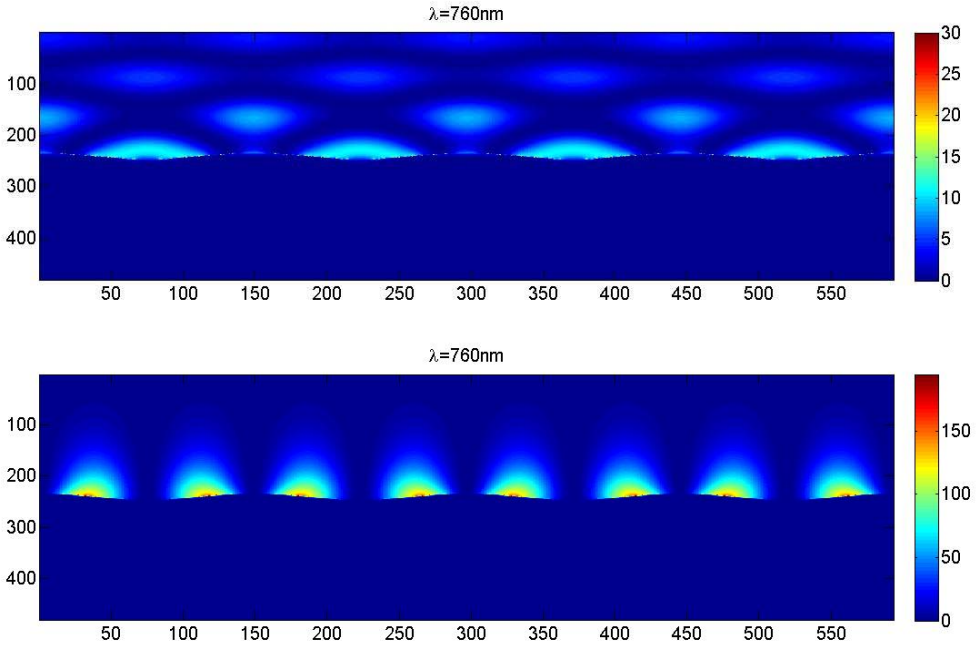

Figure 4.8 x and y components of electric field intensity at 760nm.. Perpendicular polarized dipoles are placed on the positions that y component of electric field is enhanced [See Fig. 4.8]

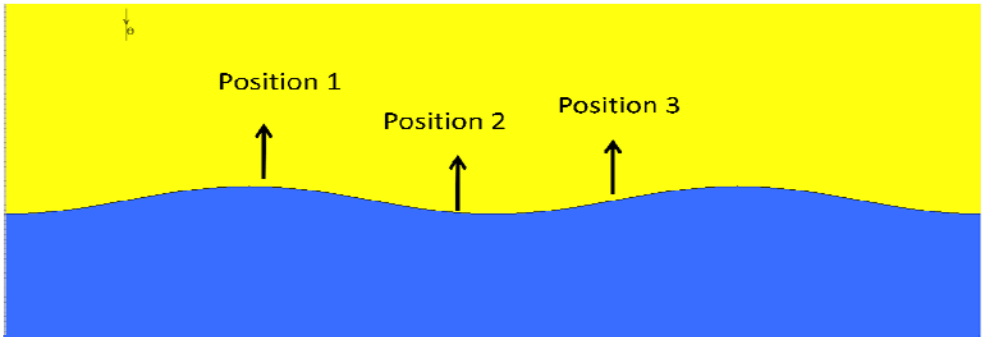

Figure 4.10 Dipole positions are to examine the effect of electric field distributions(Distribution of plasmonic mode density) for parallel polarization.

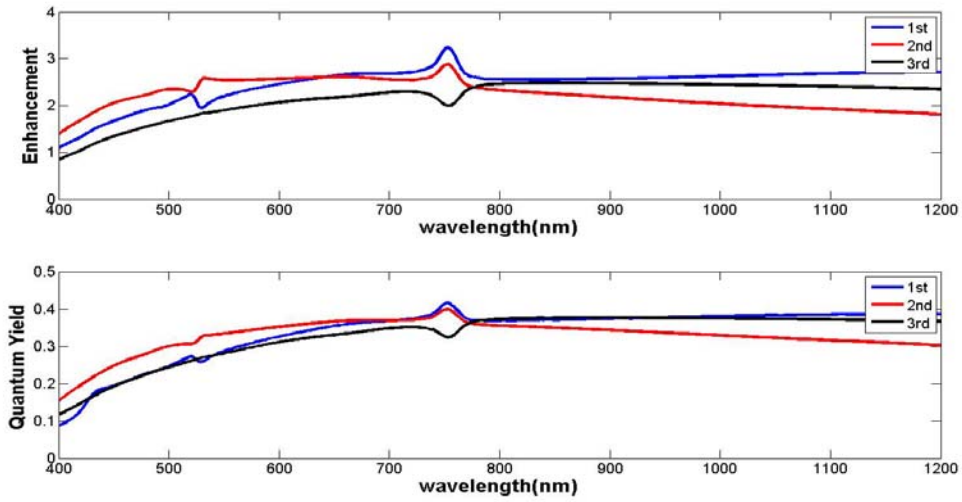

Figure 4.11 Calculated wavelength dependent radiative rate enhancement and quantum yield for perpendicular dipoles on sinusoidal gratings. At the ridges and grooves, the effect of plasmonic mode density at 760 is more significant. At the edges(middle points between grooves and ridges), emission is quenched slightly around 760nm. n_0=0.2, d=50nm

4.3 Emission on Biharmonic gratings

In standard sinusoidal gratings, there is only one harmonic component of surface profile. So that, no bandgap formation occurs. Another harmonic, causes the split of band and forming the bandgap. Near bandgap, the mode density of plasmons and emission are enhanced. At the bandgap, emission is quenched due to the lack of available states.

We used DVD-R disc for the excitation of SPPs. They have grating structures on it with a periodicity 740nm. Surface profile is almost sinusoidal for most of the discs. However, some discs have biharmonic grating structures on it. So that, we studied the formation of bandgap and emission enhancement using biharmonic gratings(Fig.4.12).

Fig. 4.13 is the calculated dispersion relation SPPs. The curves are splitted from 740 nm and bandgap formed between 740nm and 810nm. We expect an emission enhancement around bandgap and quenching of the emission at bandgap. However, we have mentioned the electric field intensities are localized some locations for both polarizations. Therefore, we examined the x and y components of electric field intensities for 740 and 810nm.

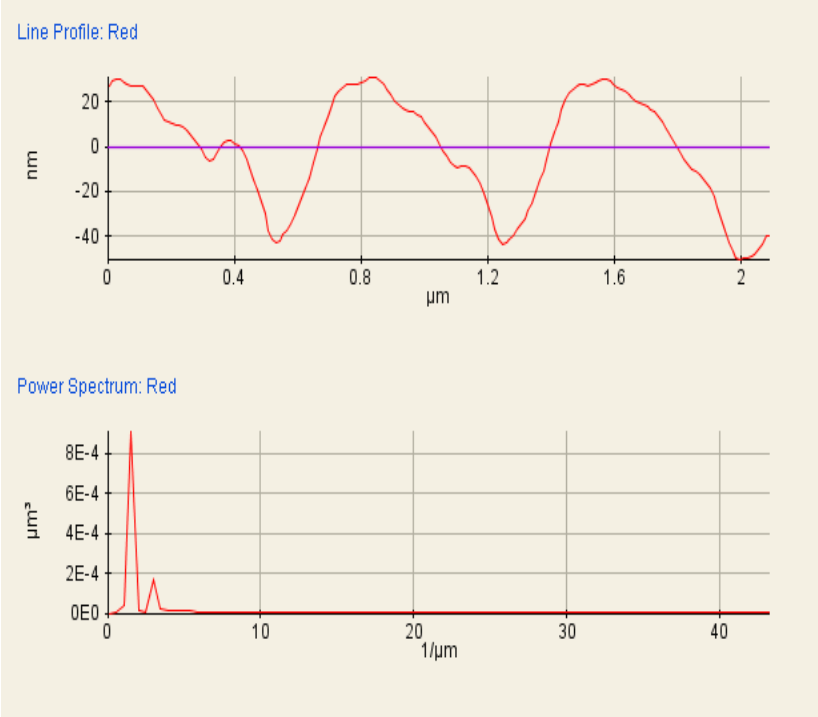

Figure 4.12 AFM surface profile and power spectra of biharmonic DVD-R gratings. Two peaks in Power Spectrum indicate the biharmonic surface profile.

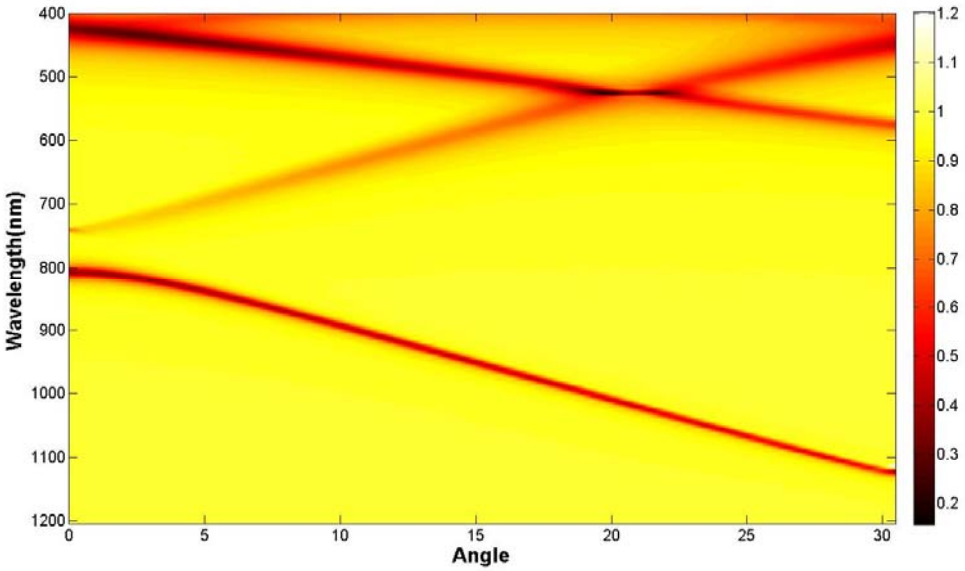

Figure 4.13 Numerical dispersion curve of Surface plasmons dispersion on Biharmonic grating with period 740nm calculated using RCWA. The second harmonic imposed as a second grating with period 370nm. The ratio of amplitudes of harmonics is 0.65. Bandgap formed between 740nm and 810nm

Figs 4.14-15 show the x and y components of electric field intensities for 740nm and 810nm. We analyzed the emission properties of dipoles placed where x and y components of electric field intensity is enhanced. For parallel polarized dipoles, we chose the points where x component of electric field intensity is enhanced. For perpendicular polarized dipoles, we chose the points where y component electric field intensity is enhanced [Eq. 4.9]. We chose 2 points for 740nm and 2 points for 810nm for each polarization of dipoles. In Figs. 4.16-17, radiative rate enhancement and quantum yield are for different positions of dipoles for both polarizations are shown. For parallel polarization, emission properties are enhanced for all positions at the edges of bandgap. Since, x component is localized at the edges of ridges for both wavelength. For 810nm, enhancement is more significant due to more intense field distribution. Also, emission properties decreases significantly at the bandgap as expected. For perpendicular polarization, the significance of position is more apparent. The effect of localization of y component of electric field intensity at 810nm is more than 740nm. Since, confinement effect for 810nm is stronger. In Fig. 4.18, positions of dipoles are shown where emission properties are calculated.

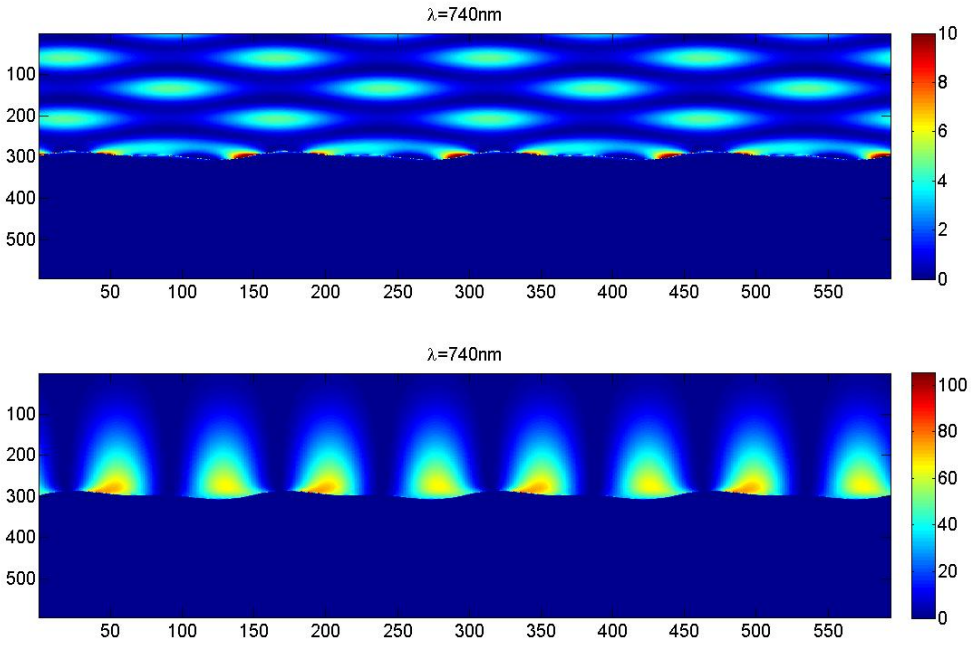

Figure 4.14 x and y components of electric field intensity at 740nm. Perpendicular polarized dipoles are placed on the positions that y component of electric field is enhanced. Parallel polarized dipoles are placed on the positions that x component of electric field is enhanced [See Fig. 4.18]

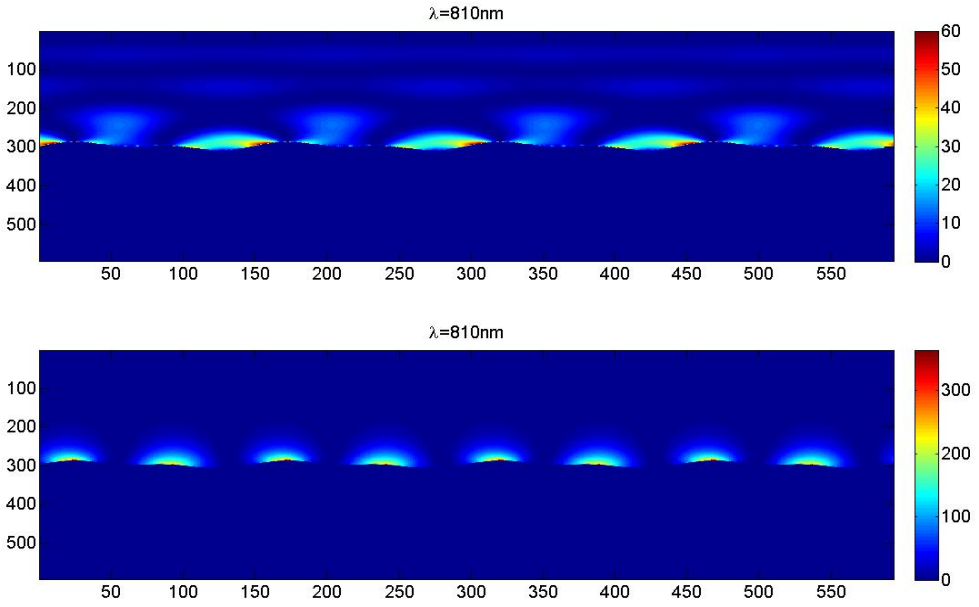

Figure 4.15 x and y components of electric field intensity at 810nm. Perpendicular polarized dipoles are placed on the positions that y component of electric field is enhanced. Parallel polarized dipoles are placed on the positions that x component of electric field is enhanced [See Fig. 4.18]

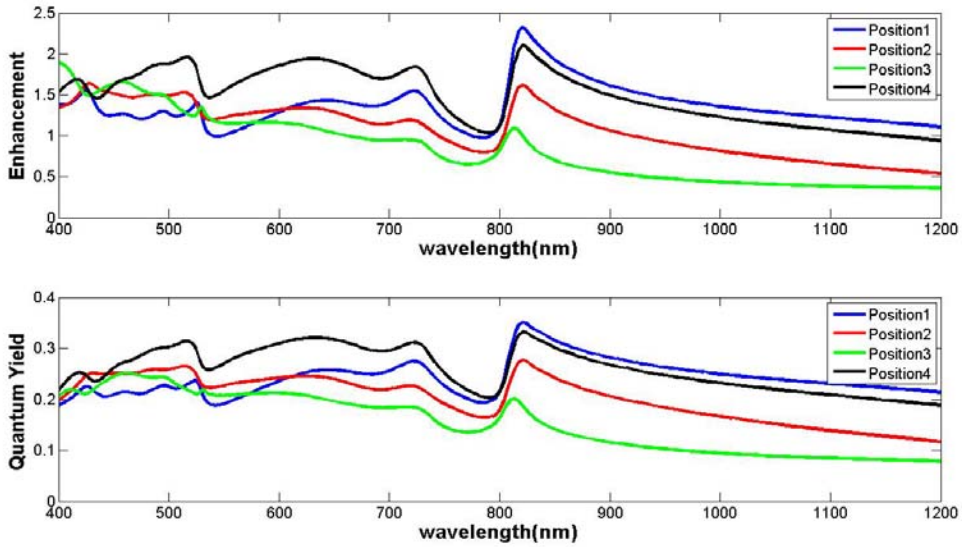

Fig.4.16 Calculated wavelength dependent radiative rate enhancement and quantum yield for parallel dipoles on sinusoidal gratings. Emission is enhanced at edges of bandgap(740nm and 810nm). At the bandgap, emission is quenched significantly. For the positions of dipole[See 4.18]. n_0=0.2

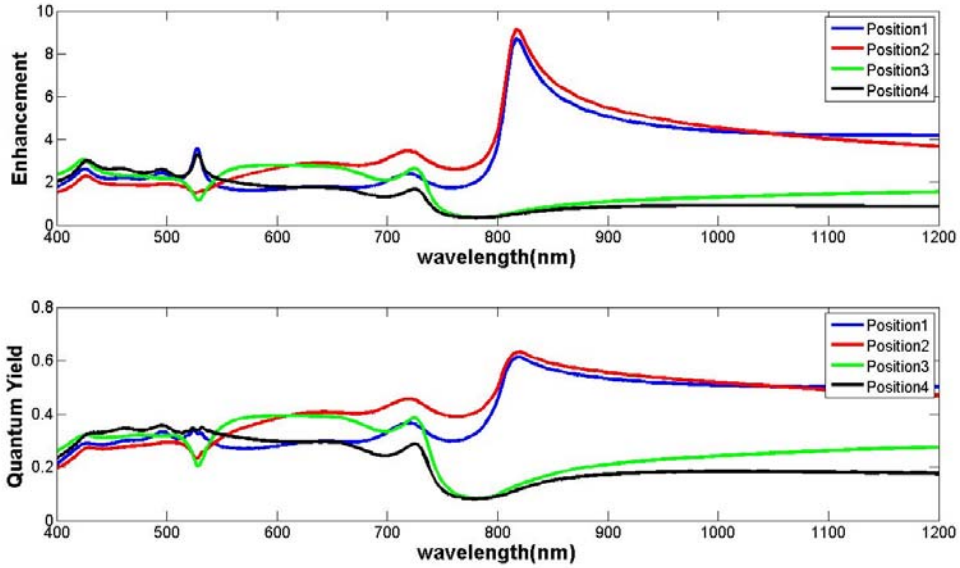

Fig.4.17 Calculated wavelength dependent radiative rate enhancement and quantum yield for perpendicular dipoles on sinusoidal gratings. Emission is enhanced or quenched for different positions. Emission enhancement for the positions 1 and 2 at 810nm is due to the enhanced mode density at these points. For positions 3 and 4, emission is quenched at 810nm due to reduced mode density at these points [See Fig. 4.18]. At the bandgap, emission is quenched significantly. For the positions of dipole [See 4.18]. n_0=0.2

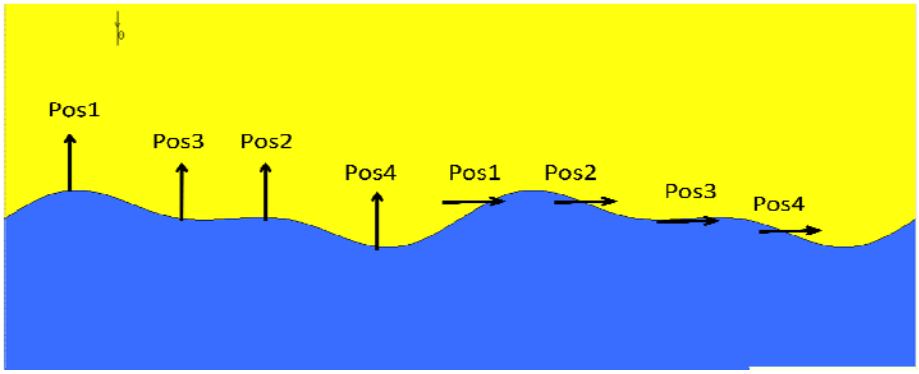

Fig.4.18 Dipole positions are to examine the effect of electric field distributions (Distribution of plasmonic mode density) for parallel and perpendicular polarizations.

4.4 Absorption enhancement on gratings

Due to excitation of plasmons at the metal air interface, field intensity enormously increases. Absorption of light by a fluorophore increases as the excitation intensity increases[Eq. 2.29]. Surface plasmons can be used to enhance absorption of emitter rather than the increasing the excitation intensity. However, surface plasmons are tightly confined to the interface. Only, absorption of fluorophores close to the interface can be enhanced. In grating structures, incident light couples to surface plasmons at particular angles. Fig. 4.19 shows the resonance condition for sinusoidal gratings with 740nm periodicity for incidence wavelength 532nm and TM polarization. Silver is used as metallic layer. The depth of grating is 60nm. At 20 degrees, surface plasmons are excited. Fig. 4.20 illustrates x and y component of electric field intensity. In Fig. 4.21 field intensities regarding the distance from the interface for different lateral position of grating. At the boundary, enhancement factor for the x, y component of electric field intensity are 25 and 80. Therefore, absorption of fluorophores can be enhanced upto 80 fold depending of the polarization and position on the gratings [Fig.4.22].

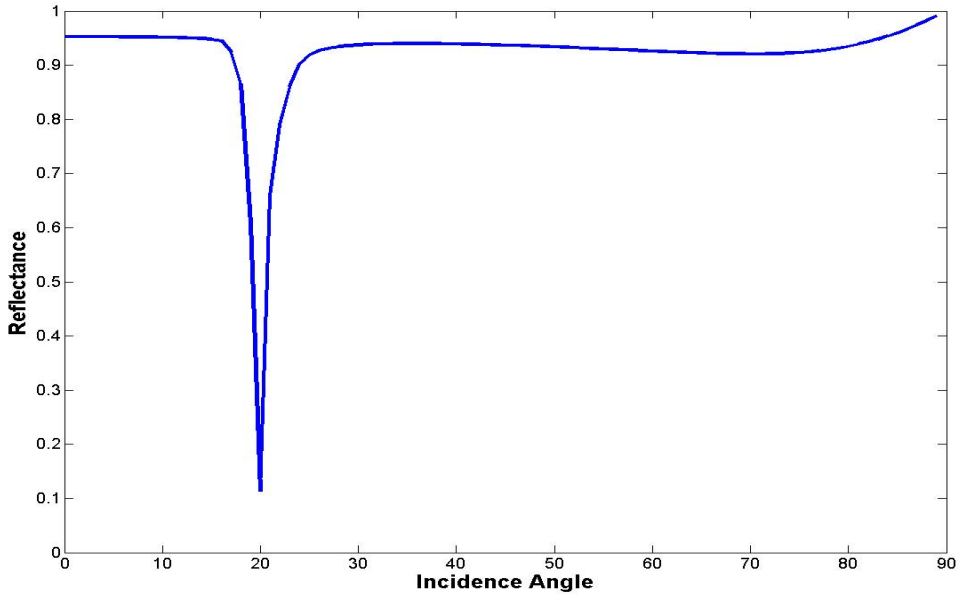

Figure 4.19 Reflectivity vs. angle for sinusoidal gratings, λ=532nm, Period=740nm, metal=silver

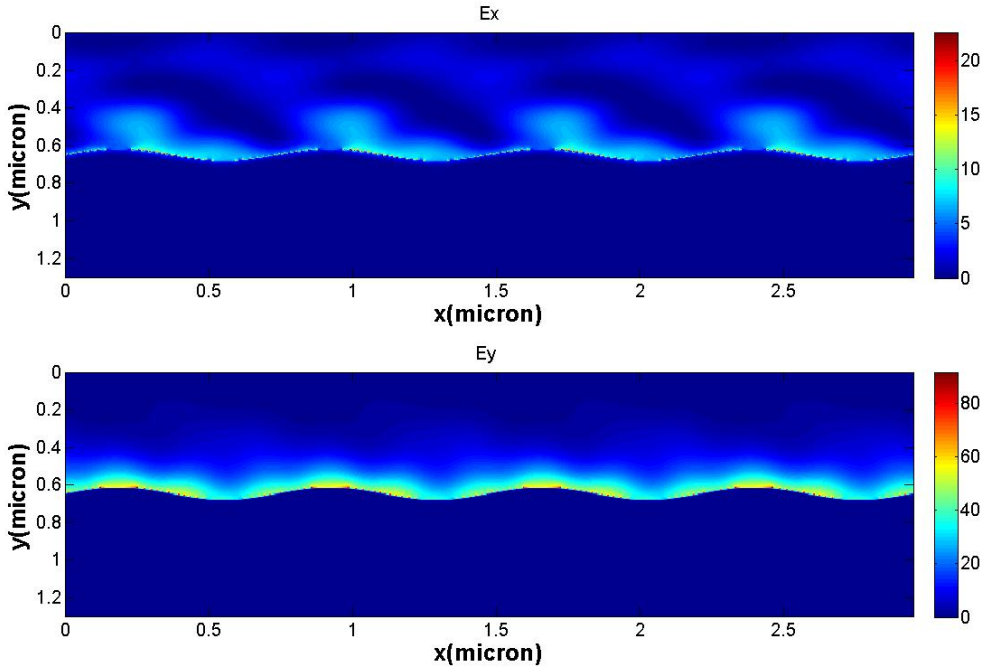

Figure 4.20 x and y component of electric field intensity. λ=532nm, θ=20

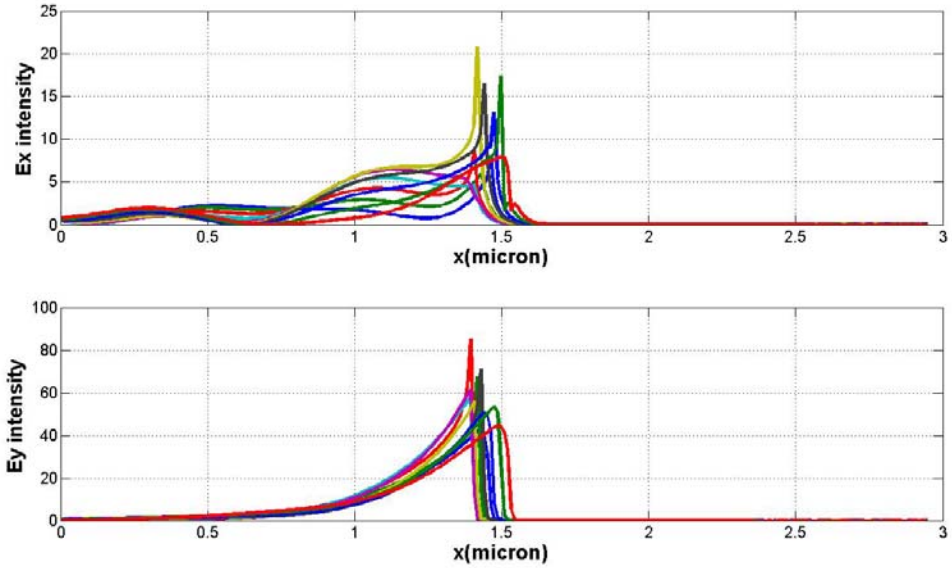

Figure 4.21 Field intensities at different lateral positions on grating. This figure also explains the how much absorption is enhanced for fluorophores that are close to the interface. λ=532nm, θ=20

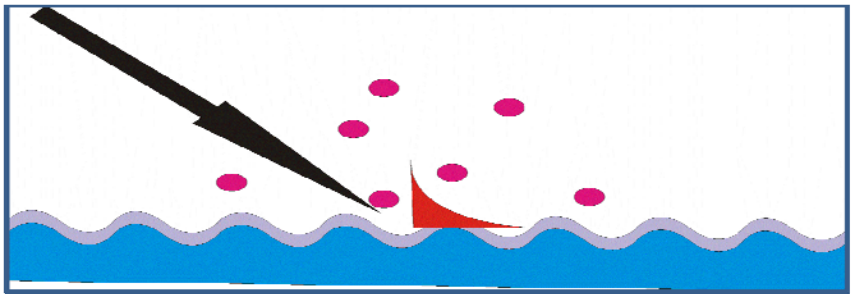

Figure 4.22 Position of fluorophores with respect to tail of SPPs. At the excitation wavelength surface plasmons are excited. Due to enhanced field distribution at excitation wavelength, absorption of fluorophores are enhanced

4.5 Emission on plasmonic nanoantenna strips

The optical properties of metallic nanostructures depend on their size, shape and environment. When the wavelength of incident light is comparable to the dimensions of particle, localized surface plasmons are excited. The enhanced field intensity increases the absorption rate of fluorophores close to the particle. The emission properties changes due to the mode density of plasmons at emission wavelength.

When two particles get closer to each other, the field intensity can enhanced tremendously. Nanoparticle dimer antennas and their arrays, nanoresonator antennas and bowtie nanoantennas with different materials are well studied examples of plasmonic nanoantennas[36-38]. We have studied nanoantenna strips both numerically and experimentally. In the previous study[21], electrodynamic calculations of spontaneous emission coupled nanoantenna strips are studied both numerically and theoretically. We have studied a similar geometry which we fabricated using e-beam lithography. In our experimental setup, we used 532nm laser. Hence, we optimized the parameters of structures according to this excitation wavelength. In Fig. 4.23, the schematic of silver nanoantenna strip is shown. The lengths of strips are assumed infinite for simulations. Indium Tin Oxide (ITO) is used to prevent charging effects in e-beam lithography.

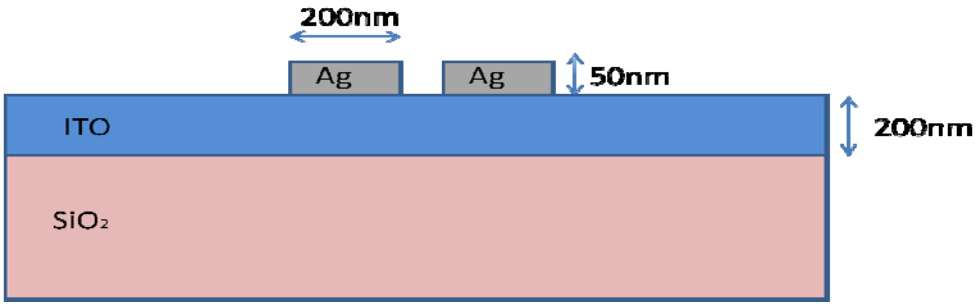

Figure 4.23 Proposed nanoantenna structure. ITO layer is used to prevent charging effect of e-beam lithography. Depending on the gap between silver wires resonance condition of nanoantenna changes.

Firstly, the scattering cross section (SCS) of nanoantenna is calculated. In grating structures, reflection and absorption curves gives us information, in which wavelength and angle surface plasmons are excited. SCS is a means for the resonance condition for the excitation of plasmons and it can be defined as the ratio of scattered power from the antenna to the incident power. The nanoantenna is illuminated with a TM polarized plane wave. Fig. 4.24 shows the SCS with different gaps. It is seen that the SCS of antennas strongly depends on the gap size. 5nm change in gap size causes to shift of resonances from 490nm to 525nm. For 35 nm, 45 nm and 55 nm gap sizes the surface plasmons are excited near 530nm. Figs. 4.25-26 shows the x component of electric field intensities for 15, 20, 35 and 40nm gap size antennas for illumination wavelength 532nm. Field intensity enhances up to 60 fold at the centers of antennas with 15nm gap size.

In Fig 4.26, intensity of x component of electric field enhances up to 15 fold at the centers of antennas with 35nm and 40nm gap sizes. Therefore, absorption of a fluorophore placed at the center can be enhanced 15 fold for excitation wavelength of 532nm.

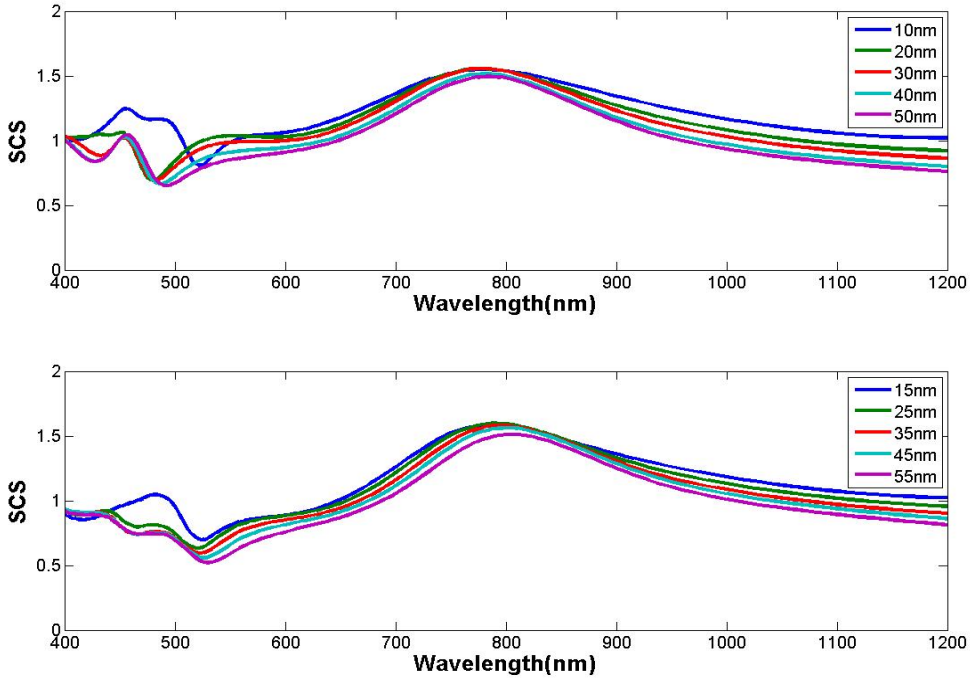

Figure 4.24 Simulated scattering cross section(SCS) of nanoantenna with different gap size

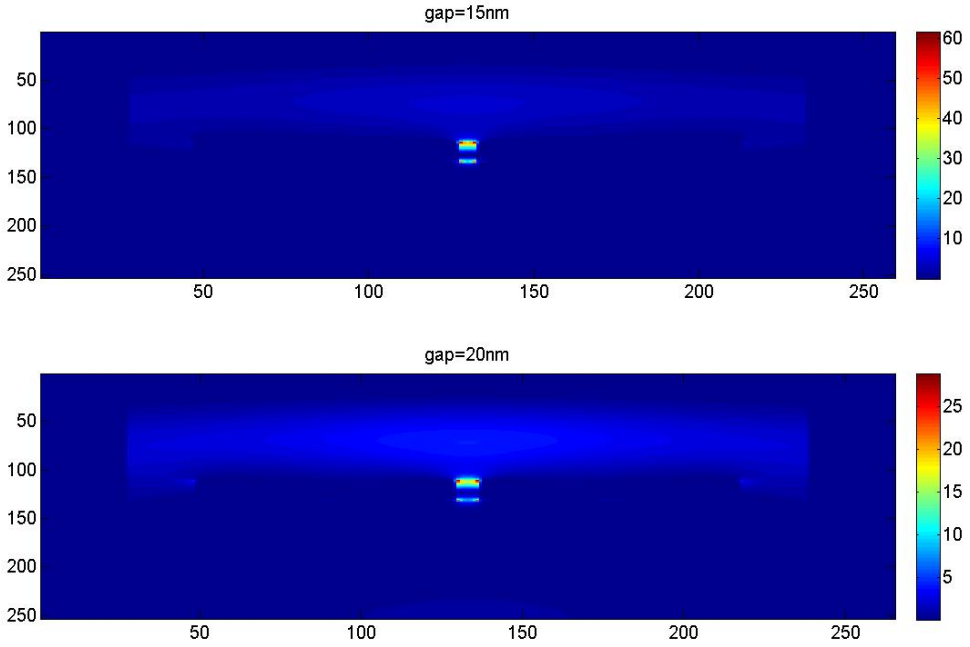

Figure 4.25 Electric field intensities for 15nm and 20nm gap sizes

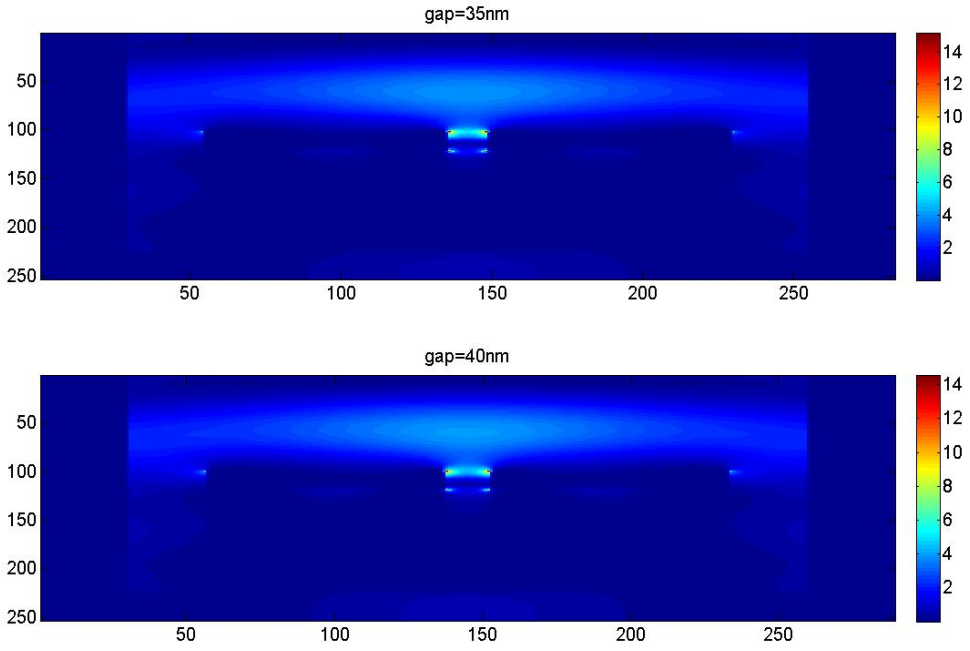

Figure 4.26 Electric field intensities for 40nm and 45nm gap sizes

In Figs. 4.27, radiative decay rate enhancement and quantum yield of a parallel dipole placed at the center of antenna with intrinsic quantum yield 0.2. As the gap size increases, radiative decay rate and quantum yield decrease for certain wavelengths. Since, the coupling between strips reduces as the gap size increases. At 510nm wavelength, the radiative rate enhancement is about 25 for 10nm gap size due to the strong coupling of emitted light to the surface plasmons, which expected from the SCS calculations. For other gap sizes, the enhancement curves shift to 470nm. Since, emitter and the antenna are not strongly coupled anymore. Also, there is radiative rate enhancement at 700nm for all antennas. In Fig.4.24, since SCS has a maximum around 800nm, enhancement and quantum yield decrease. At this wavelength plasmonic mode density around emitter decreases. As the wavelength increases, enhancement increases and quantum yield approaches 1.

In Fig.4.28, radiative decay rate and quantum yield are smaller than free space radiative decay rate and quantum yield values. Therefore, for perpendicular oriented emitters, emission is almost quenched.

Lateral and vertical positions of dipole with respect to the antenna also change the emission. In Figs. 4.29-30 radiative rate enhancement and quantum yield are

calculated as the dipole moves vertically for both polarization on 40nm gap size antenna. For parallel polarization, both parameters decrease as the vertical position of emitter increases. For perpendicular polarization, both parameter increases as the vertical position increases and the curves are well matched with SCS of antenna.

Figs. 4.31-32 show the effect of lateral position of emitter to the radiative rate enhancement and quantum yield. The vertical distance to the center of antenna is 40nm. Emission properties of parallel polarized dipole enhance more as the lateral distance to the center of nanoantenna increases.

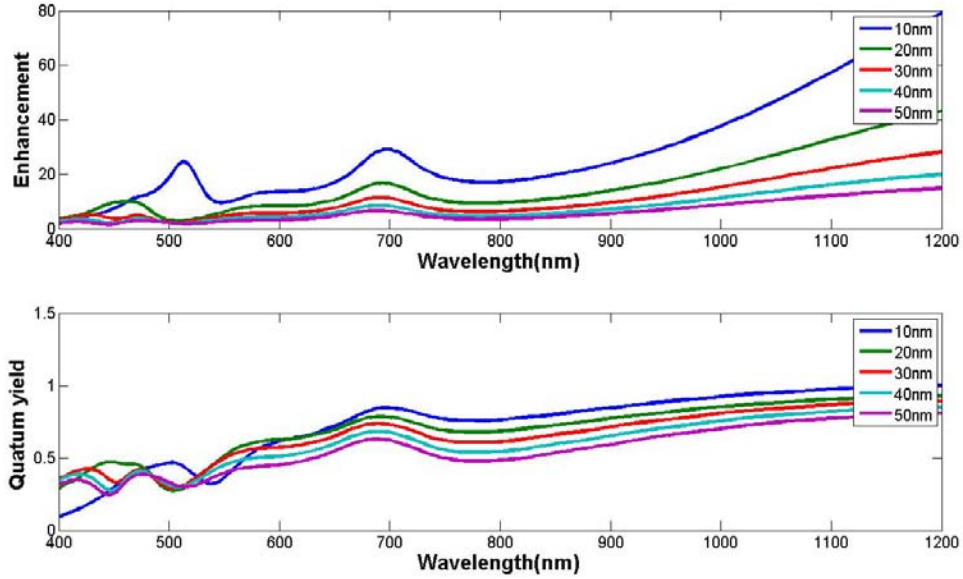

Figure 4.27 Simulated radiative rate enhancement and quantum yield for various gap size for parallel polarization. Emission is enhanced around 500nm due to enhanced plasmonic mode density. Around 800nm, quenching of emission is significant due to reduced plasmonic mode density[See SCS calculation Fig. 4.24]. The dipole is at the center of the antenna. $n_o=0.2$

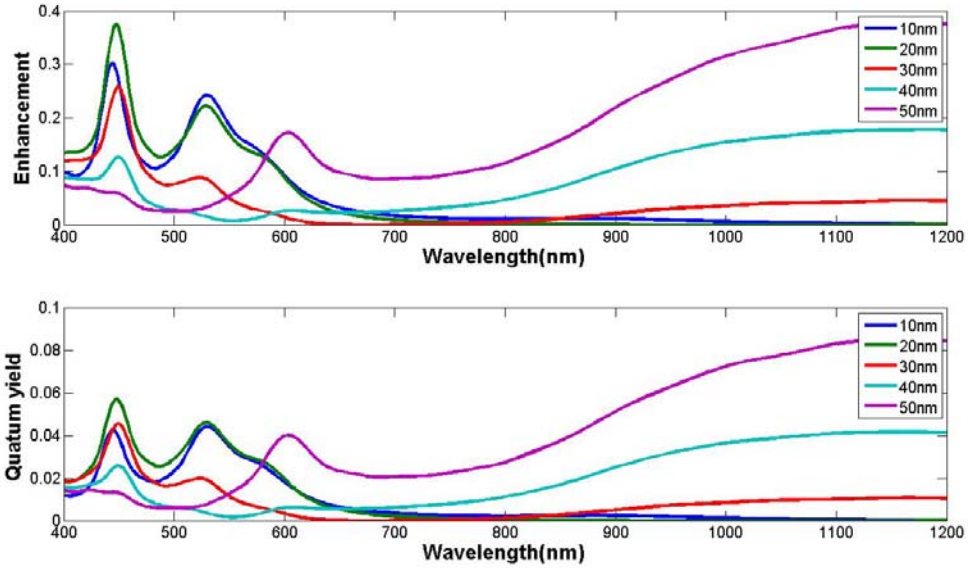

Figure 4.28 Simulated radiative rate enhancement and quantum yield for various gap size for perpendicular polarization. Emission is quenched for all wavelengths. Dipole is at the center of antenna. n_o*=0.2*

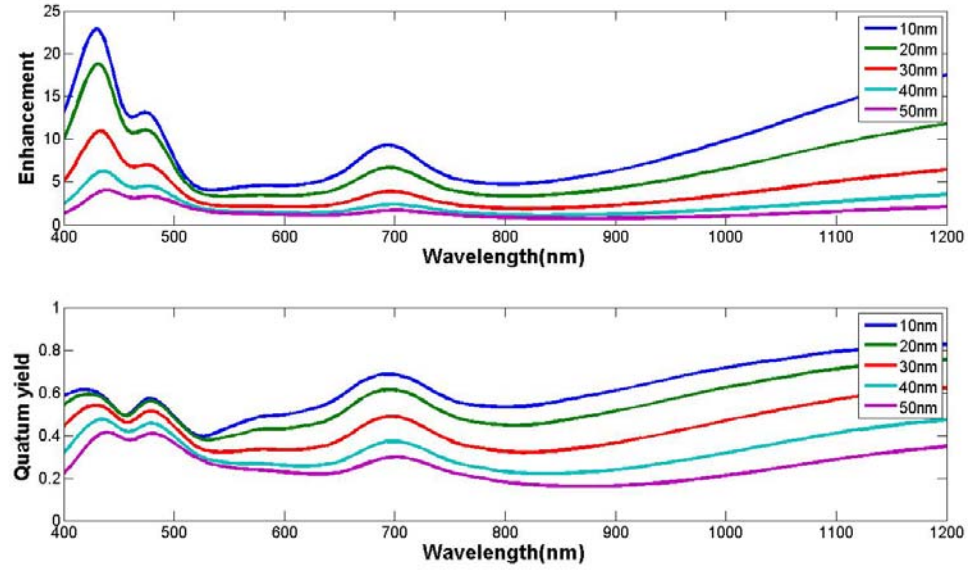

Figure 4.29 Simulated radiative rate enhancement and quantum yield for various vertical position of parallel emitter. Emission enhancement is decreased as dipoles moves vertically due to reduced plasmonic mode density. n_o*=0.2*

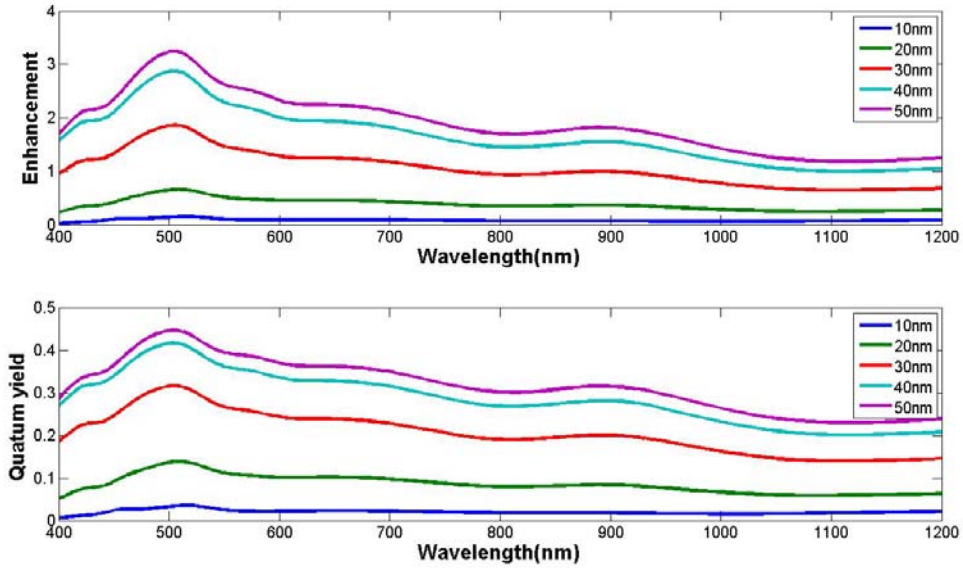

Figure 4.30 Simulated radiative rate enhancement and quantum yield for various vertical position of perpendicular emitter. Emission is enhanced as the dipole vertically. n_o=0.2

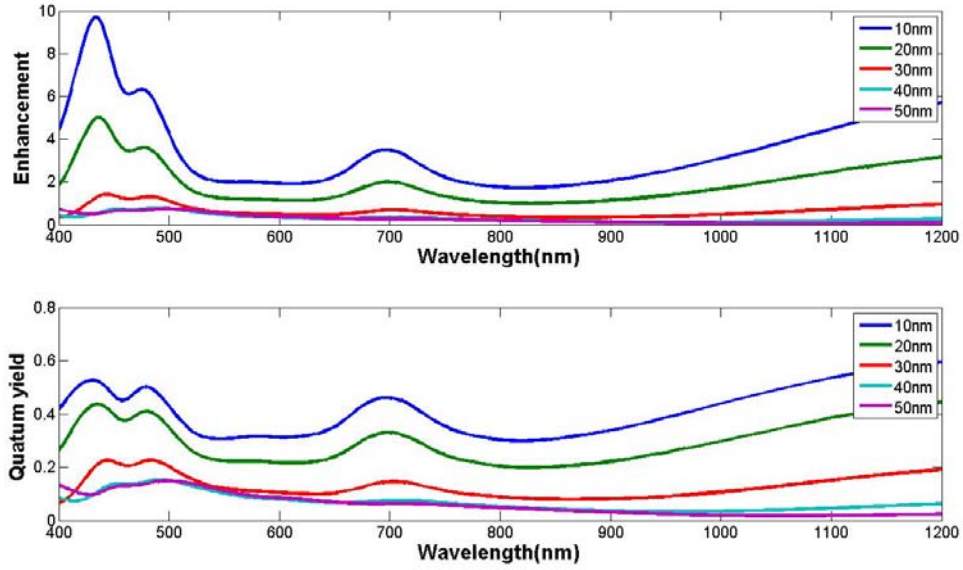

Figure 4.31 Simulated radiative rate enhancement and quantum yield for various vertical position of parallel emitter. Emission is quenched as the dipole leaves the gap of the antenna. n_o=0.2

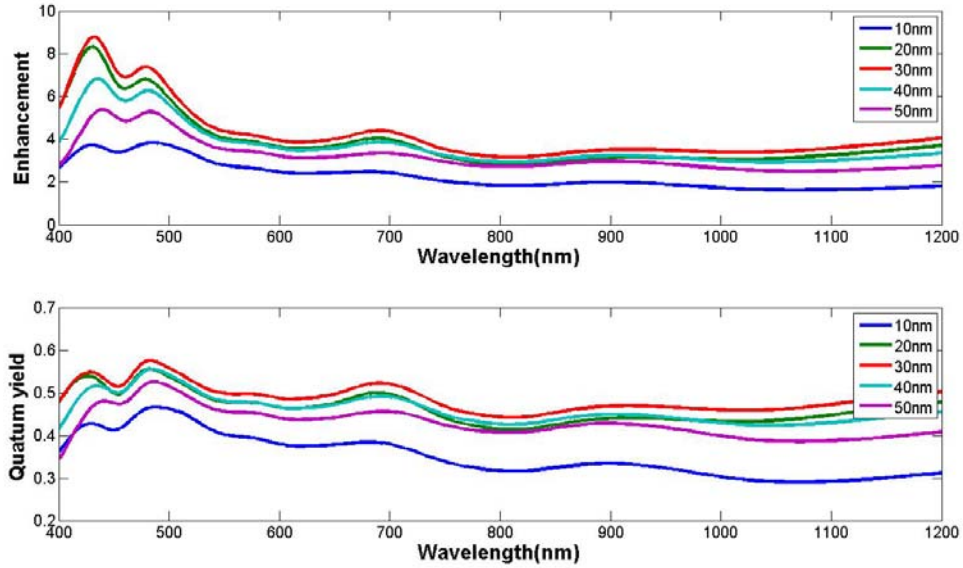

Figure 4.32 Simulated radiative rate enhancement and quantum yield for various vertical position of perpendicular emitter. Emission enhancement is significant as the dipole leaves the gap of antenna. n_o*=0.2*

Chapter 5

Experimental Work

Commercially available DVD-Rs are used to fabricate sinusoidal gratings. Nanoantenna strips and lamellar gratings are fabricated using e-beam lithography. AFM(atomic force microscopy) is used to characterize surface profile of fabricated gratings. Ellipsometer is used to obtain dispersion curves of surface plasmons. Angle resolved emission measurements are performed for absorption enhancement measurements.

5.1 Absorption Enhancement on Sinusoidal Gratings

5.1.1 Optimization, Fabrication and Characterization of Sinusoidal Gratings

Resonance condition and field distributions of gratings depends on periodicity, duty cycle, metallization parameters and groove depth. DVD-R grating structures have sinusoidal surface profile of periodicity 740nm.Due to the different fabrication processes, surface plasmon properties such as, field distributions, reflectivity and field intensities can be different. So that, structural optimization of gratings has to be done. We optimized grating structures to obtain maximum coupling conditions. Simulations are done using RCWA and FDTD. Surface profile of DVD-Rs are taken perfect sinusoidal for simulations. Duty cycle of the gratings is 0.5 for groove depth simulations. Silver is used as metallic layer. For the experiments excitation wavelength of laser is 532nm, so that all the optimization is done for 532nm.

Fig. 5.1 shows the grating coupling dispersion curves for different diffracted orders. For an excitation wavelength of 532 nm resonance conditions occurs at 17 and 24 degrees. On the other hand, for perfect sinusoidal gratings we have found that, surface plasmons are excited at 20 degrees using RCWA[Fig. 5.2]. So that, in the following simulations incidence angle assumed 20 degrees.

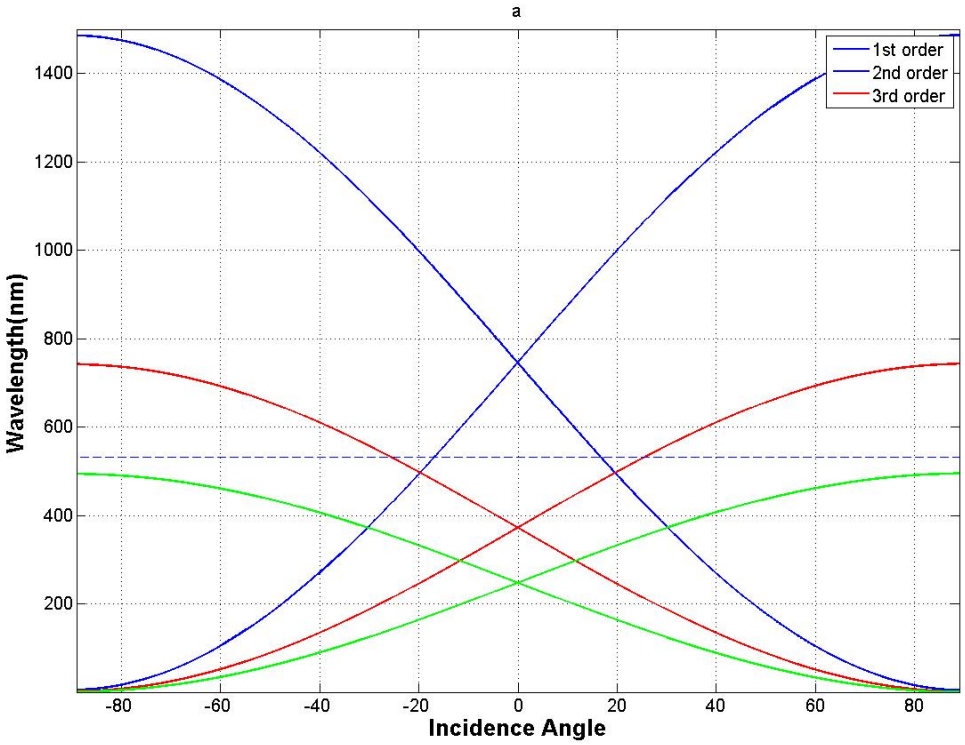

Figure 5.1 Numerical dispersion curves for plasmons on gratings

Fig.5.2 shows the effect of groove depth on the reflectivity for an excitation wavelength of 532nm. For 60 nm groove depth reflectivity minima occurs at 20 degrees and reflectivity at this angle is smaller than of 120 nm groove depth gratings. For 120 nm case resonance curve is also more wider. In Fig. 5.3, the reflectivity is plotted for various groove depths for incidence angle of 20 degrees. At 65 nm groove depth, reflectivity minima occurs. So that, 65 nm groove depth is found optimum.

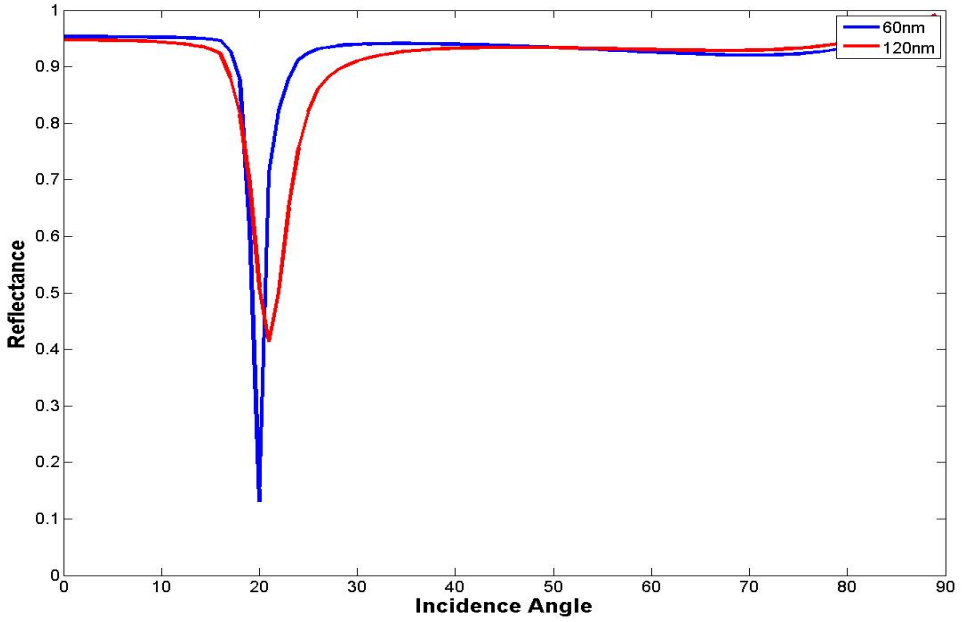

Figure 5.2 Simulated reflectivity vs. angle for 60nm and 120nm groove depths.

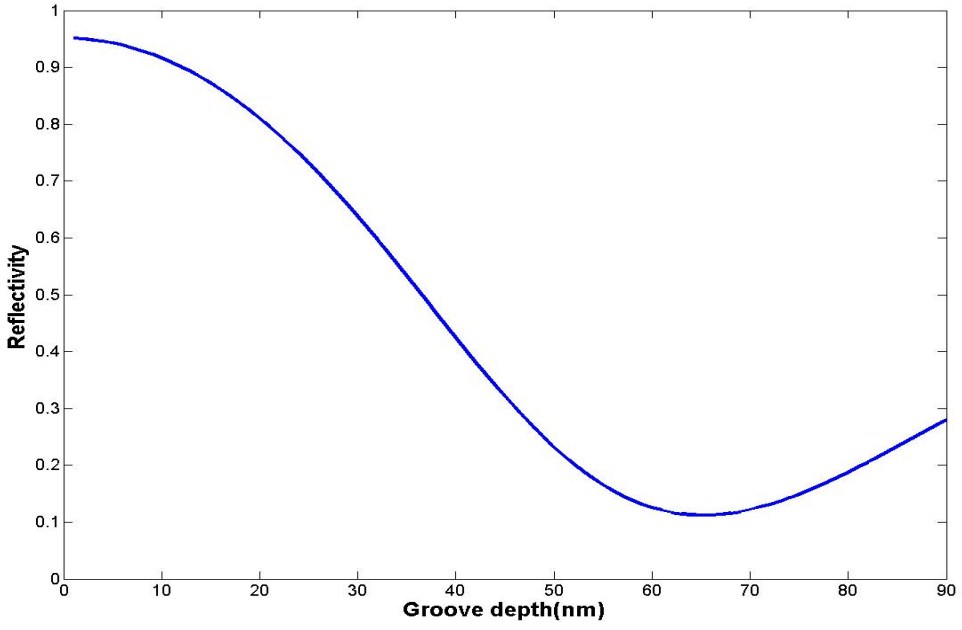

Figure 5.3 Simulated Reflectivity vs. groove depth. 65nm groove depth is found optimal for maximum coupling of surface plasmons.

Fig. 5.4 shows the reflectivity of grating for metal thicknesses of 65nm and infinite. The grating structures are assumed to be coated on Silicon Nitrate samples with a refractive index of 1.77. For infinite metal thickness the resonance curves are sharper, but the reflectivity minimum is higher. Absorption of gratings are also strongly depends on the thickness of metallic layer. In Fig. 5.5 absorption curves are plotted. For infinite metal thickness, absorption is upto 90 percent, on the other hand for 50nm metal thickness it is up to 53 percent. So that, a fraction of incident light is transmitted into the dielectric layer due to the finite thickness of metal. In Fig. 5.6 reflectivity and absorption for different metal thickness is plotted. For thicknesses greater than 100nm absorption is nearly constant. The thickness of metal can be assumed infinity after 100nm. Since, the grating depth and surface profile can be harmed, in fabrication processes it is not suitable to cover gratings with thick metal films. So that, the thickness of metal is taken between 60-70nm which is feasible for fabrication processes.

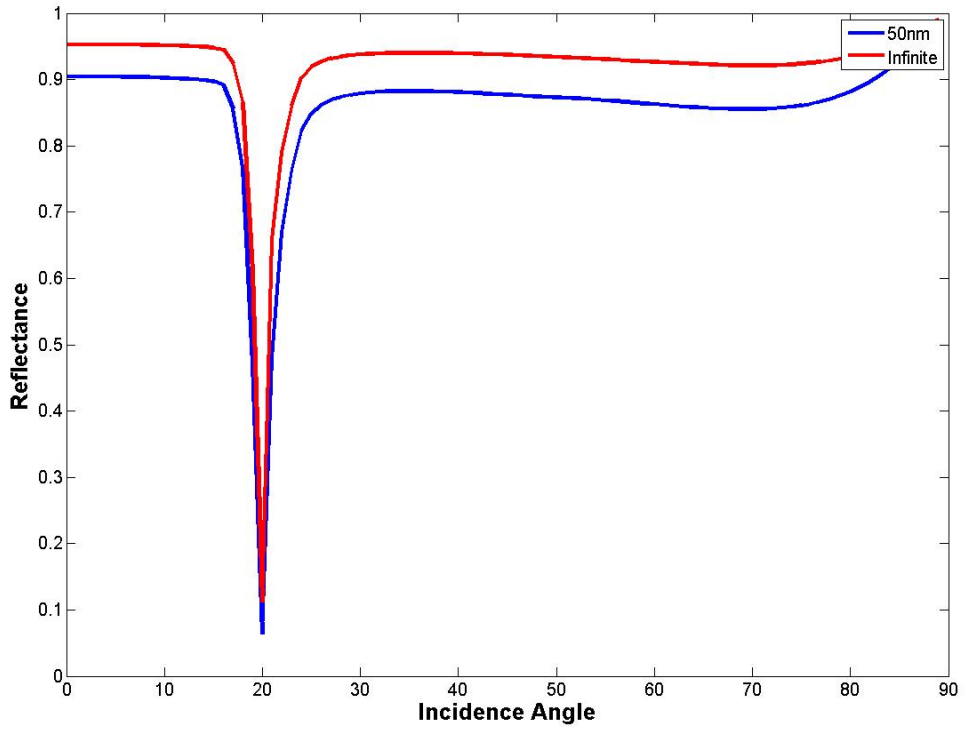

Figure 5.4 Simulated Reflectivity for different metal thicknesses. Quality factor of the resonance strongly depend on metal thickness.

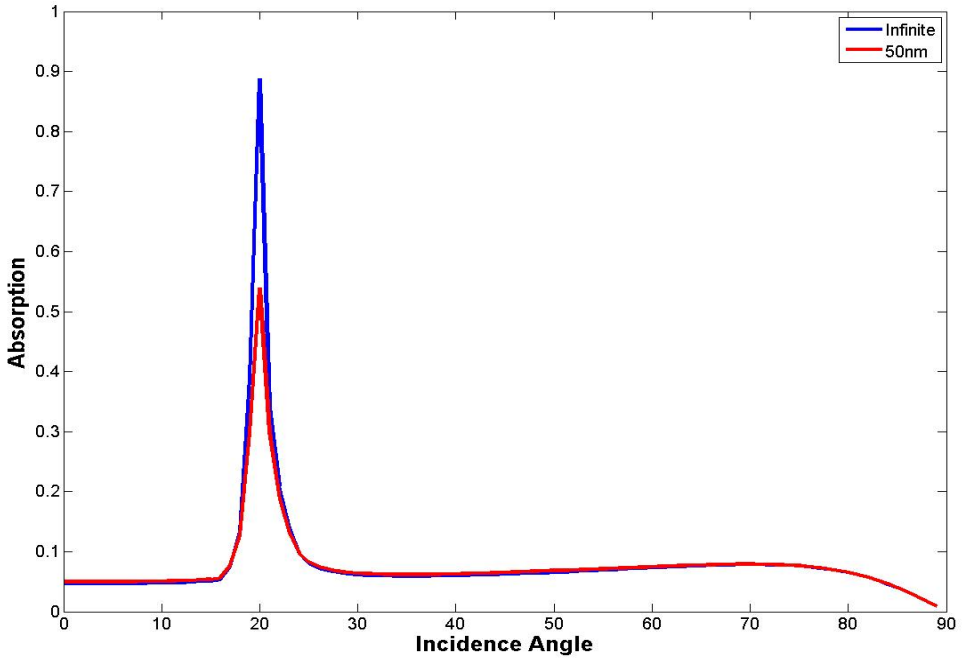

Figure 5.5 Simulated Absorption for different metal thickness. For infinite thickness metallic film, absorption is maximum.

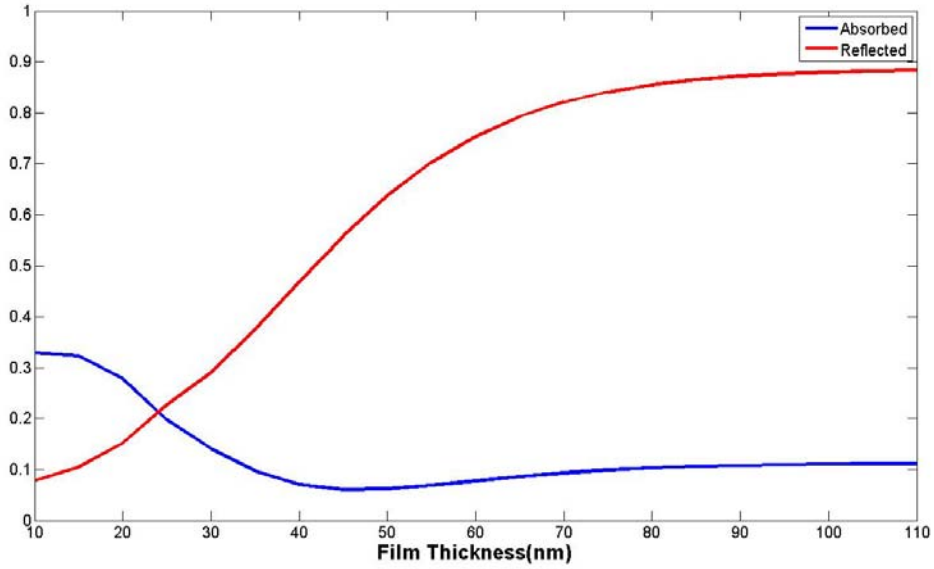

Figure 5.6 Simulated Reflectivity vs. metal thickness. After 80nm film thickness can be assumed infinite

DVD-RW disc can be used as grating source, but they have chalcogenide material for recording medium which prevents further processing of DVD-RWs. DVD-R discs use dye layers to record data., which can be easily solved in isoprophanol or acetone. DVDs are made of two layers attached to each other. After cutting one side of disc, these layers can be seperated. These two parts are complement of each other. Both can be used for grating fabrication. On the other hand one of these part has metallic layer which prevents the grating layer to be harmed by isoprophanol or acetone washing process. After washing off the dye layer, PDMS is poured on modified DVD-R and cured at 70ºC for 5 hours. Then the PDMS layer is peeled off . We now have mapped our grating structure from modified DVD-R to PDMS. As substrate layer a thick layer of SiNx is growth on silicon wafer. Then a mixture of 1:3 of photoresist (AZ5214) and thinner (AZ1500) is spin coated on the sample at 8000rpm. PDMS stamp then released on spin coated sample and hard baked at 180ºC for 5 minutes. Then, the sample is left to cool down and PDMS layer is removed. Finally, gratings are transferred to SiN_x layer using RIE. CHF_3 and O_2 are used as dry etchant with flow rates 28:8 for five minutes [Fig.5.7].

Characterization of fabricated grating structures are done using AFM(PSIA XEI100) and ellipsometer(V-VASE, J.A. Woollam). Using AFM, surface profile of gratings are analyzed. In Fig. 5.8 three dimensional topography and the depth profile is shown. The depth of fabricated gratings between 60-65nm. Also, power spectrum of depth profile proves the nearly sinusoidal profile of grating. After fabricating gratings, 60 nm of Silver is deposited using thermal evaporation. Then Ellipsometer is used to SPP dispersion. Figs. 5.9-10 show the experimental and numerical dispersion curves of SPPs. From numerical and experimental curves, reflectivity for 532nm wavelength, surface plasmons are excited at 20 degrees. The discreteness of experimental results is due to interpolation of ellipsometer data.

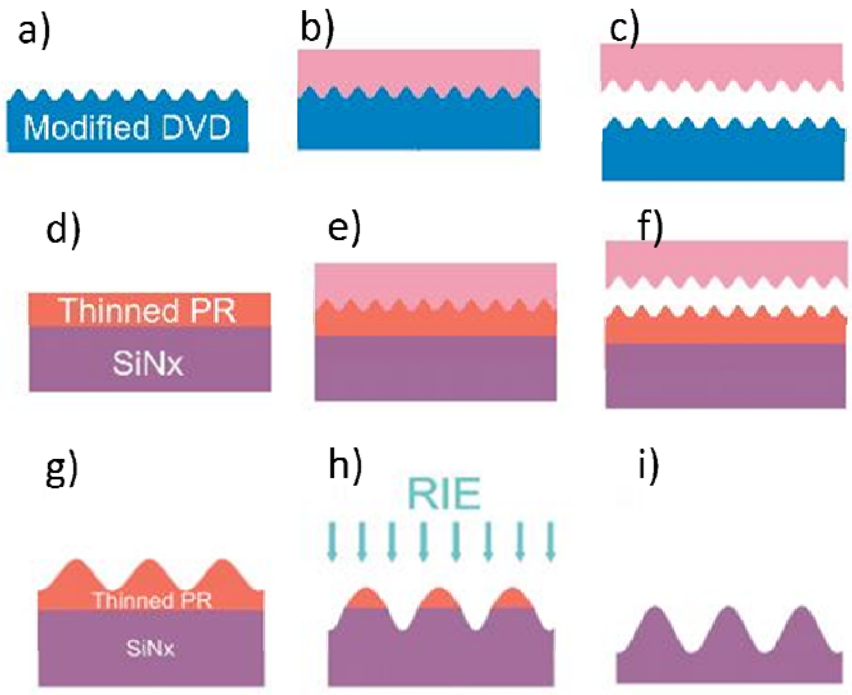

Figure 5.7 Fabrication steps (a) DVD-R disc is used as master mold. (b) PDMS is poured on the master mold and cured at 70 ^{0}C for 5h. (c) Cured PDMS is peeled off from the master mold and used as elastomeric stamp. (d) Thinned photoresist is spin-coated on SiNx deposited substrate. (e) Elastomeric stamp is released gently on the thin polymer film and hard-baked to make polymer hardened. (f) Elastomeric stamp is mechanically removed from the sample g)Grating profile on Thinned Photoresist h)Transferring of grating structures to Sinx using RIE i)Fabricated Grating structures on SiNx

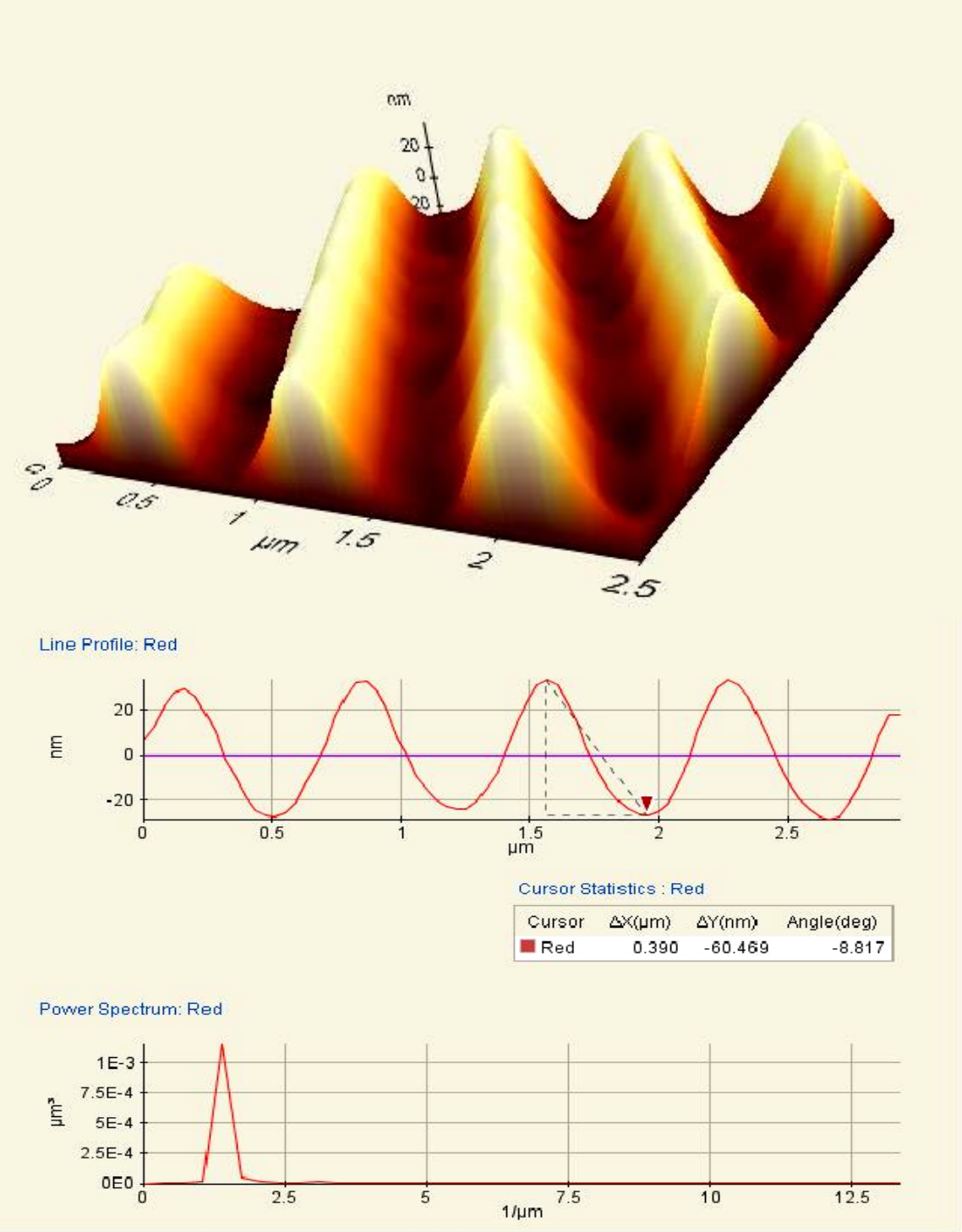

Figure 5.8 AFM Topography and depth profile of fabricated grating

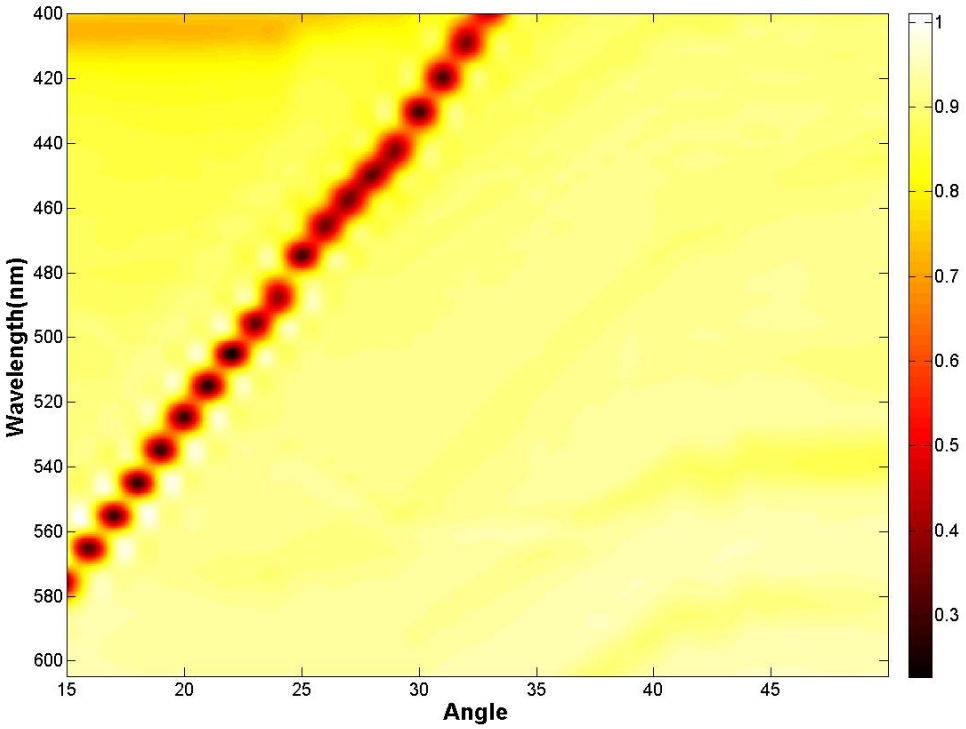

Figure 5.9 Experimental SPP dispersion relation

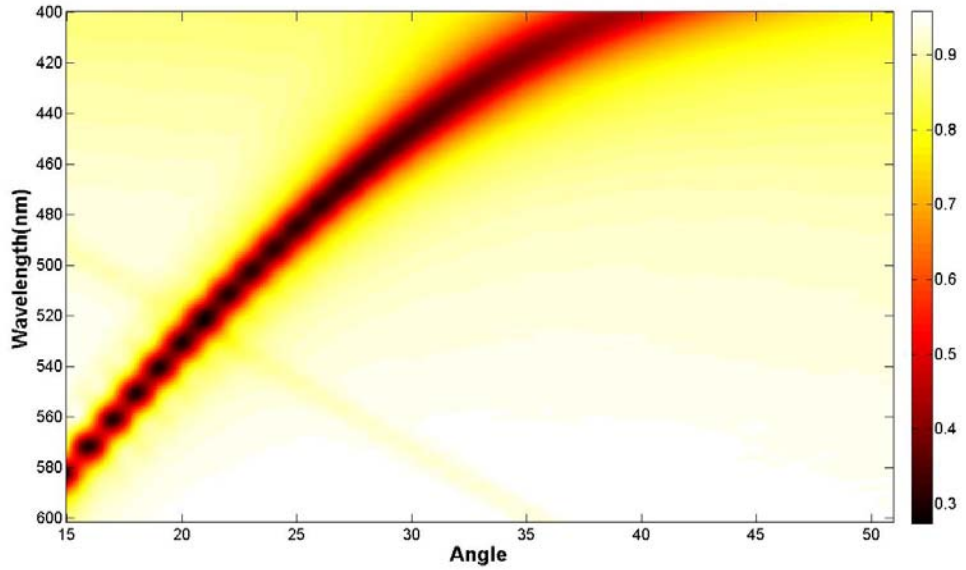

Figure 5.10 Numerical SPP dispersion relation

5.1.2 Absorption Enhancement Measurements

We used Rhodamine 6G as fluorescent layer for absorption enhancement measurements. The emission and absorption spectrum of Rhodamine 6G is shown in Fig. 5.11. The absorption maximum is at 540nm, so that we used 532nm laser to excite the dye layer. After fabrication of grating structures, we spin coated them with Rhodamine 6G doped PMMA at 8000 rpm. The thickness of the film is about 20nm. Then, we excite the sample with 532nm laser at different angles and measured the fluorescence spectrum of dye layer. Fig. 5.12 illustrates the experimental setup we have used.

Firstly, we fixed the spectrometer and changed the incidence angle of laser. Then, we measured the fluorescence signal for each angle. Fig 5.13 shows the fluorescence spectrum with respect to incidence angle. Around 25 degrees the intensity is maximum due to the excitation of surface plasmons. In Fig. 5.14, simulated reflectivity and absorption curves with respect to incidence angle for 20nm PMMA coated sinusoidal silver grating. From the simulation, the surface plasmons are excited at 25 degrees and from our measurements we observed fluorescence maximum at this angle.

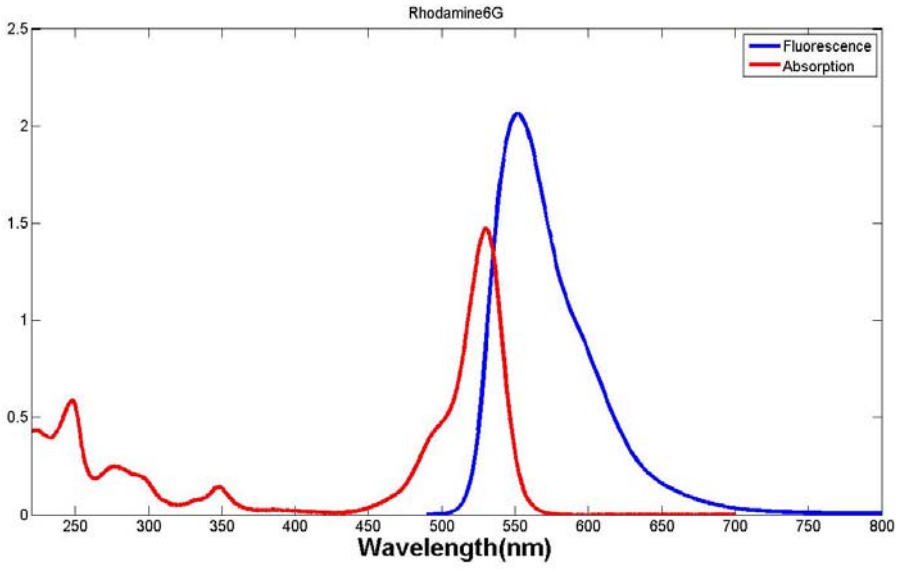

Figure 5.11 Absorption and emission spectrum of Rhodamine 6G dye. The wavelength of laser is 532 nm due to absorption maxima at 540nm.

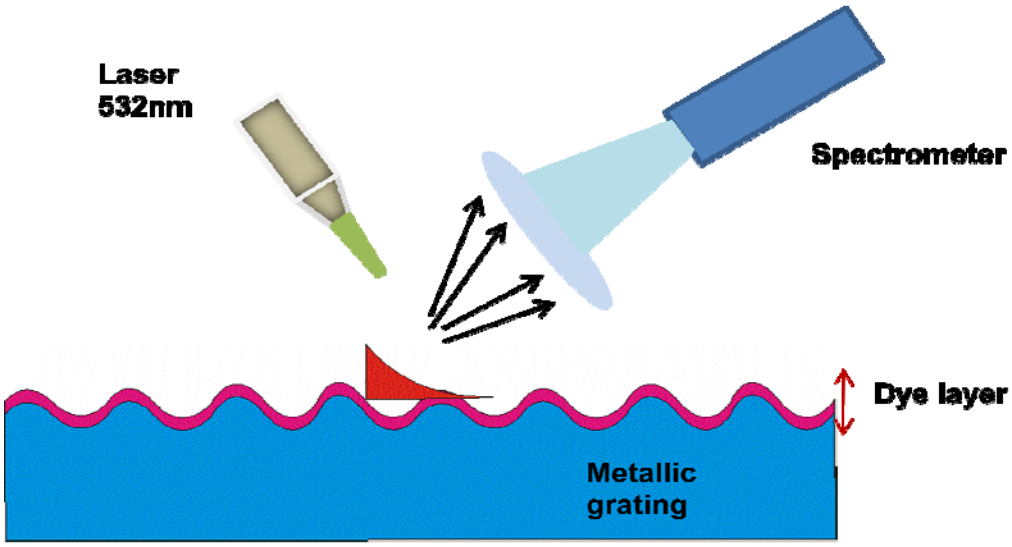

Figure 5.12 Experimental setup we have used to measure absorption enhancement

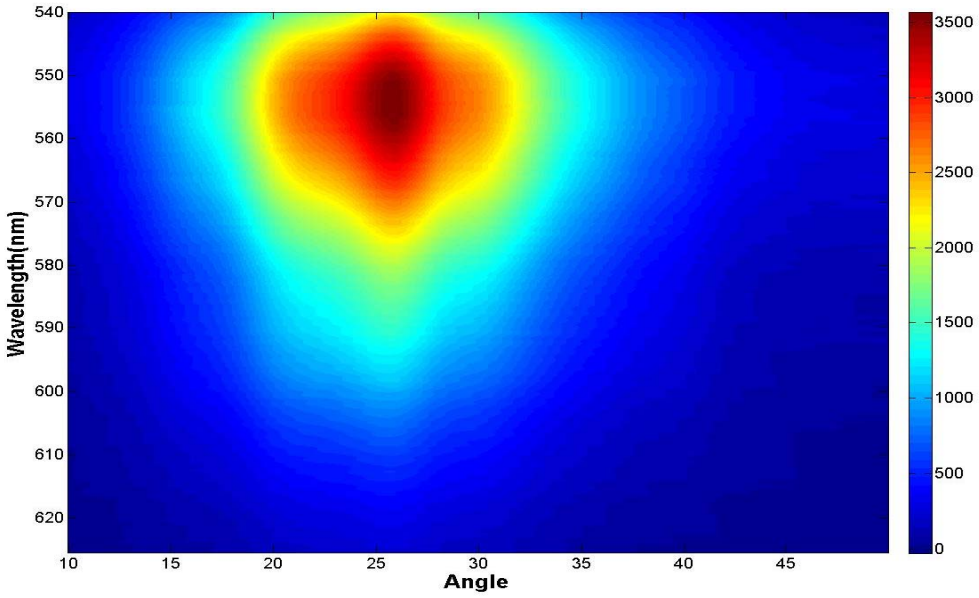

Figure 5.13 Measured fluorescence data with respect to angle. The shift of resonance of surface plasmons are due to the PMMA coating[See 5.14]. At resonance angle(25 degrees), emission is enhanced due to coupling of surface plasmons on gratings. Absorption is enhanced due to enhancement excitation wavelength intensity on gratings. Λ=532nm

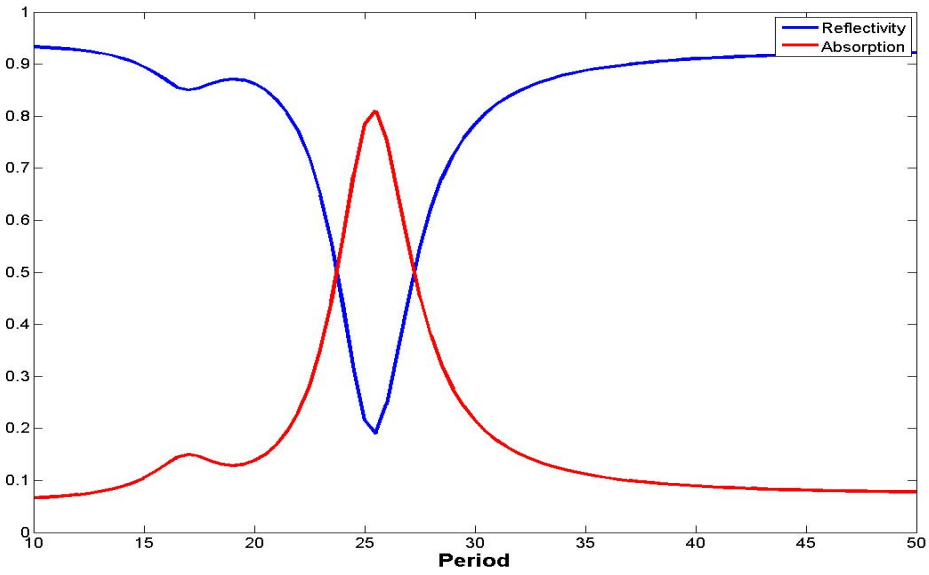

Figure 5.14 Simulated reflectance and absorption curves for gratings coated with 20nm PMMA. At 25 degrees surface plasmons are coupled to surface.

Figs. 5.15 shows the fluorescence signal for 10 and 25 degrees. Fluorescence intensity is enhanced up to 12 fold at 25 degrees with respect to 10 degrees. At 10 degrees surface plasmons are not excited from our simulations and measurements. So that we used 10 degrees as the reference for absorption enhancement measurements. We used unpolarized laser for the measurements. So that, 25 fold absorption enhancement is possible for TM polarized laser. Simulated data is well matched with the experimental data. Furthermore, we have measured the angular distribution of emission. We fixed the laser at the plasmon resonance angle, then changed the angular position of spectrometer. Fig.5.16 shows, the measured angular distribution of emission. Around 20 degrees emission spectrum is maximum. From this figure directionality of emission pattern is indicated.

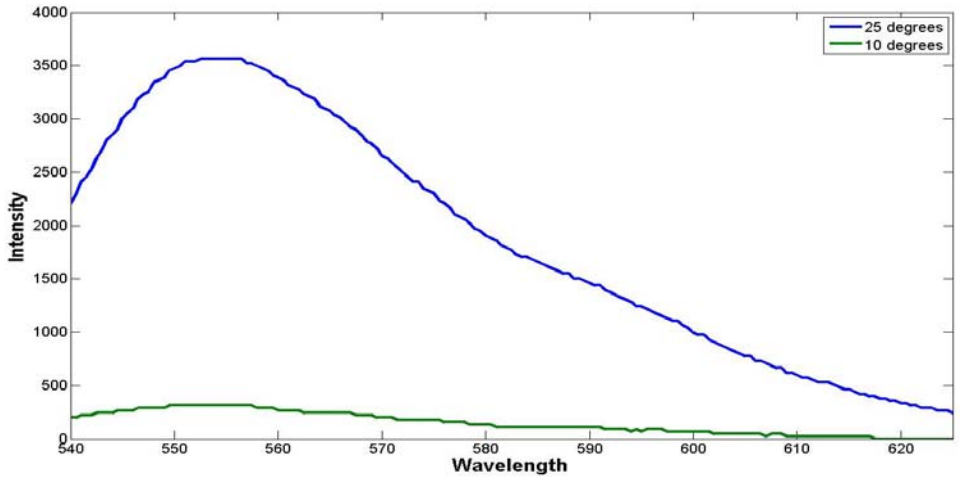

Figure 5.15 Fluorescence signals for 10 and 25 degrees. Emission is enhanced due to coupling of surface plasmons on gratings. Absorption is enhanced due to enhancement excitation wavelength intensity on gratings. We defined absorption enhancement as the ration of fluorescence signals of at 555nm(emission maximum for Rhodamine 6G). At 25 degrees surface plasmons are coupled to surface and the photonic mode density at the excitation wavelength increases, so that fluorescence signal intensity increases. Λ=532nm

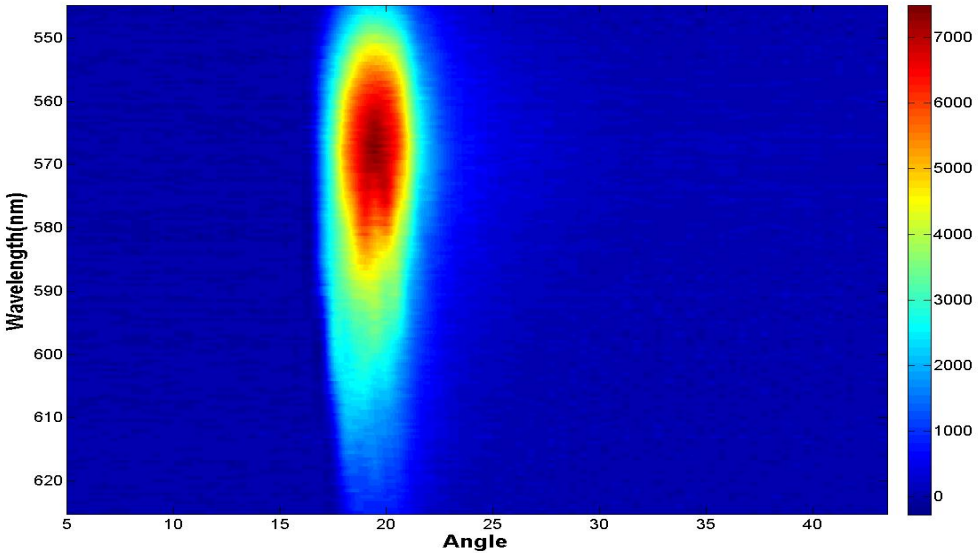

Figure 5.16 Measured angular distribution of fluorescence of dye layer on sinusoidal grating. The emission pattern is highly directional. Excitation wavelength is 532nm

5.1.3 Emission Enhancement Measurements

For emission enhancement measurements, we used another setup. Fig. 5.17 shows the setup for the emission measurements. We used Witec Alpha300 micro raman mode, rather than building our setup. Since, our micro raman apparatus performing the same measurements. We also used micro raman apparatus to measure the emission on lamellar gratings and nanoantenna strips. Fig. 5.18 shows the measured fluorescence image on Rhodamine 6G doped PMMA coated grating. The black region indicate the region that is not coated with silver. The fluorescence intensity on the sample changes due to the ridges and grooves of the grating. Fig. 5.19 shows the intensity of neighbouring rigde and groove points of fluorescence image. They are almost same, but there is still an intensity difference. This can be understood by means of simulation we have done in the previous chapter. In Fig. 5.20, radiative rate enhancement and quantum yield of an emitter is simulated for both polarization. At the grooves emission is enhanced more for both polarization. So that, our experimental and simulation results are well consistent.

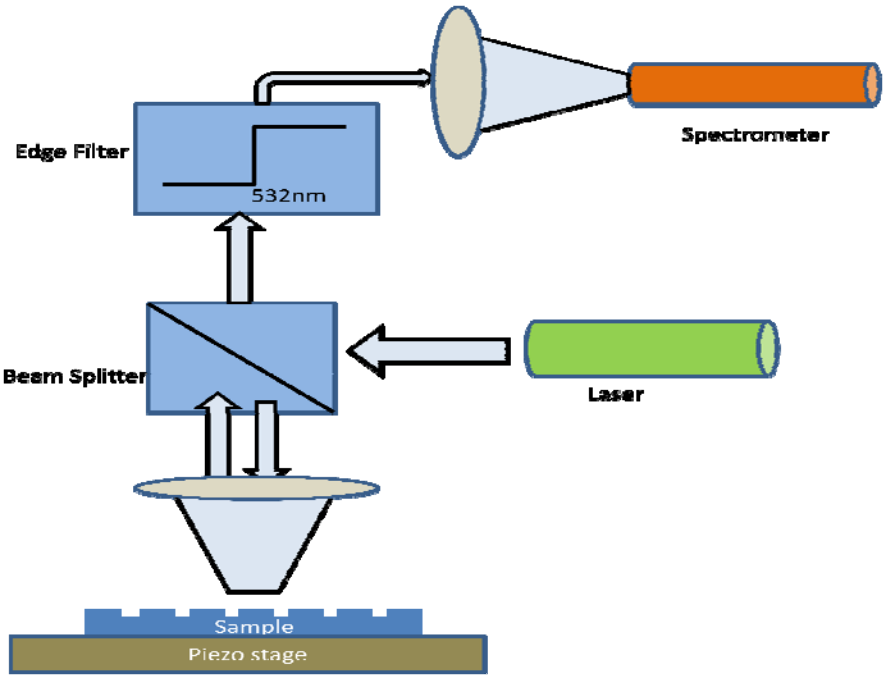

Figure 5.17 Experimental setup for emission measurements

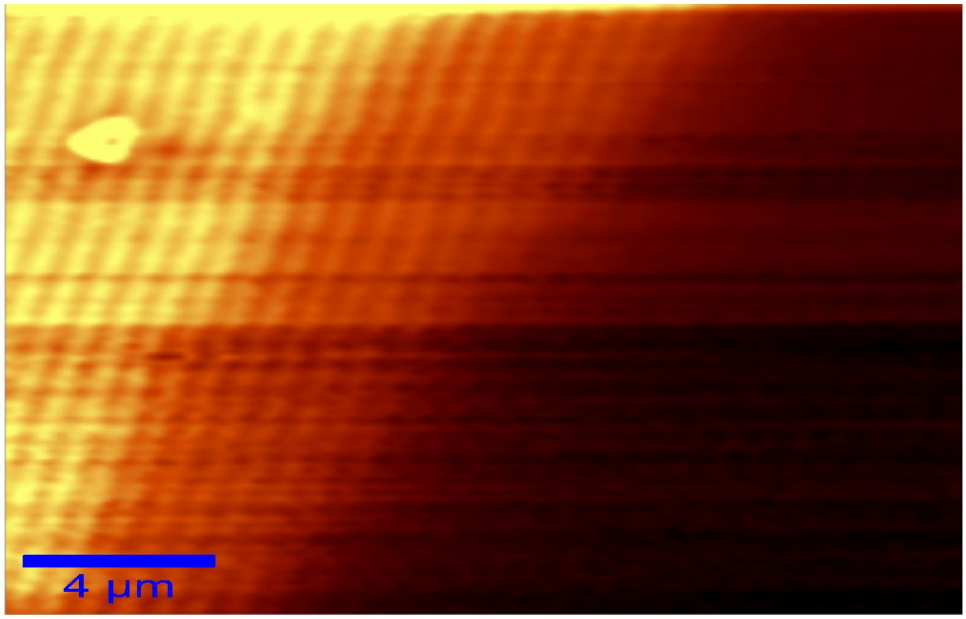

Figure 5.18 Fluorescence image of dye doped PMMA coated grating. The position dependency of emission is apparent on different locations [See Fig. 5.23 for fluorescence data]

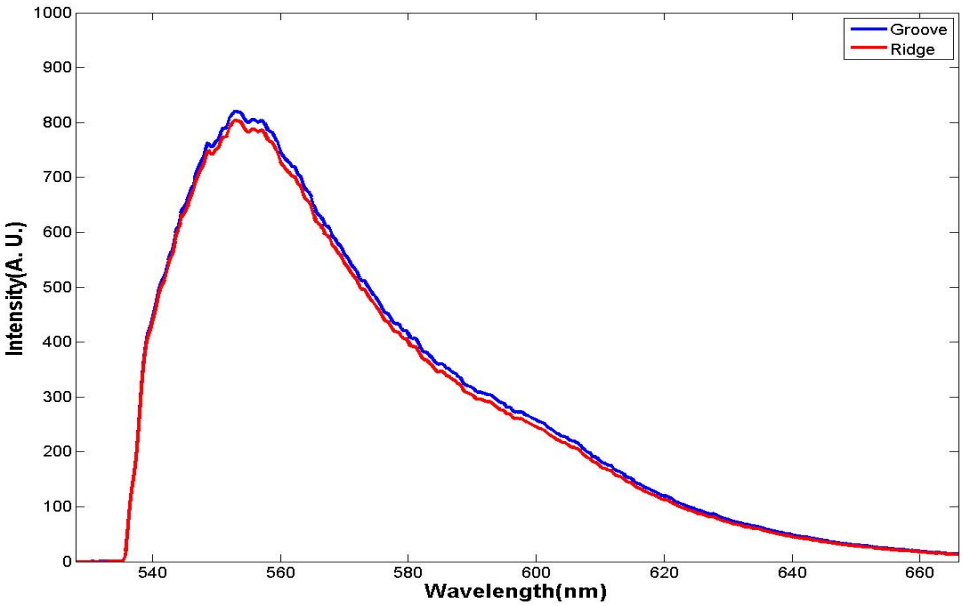

Figure 5.19 Measured Fluorescence intensity of neighbouring ridge and groove of grating. Numerical and experimental data are well matched[See Fig. 5.23 for numerical results]

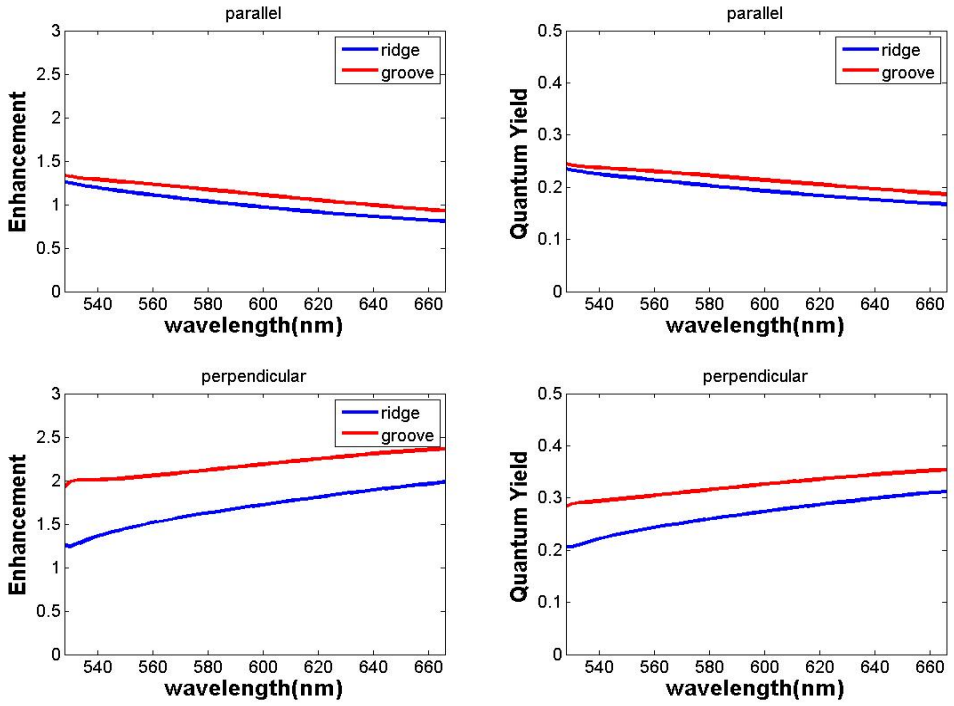

Figure 5.20 Simulated radiative rate enhancement and quantum yield for parallel and perpendicular polarization. For both polarizations emission is enhanced more on grooves of grating.

5.2 Emission Enhancement on Biharmonic Gratings

We fabricated biharmonic gratings using focused ion beam (FIB) technique. We used the emission dye layer using micro raman setup. The spectrometer of micro raman setup is designed for raman measurements and the measurement interval of the spectrometer is between 530nm and 660nm. So that, we designed our biharmonic structures, that have band gap near 630nm. Also, at this wavelength Rhodamine 6G has no raman peaks. After various attempts, we fabricated the biharmonic structures given in Fig.5.21. In Fig. 5.22 the AFM surface profiles of fabricated biharmonic gratings. Fig. 5.23 shows the simulated dispersion relation for fabricated grating structures. Finally we spin coated the gratings with Rhodamine 6G doped PMMA. Then, we measured the fluorescence signal using micro raman setup. In Fig.5.24 fluorescence signal for metal coated grating and flat surfaces are shown. The fluorescence signal is enhanced relative to bare metal surface. Also, the emission is

enhanced around 630nm due to enhanced plasmonic mode density for biharmonic gratings.

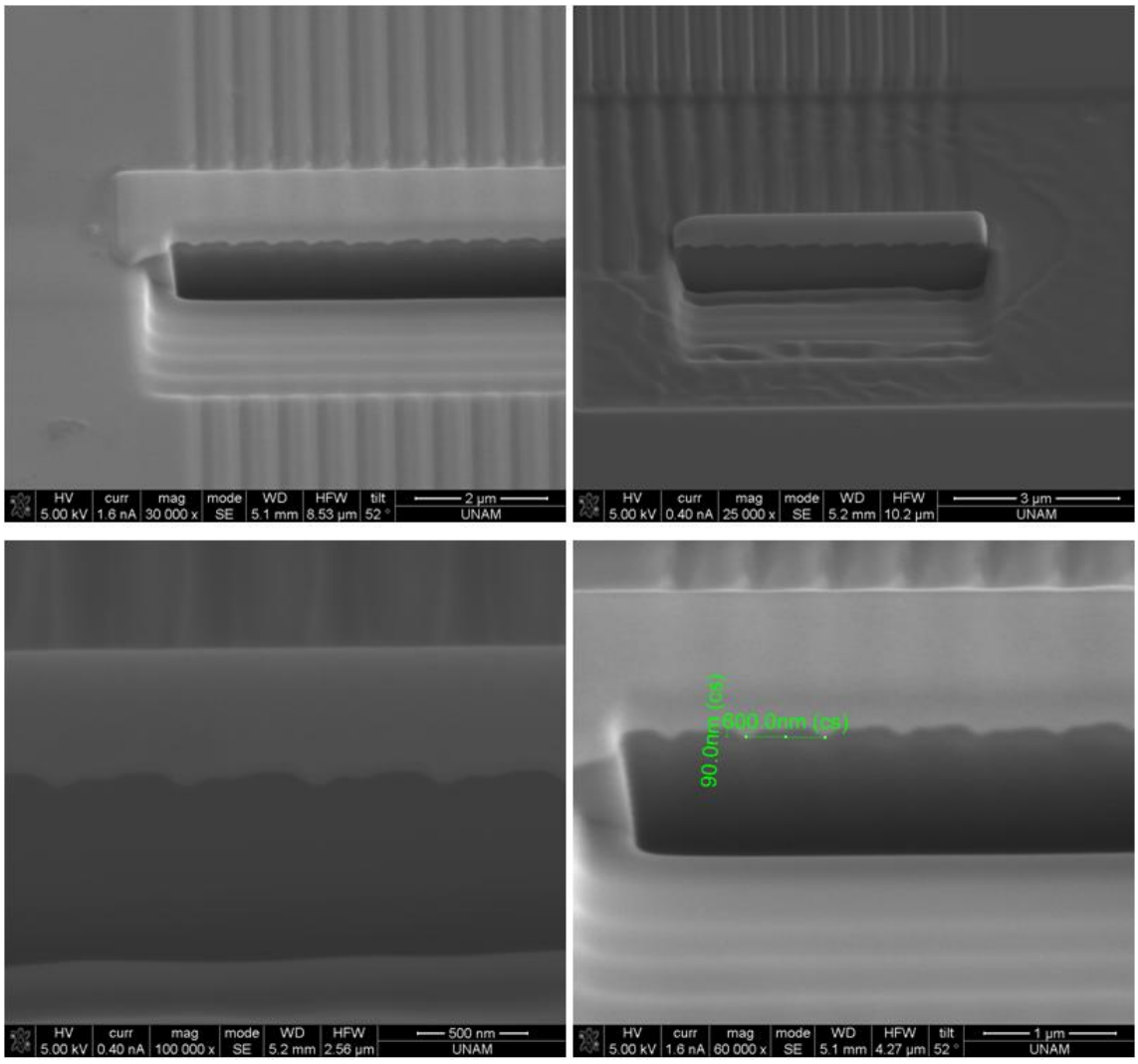

Figure 5.21 Biharmonic gratings with different depths. Period = 600nm

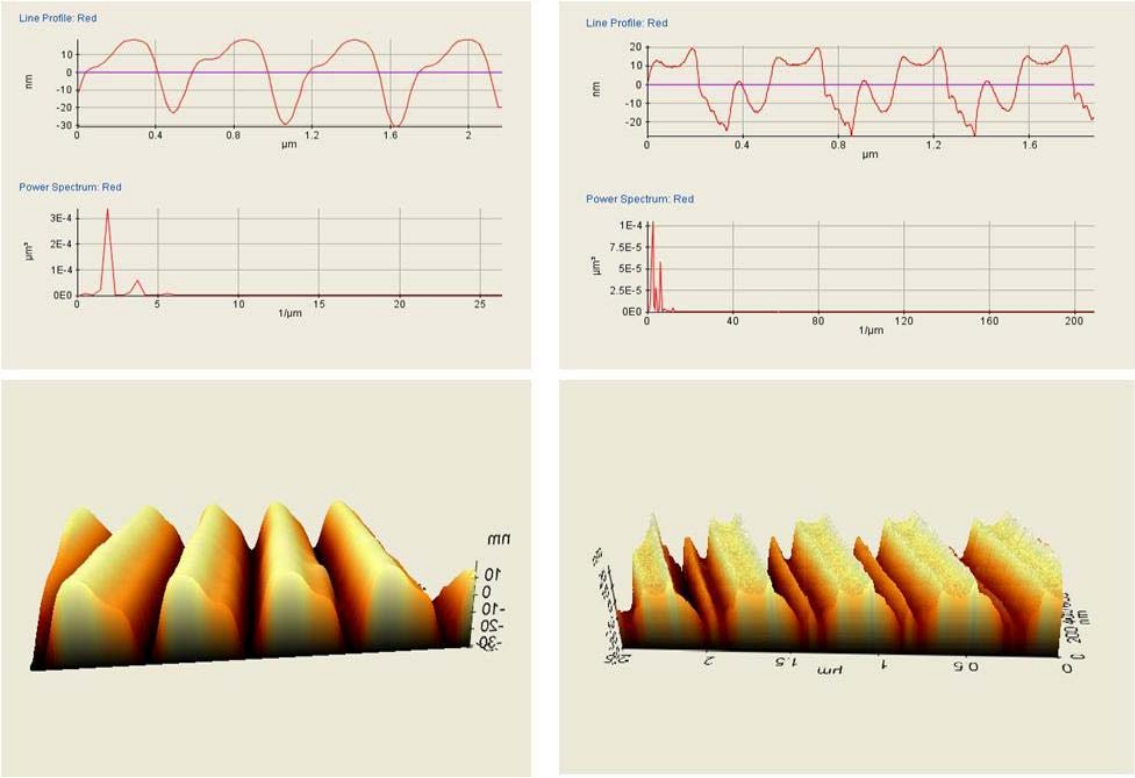

Figure 5.22 Surface profile and topography of fabricated biharmonic gratings. The depth of the grating structures are nearly 45nm

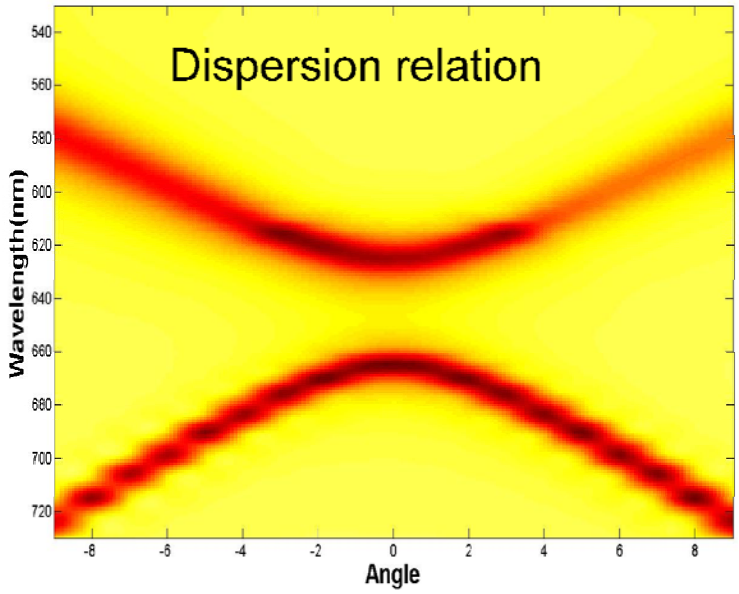

Figure 5.23 Simulated dispersion relation for the biharmonic gratings[See Fig. 5.21]

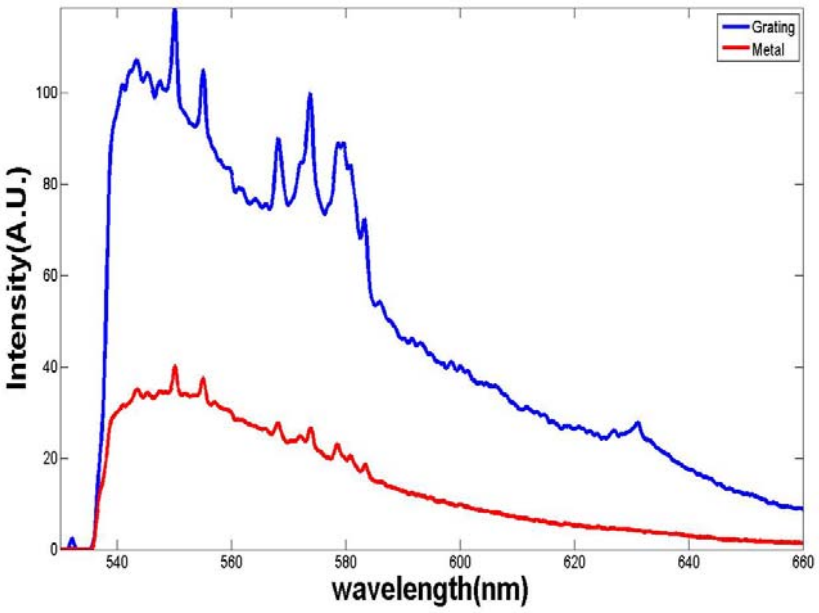

Figure 5.24 Measured fluorescence signal using micro raman setup. The Excitation wavelength is 532nm. The fluorescence peak at 630nm is due to the enhancement enhanced plasmonic mode density for biharmonic grating [See Fig. 5.23]

5.3 Emission Enhancement on Nanoantenna Strips

We fabricated nanoantenna strips using electron beam lithography. We start with sputtering a thick ITO layer . In electron beam fabrication processes, organic molecules, polymers are charged with electrons which harms the fabricated structures. In our experimental setup we have 532nm laser, to which ITO is transparent. We fabricated the nanoantenna structure we proposed in the previous chapter. Fig 5.25 shows the SEM images of fabricated nanoantenna structures. Finally, we measured the fluorescence signal on nanonatenna structures using micro raman setup. We spin coated the samples with Rhodamine 6G doped PMMA. The thickness of the polymer layer is nearly 20nm. Figs. 5.26-27 show the fluorescence image and fluorescence intensity of dye layer on various antenna. There is almost 25 fold emission enhancement. The effect of antenna can be understood from the peak around 540nm. This peak is due to the emission enhancement of fluorescence process.

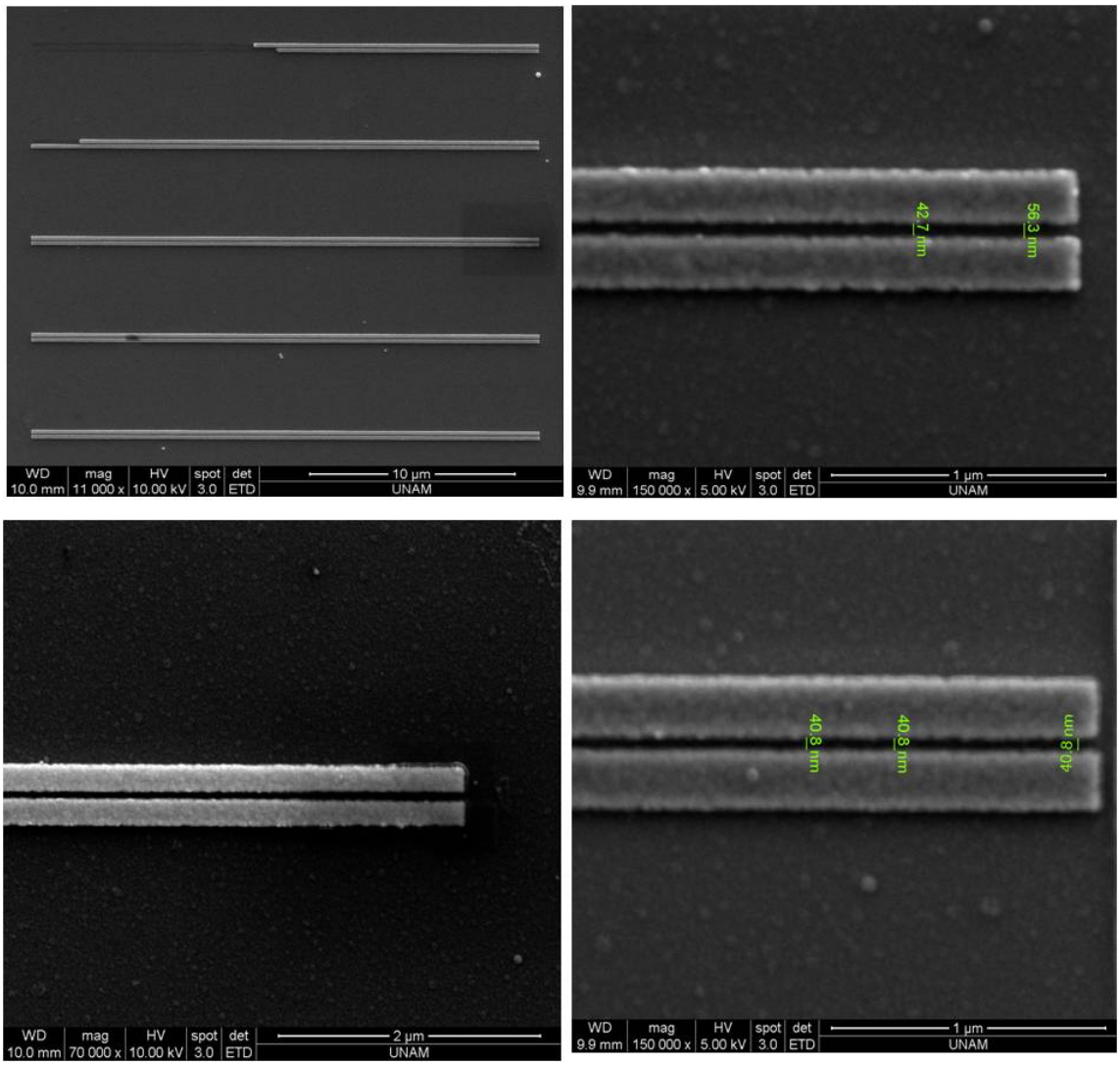

Figure 5.25 SEM images of Fabricated nanoantenna structures

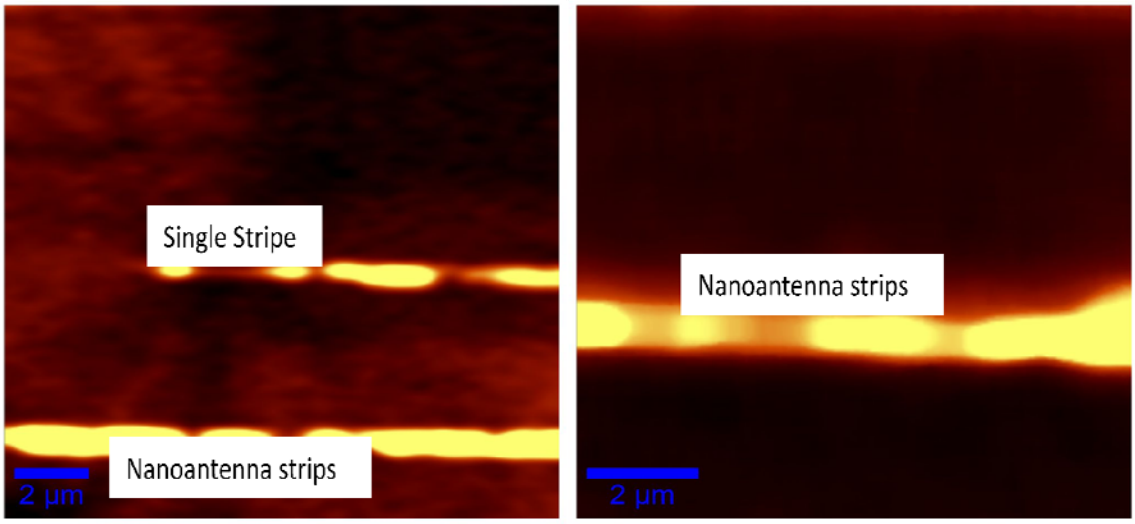

Figure 5.26 Fluorescence image of dye doped PMMA coated nanoantennas.

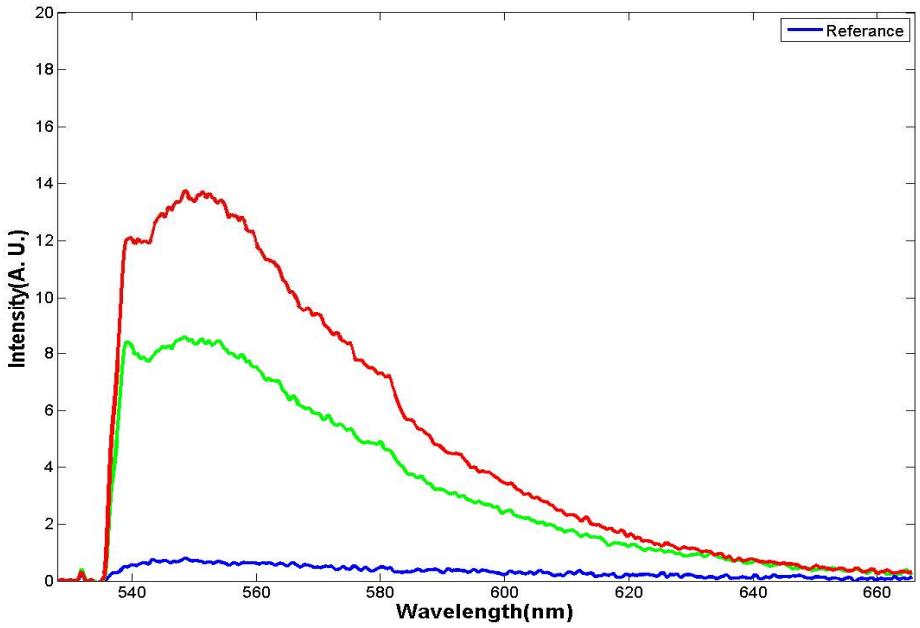

Figure 5.27 Fluorescence intensity of dye layer on nanoantenna structure[See Fig. 5.25]. Reference signal is the fluorescence of dye layer on glass. Fluorescence signal is enhanced on nanoantenna structure.

Chapter 6

Conclusion

In this thesis, we aimed to integrate emission and absorption properties of fluorophores with surface plasmons. We started with classical dipole model of optical emitters and derived the decay rates in homogeneous and inhomogeneous environment. Absorption enhancement is explained by means of Fermi' Golden Rule. Then, using Poynting Theorem and Gauss's Law simulation method for emission of classical dipole model is explained. Emission enhancement is studied on nanoantenna strips, sinusoidal and biharmonic gratings numerically using finite difference time domain (FDTD) method. Position and wavelength dependent radiative rate enhancement and quantum yield calculations are performed obtained simulation data. The dispersion curve and scattering cross section calculations are used to understand the emission enhancement on these structures. The effect of local plasmonic mode density on different locations of sinusoidal and biharmonic gratings regarding the polarization of dipoles is studied. Emission enhancement near the bandgap of biharmonic gratings indicates the importance of not only the effect of bandgap but also the distribution and polarization of local plasmonic mode density.

In the experimental part, we have fabricated grating and nanoantenna structures utilizing soft lithography, electron beam lithography and focused ion beam techniques. Surface profile of DVD-R gratings is optimized to assure maximum coupling conditions for 532nm wavelength using rigorous coupled wave analysis (RCWA). Then, gratings are fabricated using soft lithography and reactive ion etching (RIE) to have desired surface profile. For absorption enhancement measurements, we used our setup. Due to coupling of surface plasmon polaritons on the grating surface, we observed 12 fold absorption enhancement for unpolarized light. For TM polarized light, 25 fold absorption enhancement is possible. The directionality of emission on sinusoidal gratings are also presented. We also measured the emission enhancement on sinusoidal gratings using micro raman setup. Using this setup, we measured the

emission of dye layer on different position of grating. We observed that, the emission of dye layer is enhanced more on grooves with respect to the ridges of the grating.

We fabricated biharmonic gratings using focused ion beam technique. The periodicity of the grating structures are 600nm due to the limitations of micro raman setup. We have shown that, the emission is enhanced due to the enhanced plasmonic mode density at the band gap edges using biharmonic gratings and confirmed these experimental results with simulations.

Finally, using the micro raman setup, we measured the emission of dye layer on gratings and nanoantenna strips. We observed almost 25 fold fluorescence enhancement on nanoantenna structures. However, we could not show emission enhancement due to the enhanced plasmonic mode density at certain wavelengths.

REFERANCES

1. Jelena Vuckovic, Marko Loncar ,Axel Scherer, Surface plasmon enhanced light emitting diode, IEEE journal of Quantum Electronic, Vo.36, No.10, 2000
2. Aaron C. Hryciw, Young Chul Jun, Mark L. Brongersma, Plasmon enhanced emission from optically doped MOS light sources, Optics Express, Vol.17, No.1, 2008
3. Yiyang Gong, Jesse Lu, Szu-Lin Cheng, Yoshio Ishi, Jelena Vuckovic, Plasmonic enhancement of emission from Si-NCs, Applied Physics Letters,94, 011106-1, 2009
4. Ertugrul Cubukcu, Eric A. Kort, Kenneth B. Crozier, Federico Capasso,Plasmonic laser antenna,Applied Physics Letters, Vol. 89, No. 093120, 2006
5. Rupert F. Oulton, Volker J. Sorger, Thomas Zentgraf, Ren-Min Ma3, Christopher Gladden,Lun Dai, Guy Bartal1, Xiang Zhang, Plasmonic laser at deep wavelength scale, Nature, Vol. 461,October 1st 2009
6. Yu. A. Akimov, K. Ostrikov, E. P. Li, Plasmon enhancement of optical absorption in thin film silicon solar cells, Plasmonics, 4:107-113,2009
7. Sang-Kyun Kim, Chang Hee Cho, Baek Hyun Kim, Yong Seok Choi, Seong Ju Park Kimoon Lee, Seongil Im, The effect of localized surface plasmon on the current of silicon NC photodetectors, Applied Physics Letters, Vol.94, 183108,2009
8. Ragip Pala, Justin White, Edward Barnard, John Liu, Mark L. Brongersma, Design of Plasmonic Thin film solar cells with broadband absorption enhancements, Advanced Materials, Vol.21, No. 1-6, 2009
9. M. Ringler, A. Schwemer, M. Wunderlich, A. Nichtl, K. Kurzinger, T.A. Klar, J. Feldmann, Shaping emission spectra of fluorescent molecules with single plasmonic nanoresonators, Physical Review Letters, Vol.100, No. 203002, 2008
10. P. Biagioni, J.S. Huang, L. Duo, M. Finazzi, B.Hecht, Cross resonant optical antenna,Vol.102,No.256801,2009
11. Jian Zhang, Yi Fu, Mustafa H. Chowdhury, Josepg Lakowicz, Metal enhanced single fluorescence on silver particle monomer and dimer, coupling effect between metal particles, Nano letters, Vo.7, No.7,2007
12. H. Mertens, A. Polman, Strong luminescence quatum efficiency enhancement near prolate metal particles:Dipolar versus higher order modes,Journal of Applied Physics Letters, Vol.105, No.044302,2009
13. L. Bianco , F. J. Garcia Abajo, Spontaneous emission in complex nanostructures, Physical Review,Vol.69, No.205414,2004
14. Muralidar Ambati, Dentcho A. Genov, Rupert F. Oulton, Xiang Zhang, Active Plasmonics: Surface plasmon interaction with optical emitters IEEE journal of Selected Topics in Quantum Electronics,Vol.14,No.6,2008
15. J. B. Khurgin, G.Sun, A. Soref, Electrolumincescence efficiency enhancement using metal nanoparticles, Applied Physics Letters, Vol.93, No.021120,2008
16. G. Vecchi, V. Giannini, J. Gomez Rivas, Shaping of fluorescent emission by lattice resonances in plasmonic crystals of nanoantennas, Physical Review Letters, Vol.102,No. 146807, 2009
17. David J. Griffiths, Introduction to Quatum Mechanics, Pearson Educational International, 2005

18. David Miller, Quantum Mechanics for Scientists and Engineers, Cambridge University Press, 2007
19. Lucas Novotny, Bert Hecht, Principles of Nanooptics, Cambridge University Press, 2006
20. Emmanuel Fort, Samule Gresillon, Surface enhanced fluorescence ,Journal of Physics D: Applied Physics, Vol. 41, No.013001,2008
21. Vincenzo Giannini, Jose A. Sanchez-Gil, Otto L. Muskens, Jaime Gomez Rivas, Electrodynamic calculations of spontaneous emission coupled to metal nanostructures of arbitrary shape: Nanoantenna enhanced fluorescence , Journal of optical Society of America, Vol. 26, No.8,2009
22. John David Jackson, Classical Electrodynamics, Third Edition
23. Herve Rignault, Fabien Lemarchand, Anne Sentenac, Dipole radiation into grating structures, Journal of optical Society of America, Vol. 17, No.6,2000
24. Norbert Danz, Ralf Waldhausl, Andreas Brauer, Dipole Lifetime in stratified media, Journal of optical Society of America, Vol. 19, No.3, 2002
25. Mark L. Brongersma , Pieter G. Kik, Surface Plasmon Nanophotonics, Springer in optical sciences, Vol. 7, 2007
26. http://www.comsol.com/products/multiphysics
27. http://www.cst.com/Content/Products/MWS/Overview.aspx
28. http://www.lumerical.com
29. Franziska Kaminski, Mark Agio, Sandoghar, Lavinia Rogemete, Design of plasmonic nanoantenna for enhancing spontaneous emission,Optics Letters, Vol. 32, No 12, 2007
30. Stefan A. Maier, Plasmonics: Fundamentals and applications, Springer Publications, 2007
31. Edward D. Palik, Handbook of optical constant
32. M. G. Moharam, Drew A. Pommet, Eric B Grann, T. K. Gaylord , Stable Implementation of the rigorous coupled wave analysis for surface relief gratings: Enhanced Transmittance matrix approach, Journal of optical Society of America, Vol. 12, No.5, 1995
33. Benfeng Bai and Jari Turunen, Fourier modal method for the analysis of second-harmonic generation in two-dimensionally periodic structures containing anisotropic materials, , Journal of optical Society of America, Vol. 24, No.5, 2007
34. Raymond Rumpf, Design and optimization of nano-optical elements by coupling fabrication to optical behavior, Phd Thesis, University of Central Florida, 2006
35. Mario Agaio, Franziska Kaminski, Vahid Sandoghar,Engineering gold nanoantenna to enhance the emission of quatum emitters,Proc.SPIE Vol. 6717,2007
36. O.L.Muskens, V. Giannini, J.A. Sanchez, J. Gomes Rivas, Strong enhancement of radiative decay rate of emitters by single plasmonic nanoantennas,Nanoletters,Vol.7, No.9, 2007
37. Edward S. Barnard, Justin S. White, Anu Chandran, Mark L. Brongersma,Spectral properties of plasmonic resonator antennas, Optics express, Vol. 16 No.21 ,2008
38. Lavinia Rogobete, Franziska Kaminski, Mario Agio, Vahid Sandoghar,Design of plasmonic nanoantennae for enhancing spontaneous emission, Optics Letters, Vol.32, No.12,2007

39. Jörg P. Kottmann,Oliver J.F. Martin,Plasmon resonant coupling in metallic nanowires, Optics express,Vol. 18, No.12, 2001